Influence of deformation and fluids on the Ti exchange in quartz

Michel Bestmann[1,1], Giorgio Pennacchioni[2,2], Bernhard Grasemann[3,3], Benjamin Huet[4,4], Michael W. M. Jones[5,5], and Cameron M. Kewish[6,6]

[1]GeoZentrum Nordbayern
[2]University of Padova
[3]University of Vienna
[4]Geological Survey of Austria
[5]Central Analytical Research Facility, Queensland University of Technology
[6]ANSTO

November 30, 2022

Abstract

Coarse-grained quartz veins from the Prijakt Nappe (Austroalpine Unit, Schober Mountains, Eastern Alps), that formed under amphibolite facies conditions, were overprinted by lower greenschist facies deformation. During overprinting, subgrain rotation (SGR) recrystallization was the dominant mechanism assisting the evolution from protomylonite to (ultra)mylonite. The initial Ti-concentration [Ti] (3.0-4.7 ppm) and corresponding cathodoluminescence (CL) signature of the quartz vein crystals were reset to different degrees mainly depending on the availability of fluids and their partitioning across the microstructure. The amount of strain played a subordinate role in resetting. In recrystallized aggregates the most complete re-equilibration ([Ti] of 0.2-0.6 pm) occurred in strain shadows surrounding quartz porphyroclasts, acting as fluid sinks, and in localized shear bands that channelized fluid percolation. We applied a correlative multi-analytical workflow using optical and electron microscopy methods (e.g. electron backscatter diffraction and cathodoluminescence) in combination with secondary ion mass spectroscopy for [Ti] measurement. The most efficient [Ti] resetting mainly occurs along wetted high angle boundaries (misorientation angle >10-15°), and to a minor extend (partial resetting) along dry low angle boundaries (<10-15°). This key-study prove for the first time that pure subgrain rotation recrystallization in combination with dissolution-precipitation under retrograde condition is able to provide microstructural sites to apply the TitaniQ geothermobarometer at deformation temperatures down to 300-350 °C provided that information on pressure and Ti-activity is available.

Influence of deformation and fluids on the Ti exchange in quartz

Michel Bestmann[1], Giorgio Pennacchioni[2], Bernhard Grasemann[3], Benjamin Huet[4], Michael W. M. Jones[5], Cameron M. Kewish[6,7]

[1]GeoZentrum Nordbayern, Friedrich-Alexander Universität Erlangen-Nürnberg, 91054 Erlangen, Germany

[2]Department of Geosciences, University of Padova, 35131 Padova, Italy

[3]Department of Geology, University of Vienna, A-1090 Vienna, Austria

[4]Department of Hard Rock Geology, Geological Survey of Austria, A-1030 Vienna, Austria

[5]Central Analytical Research Facility, Queensland University of Technology, Brisbane, 4000, QLD, Australia

[6]Australian Synchrotron, ANSTO, Clayton, 3186, Vic, Australia

[7]Department of Chemistry and Physics, School of Molecular Sciences, La Trobe University, Melbourne, VIC 3086

Corresponding author: Michel Bestmann (michel.bestmann@fau.de)

Key Points

- Ti-in-quartz re-equilibration is possible in the regime of subgrain rotation recrystallization even at lower greenschist facies condition
- Ti resetting depends on the availability of fluid independently of strain and is mainly related to wetted interconnected grain boundaries
- Partial Ti resetting also take place along dry subgrain boundaries

Abstract

Coarse-grained quartz veins from the Prijakt Nappe (Austroalpine Unit, Schober Mountains, Eastern Alps), that formed under amphibolite facies conditions, were overprinted by lower greenschist facies deformation. During overprinting, subgrain rotation (SGR) recrystallization was the dominant mechanism assisting the evolution from protomylonite to (ultra)mylonite. The initial Ti-concentration [Ti] (3.0-4.7 ppm) and corresponding cathodoluminescence (CL) signature of the quartz vein crystals were reset to different degrees mainly depending on the availability of fluids and their partitioning across the microstructure. The amount of strain played a subordinate role in resetting. In recrystallized aggregates the most complete re-equilibration ([Ti] of 0.2-0.6 pm) occurred in strain shadows surrounding quartz porphyroclasts, acting as fluid sinks, and in localized shear bands that channelized fluid percolation. We applied a correlative multi-analytical workflow using optical and electron microscopy methods (e.g. electron backscatter diffraction and cathodoluminescence) in combination with secondary ion mass spectroscopy for [Ti] measurement. The most efficient [Ti] resetting mainly occurs along wetted high angle boundaries (misorientation angle >10-15°), and to a minor extend (partial resetting) along dry low angle boundaries (<10-15°). This key-study prove for the first time that pure subgrain rotation recrystallization in combination with dissolution-precipitation under retrograde condition is able to provide microstructural sites to apply the TitaniQ geothermobarometer at deformation temperatures down to 300-350 °C provided that information on pressure and Ti-activity is available.

Plain Language Summary

Since around 10 years, the so-called TitaniQ geothermometer is used to constrain deformation temperatures in quartz-rich rocks. The calibration roots on the direct correlation of the titanium trace element concentration in quartz with respect to the ambient temperature. However, the processes and parameters, which lead to re-equilibration of the Ti-in-quartz system during deformation, are not fully understood yet. Here we analysed deformed quartz veins from the Eastern Alps applying a correlative data workflow. In contrast to recent studies, we were able to show that instead of strain the availability of fluids and it's partitioning, especially along grain boundaries plays an essential role. We also provide a robust interpretation tool for the interplay between grain-scale deformation, fluid-rock interaction and geochemical exchange during increasing strain in the quartz mylonites. Finally, we were able to identify specific microstructures representing most re-equilibrated sites in order to apply the TitaniQ geothermometer even at lower greenschist facies deformation conditions (independently constrained by chlorite thermometry) dominated by subgrain rotation recrystallization.

Keywords

Quartz

TitaniQ thermobarometry

Recrystallization processes

Correlative data workflow

Geochemical re-equilibration

Cathodoluminescence

Introduction

Under static condition, Ti incorporation in quartz lattice during crystal growth is a function of temperature, pressure and Ti activity. Ti concentrations (referred to as [Ti] hereafter) in quartz can, therefore, be used as a geothermometer (TitaniQ: Huang & Audétat, 2012; Thomas et al., 2010; Wark & Watson, 2006) to estimate ambient conditions of quartz formation. TitaniQ is well suited for quartz in magmatic and high-grade metamorphic rocks, and when quartz directly precipitated from a fluid.

[Ti] in quartz can be modified during crystal-plastic deformation. This gives TitaniQ the potential of estimating the ambient conditions of deformation. Since the original proposal by Kohn & Northrup (2009), several authors have attempted to apply TitaniQ to mylonites and to understand the behaviour of Ti in quartz during deformation in either nature (Behr & Platt, 2011; Bestmann & Pennacchioni, 2015; Grujic et al., 2011; Haertel et al., 2013; Kidder et al., 2013, 2018; Korchinski et al., 2012; Nachlas et al., 2014; Pennacchioni et al., 2010) or experiments (Nachlas & Hirth, 2015; Nachlas et al., 2018; Negrini et al., 2014). These studies have shown that strain-induced modification of [Ti] is a process influenced by several parameters, e.g.: the recrystallization processes (Haertel et al., 2013), the amount of finite strain (Bestmann & Pennacchioni, 2015), strain/stress partitioning, fluid percolation and redistribution (Bestmann & Pennacchioni, 2015; Nachlas et al., 2014), and the metamorphic path (e.g. prograde vs. retrograde: Negrini et al., 2014). In particular, to constrain the efficiency of [Ti] re-equilibration, during dislocation creep and subgrain rotation (SGR) recrystallization, is challenging (e.g. Haertel et al., 2013; Grujic et al., 2011). This is not trivial since dislocation creep is dominant in many quartzitic rocks at mid-crustal and, to some extent, lower crustal levels (Campbell et al., 2020; Hawemann et al., 2019). Considering the sluggish, intra-crystalline Ti diffusion in quartz over the temperature range where dislocation creep is predominant (Cherniak et al., 2007), strain-induced resetting of [Ti] is clearly enhanced by the grain size decrease (and increase of reactive grain boundary area per unit volume) during SGR recrystallization. In fact, this process results in reduction of diffusion lengths for re-equilibration and provides pathways for fluids to access the grain interior (Ashley et al., 2014). Enhanced diffusion along dislocation structures ("pipe diffusion") may also contribute to resetting (Nachlas et al., 2018).

Despite the evidence of strain-induced effects, the extent of re-equilibration of [Ti] during dislocation creep to the ambient conditions of deformation appears partial and highly heterogeneous across the strain gradients of quartz mylonites, as well-imaged by SEM-based cathodoluminescence (SEM-CL) maps (Bestmann & Pennacchioni, 2015). There is in fact a direct correlation between the [Ti] and the CL intensity in quartz (e.g. Spear & Wark, 2009; Wark & Spear, 2005). Heterogeneities in degree of re-equilibration of [Ti] occur between microstructural domains within zones of similar finite strain and remain heterogeneous in pervasively deformed and recrystallized quartz mylonites. This reflects the complexity of the microstructural evolution of coarse-grained quartz aggregates with diverse crystallographic orientations in different crustal rocks, e.g. in granitoids or pure quartz veins (Ceccato et al., 2017).

The use of TitaniQ, in quartz mylonites that underwent heterogeneous deformation in the dislocation creep regime, requires identification of the sites of most complete syn-kinematic [Ti] re-equilibration that do not necessarily correspond to the most strongly deformed domains. This identification is only possible through a rigorous protocol of integrated, high-resolution analysis by optical microscopy, SEM-CL, electron backscatter diffraction (EBSD) and direct measurement of [Ti] using secondary ion mass spectrometry (SIMS). SIMS measurements are necessary for quartz deformed under middle to upper or even high-pressure crustal conditions where equilibrium [Ti] are commonly below the ˜7 ppm detection limit of electron probe microanalysis (Nachlas et al., 2018).

Matching the information from the different techniques is not only functional to TitaniQ thermobarometry, but also provides a robust interpretative tool for the interplay between grain-scale deformation, fluid-rock interaction, geochemical exchange and the evolution of the crystallographic preferred orientation (CPO) during increasing strain in a quartz mylonite. We present specific microstructures of deformed quartz veins from the Prijakt Nappe (Austroalpine Unit, Schober Mountains, Eastern Alps, Austria) as a key-study to unravel characteristic deformation processes responsible for partial to complete resetting of the Ti-in-quartz system under retrograde deformation condition in the SGR regime.

Geological settings

The studied samples of deformed quartz veins (2-10 cm thick) were collected near the Barrensee (Schober Mountains, Eastern Alps, Austria) within pre-Alpine paragneisses, orthogneisses and metabasites of the Prijakt Nappe (Austroalpine Unit; Figure 1) (Krenn et. al, 2012; Schulz, 1993). This nappe underwent Eo-Alpine (Cretaceous) subduction to eclogite-facies conditions at 650 °C and 1.9 GPa (Hauke et al., 2019). Quartz veins, that crosscut the eclogitic foliation, have been inferred to have developed at amphibolite-facies conditions (510-590 °C and 0.5-0.6 GPa) during rapid exhumation (Linner, 1999; Thöni, 2006).

In Oligocene-Miocene time, the tectonics of the Eastern Alps was dominated by the indentation of the Dolomites block (Southern Alps), delimited by the Giudicarie and the Periadriatic fault systems (Figure 1), against the Alpine stack. Indentation was accommodated within the Alpine stack by lateral escape, associated with the activity of a network of regional to smaller scale strike-slip faults (e.g., the Defereggental-Anterselva-Valles Line, DAV: Mancktelow et al., 2001) and uplift (Ratschbacher et al., 1989; Rosenberg et al., 2007). The Cenozoic deformation south of the Tauern window is dominated by strike slip faulting. Prior to intrusion of the main Periadriatic plutons at ~30 Ma the shear sense on W-E striking faults was sinistral. The transition from sinistral to dextral transpressive kinematics is related to the displacement along the Periadriatic fault, which continued at least until 13 Ma (Mancktelow et al., 2001).

East of the sample area, the Austroalpine Unit south of the DAV includes a series of ductile-to-brittle structures developed under low metamorphic conditions referable to the Oligo-Miocene faulting (Linner et al., 2009).

The studied Barrensee mylonitic quartz veins occur in association with a roughly W-E striking steeply-dipping strike slip fault with a strike-length of 300 m at an altitude of ~2850 m (UTM33 326383E/ 5199000 and 326674E/5199000N). The fault is localized in an up to 2 m broad zone with subvertical slickensides with subhorizontal slickenlines, cohesive cataclasites, black ultracataclasites and pseudotachylytes partly over-printed by a ductile SCC' fabric indicating dextral strike-slip kinematics (Figure 2c, d). The fault generally crosscuts the Eo-alpine metamorphic fabric in the host rocks, which is characterized by a complex pattern of refold structures. The investigated samples are from the eastern parts of the fault zone, where the meta-morphic layering is subvertical and parallel to the fault, where the shear displacement is strictly localized in dm-thick foliation-parallel quartz vein forming the precursor structure (Pennacchioni & Mancktelow, 2018) of grey to blueish quartz-mylonites with a subhorizontal stretching lineation (Figure 2a). Up-to mm-size mica fish indicate dextral strike slip kinematics. Interestingly, in the vicinity of the mylonitized veins, no indicati-on of cataclastic deformation, black ultra-cataclasites, pseudotachylites or SCC' fabrics have been observed. Mylonitization of the quartz veins only occurs within the narrow fault zone and ca. up to 4-5 m outside of the central part of the fault zone. Quartz veins further away do not show evidence of mylonitisation.

Materials and methods

The analyses were conducted on thin sections of sheared quartz veins orthogonal to the vein boundary (X-Y plane in the kinematic reference frame) and parallel to the stretching lineation (X-axis). The centre of the pole figures (PF), used for representing the CPO, corresponds to the shear zone kinematic vorticity axis (Y-axis).

We use optical microscopy, SEM-CL and EBSD to characterize the microstructures and CPO of quartz veins across strain gradients from weakly to strongly deformed domains parallel to the vein boundary. Based on CL images, where the CL signal is proportional to [Ti] (e.g. Bestmann & Pennacchioni, 2015; Wark & Spear, 2005), microstructurally-controlled measurements of [Ti] in quartz were carried out by SIMS. The correlation between [Ti] and intensity of the CL signal is corroborated by the SIMS measurements. Wavelength spectral analysis demonstrate that the CL signal depends only on the single emission peak at 400-420 nm (Figure S1). Despite very low [Ti] (0.1-4.7 ppm), CL was perfectly capable of imaging even sub-ppm Ti-variations. Because the highest CL intensities of weakly deformed quartz veins is also reflected in stretched protolithic vein crystals and porphyroclasts in mylonites, we limited our SIMS measurements to these last domains where the whole range of CL/[Ti] are present in association with a diversity of microstructures. Synchrotron-based X-ray fluorescence microscopy (XFM) was undertaken on the XFM beamline at the Australian Synchrotron (Howard, 2020) to identify µm-sized Ti-bearing phase within the vein that buffered the Ti activity.

Optical images in transmitted plane-polarized light and high-resolution SEM orientation contrast (OC) images were used to record the spatial density of small-scale pores (fluid inclusions, FI). This information, in combination with EBSD maps, was aimed at correlating variations in CL intensity (and corresponding variations in [Ti]) across the microstructure with the occurrence of fluids.

The composition of syn- and late-kinematic chlorite (with respect to the mylonitic deformation) was determined by microprobe analysis to apply chlorite thermometry (Vidal et al., 2005; 2006). This provides an independent, complementary estimate of temperature to TitaniQ.

A detailed description of the different analytical apparatus and procedures used in the study is reported in the Data Repository.

Results

Most veins are heterogeneously deformed with strain increasing towards the vein core or show a strain gradient from one vein margin (protomylonite) to the other (ultramylonite). Weakly deformed domains consist of mm-sized vein crystals (qtz_1) (Figure 3). With increasing strain, qtz_1 grains progressively stretched, their long axis rotated into parallelism with the shear plane (vein boundary) and dynamically recrystallized to different degrees depending on their crystallographic orientation (Figure 4). Relict qtz_1 grains persist as porphyroclasts in extensively recrystallized, strongly deformed domains (Figures 5-7). Initially, qtz_1 recrystallized into elongated (aspect ratio up to 10:1, hundred microns long) new grains (qtz_{2A}) (Figure 8). Then, highly sub-structured qtz_{2A} grains underwent mantle recrystallization to smaller (1-10 µm in diameter), equant new grains (qtz_{2B}). At high strains, the microstructure is still heterogeneous: the main foliation, parallel to the vein boundary, is defined by an alternation of dominant, recrystallized layers showing a distinct internal extinction banding (100-500 µm in thickness) and monocrystalline (commonly highly sub-structured) ribbon grains. The recrystallized layers show a CPO characterized by a single c -axis girdle with variable sub-maxima as reflected in the optical extinction banding (Figure 8). The foliation of deformed quartz veins is crosscut at a high angle by late-stage quartz, (qtz_3±chlorite) veins, which were only slightly involved in ductile deformation (Figures. 2b, 9, 10 and Figure S3c). The microstructural and CPO evolution, and the variations in [Ti] across the differently strained domains (imaged by CL and measured by SIMS) are described in detail below.

4.1. Weakly to moderately deformed quartz vein domains

The most preserved domains (Figure 3) contain mm-sized, weakly deformed quartz vein crystals (qtz_1). These "crystals" contain deformation bands, elongated subgrains and deformation lamellae, and show serrate grain boundaries (GB). The qtz_1 CL shade varies from medium to light grey with darker tones at GB (over a thickness of 20-40 µm). XFM element maps reveal dispersed inclusions of rutile grains (3-7 µm grain size) as inclusions inqtz_1 and along pristine microshear zones (Figure S2).

With increasing bulk strain qtz_I grains become (i) stretched to different degrees, depending on their crystallographic orientation relative to the kinematic reference frame, and (ii) separated by shear bands of recrystallized grains (qtz_2). Qtz_I grains show a high spatial density of low angle boundaries (LAB: misorientations < 10-15°). In qtz_I grains with$c$ -axis oriented between the Y and Z-axis, the LAB misorientation axis plot shows clustering around $<c>$ with a spread to the rhomb planes and to the {10-12} direction.Qtz_I grains with a peripheral c -axis orientation in the PF have more random LAB misorientation axes and higher degree of recrystallization. The selected, elongatedqtz_I grain (aspect ratio of 10:1) of Figure 5, with c -axis inclined 37° to the Y-axis in the Y-Z plane, is highly substructured; the LAB misorientation axes cluster around $<c>$ (Figure 5g) and the PF show a continuous dispersion around the {10-12} pole close to the Y-axis (Figure 5g). This qtz_I grain shows a similar CL-shade as the incipiently deformed quartz vein crystals

(Figure 5b, e). In contrast, the recrystallized portions are darker in CL shade (Figure 5e), and associated with high angle boundaries (HAB: misorientation >10-15°) (Figure 5f, k') and pores (Figure 5i, j'). The interior of *qtz_I* grain shows a network of thin dark-grey CL lines (Figure 5e) that matches the LAB network (misorientation 0.5°-15°) of EBSD maps (Figure 5f). There are no visible pores associated with LAB (Figure 5k") in either the optical (Figure 5i) or OC images (Figure 5h, j").

4.2. Strongly deformed domains

Strongly deformed vein portions show a mylonitic foliation subparallel to the vein boundary defined by the alternation of layers of (i) dominant, recrystallized aggregates of $qtz_{2A,B}$ with slightly different CPO reflected in the extinction banding, and (ii) monocrystalline, ribbon grains. This layering is partially reflected in a CL-shade layering (Figure 9a). The foliation wraps around local, mm-sized qtz_1 porphyroclasts (Figure 4). In the following we highlight the correlations between the CL-patterns and [Ti] with the CPO, (sub)grain size and porosity distribution.

4.2.1. Qtz_I porphyroclasts

Most of the qtz_1 porphyroclasts have a nearly peripheral *c* -axis orientation in PF, slightly rotated to the Z-axis against the sense of shear (Figure S3). Two different microstructural sites (*Site 1, 2*) have been selected for detailed study. *Site 1* (Figure 6) shows a cluster of qtz_1 porphyroclasts (I-IV) mostly retaining the medium-light CL-shade of qtz_1 of weakly deformed vein portions, corresponding to 3.6-4.1 ppm [Ti] (*SIMS-profiles 8-11, 13, 14*). Pores are rare or absent within the clast. As a whole the cluster defines a composite low-strain domain with the wrapping recrystallized qtz_2 matrix showing CL variation between the contractional and extensional domains, developed at opposite quadrants around the porphyroclast cluster and induced by distortion in the non-coaxial (dextral) flow. The contractional domains show medium-dark CL shade and 1.3-2.7 ppm [Ti] (*SIMS-profiles 10, 15*). The extensional quadrants, including the recrystallized domain between I and III, show darker CL shade and 0.4-0.5 ppm [Ti] (*SIMS-profiles 7, 12*). These CL/[Ti] patterns well correlate with the density of HAB pores, higher in the Ti-poorer extensional domains (Figure 6a, d). The separation zone between porphyroclasts I and II (Figure S3) shows heterogeneous CL patterns with (i) larger irregular portions, partially retaining the typical CL-shade of qtz_1 , and (ii) CL-darker domains. The formers are highly sub-structured, contain scarce pores and show a trend of decreasing [Ti] (1.3-2.2 ppm) from the values of the porphyroclast cores. The CL-darker domains include new qtz_2 grains, have higher pore spatial density (Figure S3) and show lower [Ti] (0.4-0.7 ppm). Porphyroclast II locally shows decreasing CL intensity towards the rim (up to 50 µm in width; Figure 6f), in association with highly sub-structured domains (Figure 6h) almost free of pores (Figure 6g), corresponding to a progressive decrease of [Ti] from 3.0-4.0 ppm (clast interior) to 1.1 ppm (clast margin) (Figure 6a, *SIMS-profile 13*). [Ti] decrease to 0.9 ppm in the adjacent recrystallized pore-rich qtz_2 aggregate.

Site-2 shows a qtz_1 porphyroclast partially separated in two parts by a wedge-shaped domain of recrystallized qtz_2 (Figure 7). The upper part has moderate-light CL shade and 3.3-3.7 ppm [Ti] (*SIMS-profiles 3, 5, 6*). The presence of localized pore clusters associates with darker CL shade (Figure 7c). The lower porphyroclast part shows a more heterogeneous CL pattern corresponding to a larger variation in [Ti] (2.0-3.9 ppm; *SIMS-profiles 1, 4, 5*). The set of thin CL-brighter lines corresponds to deformation lamellae (Figure 7g, h). The dividing recrystallization qtz_2 aggregate shows homogenous dark CL shade, 0.2-0.5 ppm [Ti] (*SIMS-profiles 2, 4, 5*) and abundant HAB pores (Figure 7c, g, h). The CPO of the recrystallized aggregate consists of an oblique, single girdle with *c* -axis Y-maximum and peripheral sub-maxima (nearly overlapping with the host grain CPO) linked to low-strain tip of the recrystallized aggregate (Figure 7f). There is no noticeable change in CL signal within the porphyroclast associated with the strain gradient towards the tip of the recrystallized aggregate (Figure 7f-h, ellipse). A dark CL shade is also observed for very thin (single-grain-thick) micro-shear zones of recrystallized qtz_{2B} showing HAB porosity (Figure 7f-h, black arrow). There is also no noticeable change in CL between recrystallized aggregates of qtz_{2A} and qtz_{2B} .

4.2.2. Monocrystalline lenticular quartz

Qtz_1 grains are progressively stretched into lenticular, high aspect-ratio, monocrystalline grains bending into the mylonitic foliation subparallel to the vein boundary. *Qtz₁* grains less favourably oriented for prism$<a>$ slip (c -axis angle to Y: >54°) tend to recrystallize as soon as the clasts bend into the shear foliation (*ribbon-clast-1, 2* in Figure 9a and Figure S4). This goes along with the overall change to darker CL-shades associated with the appearance of a high spatial density of HAB pores. The recrystallized grains commonly contain brighter CL remnant cores. Extensive recrystallization is especially observed for ribbon-clasts with c -axis at the PF periphery (*ribbon-clast-1*). Instead of a main clustering of LAB misorientation axis parallel to $<c>$ a tendency around $\{m\}$ is evident suggestive of basal$<a>$ and/or $\xi<c+a>$ slip (Neumann, 2000) (Figure S4c-I). Deformation zones, showing different degree of recrystallization, are commonly localized between the ribbon-clasts. However, independently of the accommodated amount of strain, the localized zones reveal a resetting towards low CL intensities and low [Ti] (0.3-1.0 / 1.8 ppm; *SIMS-profile 13* , Figure 9a).

4.2.3. Ribbon grains

In general, ribbons preserve a light CL-shade similar to, or slightly darker than, that of qtz_I grains (Figure 9a). The corresponding [Ti] vary between 3.0-4.7 ppm (lighter ribbons: *ribbon-1, 2*) and 1.6-3.2 ppm (darker ribbons: *ribbon-3, 4*). All ribbons contain a high spatial density of LABs (Figure 9b-IV, Figure S5d) with a main cluster of misorientation axis around $<c>$ and additional clusters are towards $\{r\}/\{z\}$ and $\{\xi\}$, even for misorientation angles >10-15° (Figure S4c-I *ribbon-4*). The internal HAB are mostly not interconnected. The cellular-structure with a high CL shade present within some ribbons (e.g. *ribbon-2* , Figure 9, Figure S4) corresponds to LABs not associated with detectable [Ti] variations; this structure likely corresponds to intrinsic lattice defects of SGB (Hamers et al., 2017). Ribbons with the c -axis next to the Y-axis (c -axis angle to Y [?] 25deg; *ribbon-2*) are the most elongated ones (up to 1 cm long and 250 µm thick) (Figure S4a, c-I). The LAB misorientation axis are subparallel to $<c>$ and correspond to prism$<a>$ slip (Neumann, 2000). Ribbons with c -axis orientation between Y and Z (angle 40-44°) show a main clustering of LAB misorientation axes (sub)parallel to $<c>$ but also towards $\{r\}$ and $\{z\}$; this is suggestive of both prism$<a>$ and rhomb$<a>$ slip (Neumann, 2000). These grains show a higher degree of recrystallization at their ends where the CL signal gets weaker. In general, ribbons are nearly free of porosity (Figure 9b-II), except for some specific clusters and in zones of incipient recrystallization.

4.2.4. Strongly deformed, pervasively recrystallized aggregates

Pervasively recrystallized aggregates are characterized by extinction banding and corresponding CL variations (layer thickness 100-500 µm) (Figure 4a, b and Figure 9). The CPO of the different layers indicate a variation in the distribution of the c -axis submaxima within the c -axis girdle, mainly located between the Y and Z direction of the PF (Figure S4c-II). The distribution of LAB misorientation axes mainly cluster around $<c>$. We used the density of the clustering (multiple of random distribution, *mrd* , for misorientation angle interval 2-10°) to quantify the activity of slip system, especially prism$<a>$. The *mrd* values varies for different CPOs (position of the c -axis sub-maxima). In general, the closer the c -axis sub-maxima is to the Y-axis the higher is the *mrd* . For some (ultra)mylonitic areas there is a tendency that layers with dark CL show higher *mrd* values, corresponding to c -axis clustering towards Y-axis (e.g. *mylonite-5* - dark CL, *mrd* 4.2; Figure S4c-II). Adjacent layers with a brighter CL signal are characterized by lower *mrd* values and more peripheral c -axis sub-maxima in PF (*mylonite-3* and *6* – brighter CL, *mrd* 2.9 and 2.8). The darker CL layers commonly display a higher degree of smaller (sub)grain size and accompanied higher pore spatial density than CL-brighter layers. However, this is not always true and no strict correlation between CL, CPO, misorientation axis distribution, (sub)grain size and FI density can be demonstrated. For example, *area-A* is completely recrystallized where a layer with brighter CL signature (thickness 300 µm) is surrounded by either sides by layers with darker CL signature (Figure 8). However, the brighter CL *layer-2* shows a cluster of c -axis in the centre of the PF (Y-axis), whereas the c -axis sub-maxima of the adjacent *layers-1* and *3* (dark CL) tend to localize further away from Y and/or a located near the PF periphery. This is also reflected by the *mrd* values of the LAB (clustering around $<c>$) showing higher values for *layer-2* (mrd 7.45) compared to lower values for the adjacent *layers-1* (*mrd* 4.58) and *layer-3* (*mrd* 5.29). Further, all three layers show the same (sub)grains size distribution and there is no obvious variation of the FI density. FI occur mainly along HAB but are also present along LAB (Figure 8f, g).

In sample (*MS-09a*) strongly deformed vein portions show a characteristic extinction banding but a relatively minor corresponding CL variation (Figure 4c, d). With respect to *qtz1*of weakly deformed parts the mylonitic aggregate have a slightly to moderately decreased CL-shade (Figure 4d). A strong reduction in the CL signal is only observed in strain shadows between coarse quartz clasts (Figure 4g, h). It is important to note, that only the microstructures with a dark CL signal contain a high spatial density of pores. In contrast, the (ultra)mylonitic matrix with its relatively homogeneous moderate CL signal is characterized by a very low FI density, where only sporadically FI are evident along HAB.

The SIMS data reveals very homogenous low [Ti] (0.3 – 0.6 ppm) for the dark CL layers (Figure 9a). The brighter (ultra)mylonitic CL layers are more heterogeneous in the [Ti] (0.8-2.2 ppm) which is also reflected by the heterogeneous CL microstructure. Many of the elongated recrystallized grains show brighter CL cores and darker structures along the HAB especially where FI are evident. In general, CL intensity can vary within and between these layers.

4.3. Late-stage quartz (LSQ, *qtz3*) veins

Late-stage quartz (LSQ) veins (locally accompanied by chlorite) crosscut the main foliation of the deformed quartz veins. These veins are easily identified in CL images by their dark, homogeneous shade crosscutting the CL banding of the deformed vein (Figure 10a, e). Thin LSQ veins can be easily overlooked under the optical microscope due to the epitaxial growth of the quartz infilling on the host-vein quartz. These veins are slightly involved in ductile deformation and show the same type of deformation features as the hosting quartz and therefore are called syn-kinematic late stage quartz veins. In Figure 10f the host ribbon grain (*qtz1*) and the filling of the crosscutting vein (*qtz3*) show (i) the same dispersion patterns of the CPO in PFs, and (ii) similar clustering around $<c>$ and around the Y-axis in the misorientation axis plots in crystal and sample coordinates, respectively. Only minor dynamic recrystallization is recorded in the LSQ veins as result of the small accumulated strain. The homogeneous, dark CL shade corresponds to [Ti] in the range of 0.1-0.5 ppm (mainly 0.1-0.3 ppm) (*SIMS-profile 5, 6, 11* and *12* in Figure 10a).

4.4. Chlorite thermometry

We applied chlorite thermometry (Bourdelle, 2021) in order to have an independent information on the deformation temperature to complement the Ti-in-quartz estimates. This method has been shown to be particularly efficient for determining deformation temperature in the greenschist facies (Calzolari et al., 2018; Cantarero et al., 2014; Lacroix et al., 2012; Mizera et al., 2020; Zihlmann et al., 2018). We used the calibration of Vidal et al. (2005; 2006), which is based on two independent internal equilibria amongst the end members of the chlorite solid solution in presence of quartz and H_2O (see Ganne et al., 2012 for calculation details).

Chlorite from the investigated samples were classified from microstructural observation as pre-, syn- and late-kinematic with respect to the mylonitic deformation event of the quartz veins. Syn- and late-kinematic chlorites from three different microstructural sites in three sample (Figure S6) were analyzed with an electron probe microanalyzer (see Data Repository for method). An equilibrium temperature was calculated for each analysis, assuming a pressure of 0.3 GPa (see *section 5.3.2.2.* for explanation, Table 1). Syn-kinematic chlorite from shear bands and strain shadows (Figure S6a) yielded values between 238 and 268 °C. Chlorite growing in garnet cracks as retrogression product is interpreted as syn- to late-kinematic (Figure S6b) and yielded temperatures in the range 272-352 °C. The unoriented chlorite from a late-stage syn-deformational quartz veins crosscutting the mylonitic foliation (Figure S6c, see *section 4.3*) yielded temperatures between 265 and 333 °C.

A minimum error of 30 °C (Plunder et al., 2012) to 50 °C (Powell & Holland, 2008) should be applied to results of thermometry. Increasing the input pressure to 0.5 GPa induces an increase of the sample average temperature lower than 10 °C and changing the range of accepted ferric iron indicates that the impact of this parameter remains within 50 °C. With an uncertainty of 50 °C, the average temperatures in the three microstructural sites overlap within error, implying that syn- and late-kinematic chlorite grew at similar conditions. Only one sample yielded temperature consistently below 300 °C (Table 1). Owing to the irregular surface of chlorite in shear bands and strain shadows in this sample (Figure S6aIII) and the small number of analyses, less weight should be put on this sample. We therefore conclude that chlorite thermometry provides a reasonable estimate of 300±50 °C for the deformation temperature, most likely in the upper part of this range.

5. Discussion

5.1. Conditions of quartz vein formation and deformation

The development of the Barrensee quartz veins has been referred to amphibolite-facies conditions, constrained at 510-590 °C and 0.5-0.6 GPa (Linner, 1999). The quartz veins were later exploited as ductile shear zones along a sub-vertical ca. W-E-striking pseudotachylyte-bearing fault/shear zones, with dextral strike-slip kinematics, cutting discordantly the main foliation of the host rocks. A strike-slip kinematics, and the association with pseudotachylytes, is typical of the Oligocene-Miocene faulting in the Austroalpine and Penninic units of the Eastern Alps (Ceccato & Pennacchioni, 2018; Mancktelow et al., 2001). These strike-slip faults, including major faults like the DAV fault (Mancktelow et al., 2001), accommodated shortening and the lateral escape of the Alpine stack at the front of the Dolomites block (Southern Alps) indenter (Ratschbacher et al., 1989). Since only dextral shear sense is recorded in the mylonites and the brittle fault rocks, the shear zone most likely belongs to the dextral Periadriatic fault system active after 30 Ma (Mancktelow et al., 2001). This postdates the Cretaceous/Paleocene exhumation constrained by biotite Rb/Sr ages (Linner, 1999) and indicates that deformation took place at the basal part of the upper crust, consistent with (i) the temperatures estimated from the chlorite thermometry, and (ii) the occurrence of ultra-cataclasites and pseudotachylytes coeval with ductile shearing in the quartz veins. Alternatively, the mylonitization of the quartz veins could have happened earlier during the Cretaceous/Paleocene exhumation and the investigated fault exploited the mylonitic foliation as a pre-existing anisotropy in a favourable orientation for brittle-ductile strike-slip in the Oligocene/Miocene. However, the mylonitic quartz veins have only been observed in the investigated fault and the mylonitic quartz veins do not record any evidence of cataclastic reworking and therefore we favour the interpretation that mylonitization of the quartz veins was coeval with brittle-ductile strike-slip faulting at low-greenschist facies conditions.

5.2. Resetting of [Ti] during deformation

Resetting of [Ti] from initial 3-4 ppm of coarse-grained qtz_1 grains down to 0.3-0.5 ppm of recrystallized qtz_2 grains in strongly deformed domains is heterogeneous. Two main factors apparently caused resetting: (i) the amount of fluid in combination with dynamic recrystallization, responsible for the strongest resetting, and (ii) the development of SGB. The SIMS analysis have established the univocal correlation between the CL signal and [Ti]. In the following we use the term resetting to indicate the decrease of the [Ti] with respect to that of pristine vein quartz crystals, corresponding to change to darker CL grey shades. We discuss the influence of different parameters (fluids, recrystallization, CPO, clast orientation, strain, and available) on the [Ti]/CL resetting.

5.2.1. Effect of fluids

Synkinematic infiltration and/or re-distribution of free aqueous fluids (e.g. released from FI of the protolithic quartz vein grains during deformation) played a major role on [Ti] resetting. The main mechanism producing grain-scale fluid pathways is SGR recrystallization resulting in a pervasive network of fluid-permeable grain boundaries (GB). As a result, there is a general switch to dark CL-shades and low [Ti] from qtz_1 grains to qtz_2 recrystallized aggregates. GB permeability is witnessed by widespread occurrence of pores along HAB, as reported in other quartz mylonites (Fitz Gerald et al., 2006). In contrast, LAB are either free of porosity or show only a minor porosity. The syn-kinematic timing of fluid infiltration is well documented in Figure 6a, where there is a distinct degree of [Ti] resetting, in the recrystallized quartz matrix surrounding the composite quartz porphyroclast, between the low pressure domains (preferential sink of fluids and with stronger resetting) and the high pressure domains (weaker resetting) (see schematic stress field, marked in Figure 6a). The contrast in CL shade between extensional and contractional sites is not associated with a change of CPO of the qtz_2 aggregate or of the active slip systems (Figure 6a-c). [Ti] resetting along GB commonly affects a thickness of as much as several tens of micron of the grains (Figure 6a, Figure S3). This may result from a component of dissolution-precipitation in the recrystallized aggregate accompanying the predominant SGR recrystallization. An enhanced resetting may result from a combination of diffusion creep (pressure solution) and the movement of HAB through the strained aggregate in the dislocation creep regime accompanied by SGR recrystallization (Yund & Tullis, 1991). Complete resetting is also evident even when the degree of recrystallization and the strain are low (Figure 7f-h, ellipse) or is strictly localized along interconnected HAB (black arrow). On the other hand, in high strain zones at the compressional quadrants around clasts the GB fluid was drained and moved to extensional and dilatant zones under microscale pressure gradients (Figure 6a). Therefore, in compressional quadrants resetting took place to a minor extent despite the persavive dynamic recrystallization (see also *section5.2.1.3*). In contrast, within strongly localized and recrystallized microstructures, e.g. shear bands in the protomylonites (Figure 4a-d; Figure 5a, b) or in clast-related microstructures in the (ultra)mylonites (Figure 4d, h), available fluids were channelized and promoted a strong resetting.

Along GB, but locally also along SGB, a CL gradient towards the grain interior is observed. Cherniak et al. (2007) showed that diffusion distances are limited at low temperatures. Ti volume diffusion over a distance of 1 µm should take more than 1 Ma at ˜300 °C (the inferred deformation temperature of the Barrensee quartz veins). This diffusion rate is too sluggish to explain the observed 3-10 µm-thick [Ti] zonation. However, dislocations can act as fast diffusion pathways – a process known as pipe diffusion (Legros et al., 2008). Most diffusion experiments have been carried out under static condition and therefore probably underestimate diffusion rates of deformation microstructures (Chakraborty, 2008, and references within). In deformation experiments, Yund et al. (1981) concluded, based on dislocation density gradients, that pipe diffusion enhanced diffusion coefficient for oxygen and therefore promoted faster chemical exchange in albite. Piazolo et al. (2016) showed direct evidence by atom probe tomography that trace elements within deformed zircons are concentrated along dislocations piled up at SGB. For the Barrensee quartz veins the [Ti] are too low to carry out atom probe analysis. However, since CL gradients mainly occur where GB and SGB are correlated with a high FI density we presume that diffusion is promoted by the presence of fluids in any case.

5.2.1.2. Effect of subgrain boundaries

Resetting related to SGB ranges from (i) a strongly localized effect along individual SGB to (ii) a nearly homogeneous effect in strongly substructured (high spatial density of SGB) domains. In both cases, an associated porosity is basically absent, and the degree of resetting is minor compared to wetted GB and SGB.

Local [Ti] resetting along SGB

In Figure 5e the network of thin dark-grey CL lines within the qtz_1 grain correspond with the LAB network. Dislocations along SGB can cause non-bridging oxygen hole centre defects under electron irradiation and act as intrinsic defects producing a 650 nm emission peak in the red wavelength range in quartz (Hamers et al., 2017 and references within). However, the above described CL network is not visible using a red filter (600-700 nm) therefore excluding that intrinsic defects are responsible for the observed feature. We refer the dark-grey CL network to [Ti] variations associated to diffusion along SGB. Note the strongly localized reduced CL signal along SGB is too small for SIMS analysis (beam spot size ca 10x15 µm, see methodical section in Data Repository). Nachlas et al. (2018) observed that Ti-undersaturated coarse-grained quartz clasts, experimentally deformed in a fine-grained Ti-saturated quartz matrix, show slightly higher CL intensities along SGB and to some extent also a broader diffusion pattern from the SGB into the host grains.

Homogeneous [Ti] resetting in areas with high SGB density

The observed partial resetting along stretched qtz_1 margins (up to 50 µm, Figure 6a, f) cannot result from the sluggish volume diffusion of Ti within intact quartz at greenschist facies conditions (see above and *section 5.2.1.*). Rather synkinematic rearrangement of SGB and migration within the relatively highly strained grain margins can explain the process of resetting. SGB migration was observed in metals, analogue materials (Drury et al., 1985; Urai et al., 1986) and in rock-salt (Bestmann et al., 2005). Because SGB do not show any associated porosity, this type of resetting seems not to imply a role of fluids, at least at the submicron level. Nachlas et al. (2018) argued that SGB migration is also able to reset the deformed parts of the grain, where SGR recrystallization is evident, to uniform higher [Ti] with respect to the host with original lower [Ti].

5.2.1.3. Effect of clast orientation, strain, recrystallization and available fluid in strongly deformed vein portions

Highly strained quartz-ribbons with high SGB spatial density and misorientation axis around $<c>$ preserve the pristine CL/Ti signal (e.g. *ribbon-2,* Figure 9a). This was also observed in the experiments of Nachlas et al. (2018). Therefore, continuous SGB rearrangement by mainly prism$<a>$ slip, not leading to dynamic recrystallization, allows homogeneous crystal deformation without resetting. Only marginal resetting takes place with the nearly FI-free quartz ribbons acting as barriers for fluids. However, at incipiently recrystallized ribbon-tips, a higher FI density is evident and is associated to a stronger resetting.

In the ultramylonite with the characteristic extinction banding there is no strict correlation between [Ti]/CL and the CPO (LAB misorientation axis and related slip systems), the FI density and the (sub)grain size (Figure 9, Figure S4). However, the original orientation of the vein crystals apparently plays a major role for the microstructural evolution during increasing deformation (Ceccato et al., 2017). The degree of the [Ti] resetting depends strongly on the amount of the available fluids, and only to a minor degree on the "cycles" of dynamic recrystallization (Figure 4d). A strong resetting occurs where fluids were channelized (shear bands) or concentrated in dilatant sites (Figure 4d) in combination with recrystallization and dissolution-precipitation (Bestmann & Pennacchioni, 2015). At comparable strain/recrystallization microstructures with lower fluid/rock volume ratio show minor [Ti] resetting than the ones with a high fluid/rock volume ratio (Bestmann & Pennacchioni, 2015). Thus, the moderate and incomplete resetting took place under relative dry conditions due to continuous rearrangement and movement of SGB and GB during ongoing cycles of SGR recrystallization. Ashley et al. (2014) and Bestmann & Pennacchioni (2015) already suggested the importance of an inter-crystalline fluid to promote Ti-removal from quartz during deformation by SGR recrystallization.

In summary, under conditions where SGR recrystallization and prism $<a>$ intracrystalline slip are predominant, deformation-induced resetting of Ti in the deformed quartz veins remains heterogeneous up to high strain and pervasive recrystallization. The different crystallographic orientation of the vein crystals determines whether quartz persists as relatively low-strain porphyroclasts or stretches into mono-crystalline ribbons or recrystallizes to mylonitic aggregates. Dynamic recrystallization by SGR represents an efficient process to dramatically increase the GB surface area per unit volume and, especially, results in an invasive permeability network, allowing fluids to reach grain interior, and decreasing the diffusion length for compositional exchange. In fact, HAB commonly host GB fluids and, therefore, recrystallization enhances permeability and fluid-assisted Ti re-equilibration. Microscale strain heterogeneities also result in pressure gradients that guide fluid redistribution and differential Ti re-equilibration between fluid-rich and fluid-poor domains even in fully recrystallized aggregates. In fact, fluids appear the main agent of Ti re-equilibration. In contrast to HAB, LAB are in most cases impermeable to fluids and induce only subordinate Ti re-setting. In mylonites, containing recrystallized highly elongated grains qtz_{2a} surrounded by small qtz_{2b} grains, commonly show a CPO banding, reflecting the derivation from original crystals with different crystallographic orientation that control the selective activation of the main intracrystalline slip systems. This CPO banding is in part reflected in the Ti re-setting indicating that the CPO affects the strength and fluid redistribution in dependence of the original orientation of the vein crystals and the amount of strain within each band, and finally the amount of fluid.

5.2.2. Influence of late-stage syn-deformational quartz veins

The fluid infiltration associated with the formation of the late-stage quartz (qtz_3) veins does not have any significant effect on the [Ti]/CL signature of the crosscut mylonitic fabric. The crosscutting new qtz_3 veins show a homogenous dark CL shade sharply in contact with the CL banding of the host quarzt vein (qtz_1 ,

qtz_2) except for a very limited, micron-scale halo in contact to the ultramylonite (Figure 10c). This indicates that fluid percolation across the quartz veins was actually only effective during synchronous mylonitization by crystal-plastic deformation. The evolving grain-scale microstructure during flow (especially associated with new GB formation by SGB recrystallization) provided transient and mobile porosity allowing fluid transport. This is consistent with the observed partitioning of fluids along pressure gradients induced by flow perturbation around porphyroclasts.

5.3. Application of TitaniQ

5.3.1. TitaniQ of quartz vein formation

TitaniQ calibrations (Huang & Audétat, 2012 – HA12; Thomas et al., 2010 – TH10;) are based on synthetic quartz grown from silica-saturated aqueous fluid in presence of rutile. Synchrotron analysis of the Barrensee veins reveals the occurrence of rutile inclusions in coarse quartz vein crystals and within recrystallized shear bands. This constrains TiO_2 activity (a_{TiO2}) to unity (e.g. Thomas et al., 2010). Assuming the pressure estimates of Linner (1999), the TH10 of pristine [Ti] (3.0-4.7 ppm) preserved in deformed quartz clasts yields 388-410 °C (0.5 GPa) and 405-427 °C (0.6 GPa). HA12 results in approximately 100 °C higher temperatures, 492-519 °C and 507-534 °C. The TH10 calculations are far below the vein crystallization temperatures (510-590 °C) inferred by Linner (1999).

5.3.2. TitaniQ of quartz vein deformation

5.3.2.1. Influence of deformation processes and related microstructures for Ti-in-qtz re-equilibration

Several studies have shown that SGR recrystallization is inefficient to cause [Ti] re-equilibration (e.g. Ashley et al., 2013; Grujic et al., 2011). Grujic et al. (2011) concluded that only grain boundary migration (GBM) above ~540 °C causes a complete [Ti] resetting. Nachlas et al. (2018) showed experimentally that SGB migration is able to promote [Ti] resetting. Haertel et al. (2013) inferred that, during retrograde deformation, SGR together with fluid-mediated bulging recrystallization were capable of re-equilibrating [Ti] at 350-400 °C, but concluded that the sole SGR recrystallization did not. All these studies inferred that SGR recrystallization represents a structural rearrangement of the lattice coupled with grain size reduction, but does not involve SiO_2 transport and, therefore, is not efficient for [Ti] re-equilibration. Further, the duration (cycles) of dynamic recrystallization and the amount of strain were inferred to play an important role in [Ti] resetting (Ashley et al., 2014; Bestmann & Pennacchioni, 2015; Kidder et al., 2013; Nachlas et al., 2015). In this view, ultramylonites (i.e. portion of nearly complete dynamic recrystallization) should represent the best candidates for applying TitaniQ. Here we show that the amount of free fluids percolating through the specific microstructure (especially along GB) is critical in controlling [Ti] resetting. Not a precise strain threshold is essential, instead an almost complete resetting occurs along wetted HAB and/or where dilatation sites provided sinks for fluids and synkinematic quartz precipitation (Bestmann & Pennacchioni, 2015; Haertel et al., 2013). In those microstructures the [Ti] (0.2-0.3 ppm) is in the same range as in (ultra)mylonitic layers (showing high FI density) characterized by homogeneous low dark CL and corresponding homogeneous low [Ti] (0.3-0.6 ppm).

5.3.2.2. Application of TitaniQ to (ultra)mylonites

As discussed above (*section 5.1*), it can be reasonably assumed that the Barrensee veins were deformed at the base of the brittle-ductile transition of the crust, ~300-350 °C that roughly occurs at 10-12 km depth (e.g. Hirth & Beeler, 2015), corresponding to ~0.3 GPa. Acosta et al. (2020) pointed out that HA12 was experimentally calibrated at lower pressure (0.1-1.0 GPa) than TH10 (0.5-2.0 GPa), and should ideally be more suitable for the Barrensee quartz veins. At 0.3 GPa, the temperatures calculated with the 2 calibrations differs of ca. 70-100 °C for a [Ti] range of 0.2-0.6 ppm and for an a_{TiO2} range of 0.1 and 1 HA12 yields systematically higher temperatures. Provided the assumed ambient conditions of ~300-350 °C are correct, temperature values in this range are obtained with HA12 with $a_{TiO2} = 1$ (320-369 °C) or with TH10 with $a_{TiO2} = 0.2$ (305-355 °C). If our multi-methodological microstructural analysis allows identification of proper sites of compositional re-equilibration for TitaniQ, the use of the HA12 and TH10 calibrations need to have a rigorous constrain on the Ti activity for the application of the thermometer (and the choice of the appropriate calibration). Small rutile inclusions are present within the coarse quartz vein crystals as well as along the crosscutting MSZ showing the same dark CL-shades as the ultramylonitic samples analysed by SIMS (Figure S2g, h). Further, during dynamic recrystallization rutile inclusions within qtz_I grains are exposed into the qtz_2 matrix and get in contact with the GB fluid. Therefore, we infer that mylonitic deformation occurred under Ti-saturated conditions due to water-assisted rapid diffusion along the interconnected GB network (Bromiley & Hiscock, 2016; Farver & Yund, 1991; Nachlas et al., 2018; Thomas & Watson, 2014). In summary, the calculated temperature of 320-369 °C using HA12 (as the low-pressure TitaniQ calibration) and $a_{TiO2} = 1$ apparently represents the most reliable estimate for the mylonitization of the Barrensee quartz veins.

5.4. Temperature estimates vs. quartz microstructure in the Barrensee quartz veins: a paradox?

In the deformed Barrensee quartz veins, subgrain rotation (SGR) and accordingly SGR recrystallization was the dominant deformation process and prism$<a>$ the easiest intracrystalline slip system (Figure 8d and Figure S4cI+II) (Neumann, 1999). Despite a recrystallization process and a CPO cannot be taken as univocal representative of a specific temperature range, SGR recrystallization and prism$<a>$ slip have been commonly described for quartz at upper greenschist to amphibolite facies deformation conditions (Behr & Platt, 2011; Ceccato et al., 2020; Stipp et al., 2002). Ceccato et al. (2020) constrained in the range 420-460 °C, by petrologic pseudosections, the deformation of quartz (by dominant SGR and prism $<a>$ slip) within different granitoid plutons (Adamello, southern Alps: Pennacchioni et al., 2010; Sierra Nevada, California: Pennacchioni & Zucchi, 2013; Rieserferner, Eastern Alps: Ceccato et al., 2020). In study cases where deformation occurred over a temperature range (e.g. 250–700 °C in the Tonale shear zone: Stipp et al., 2002; 300–550 °C in the Whipple Mountains core complex: Behr & Platt, 2011) the intracrystalline slip system is observed to evolve from prism $<a>$ at high temperature/low stress to a mixture of basal $<a>$, prism $<a>$, and rhomb $<a>$ at intermediate temperatures and stresses to basal $<a>$ at low temperatures/high stresses. At low temperatures for crystal-plasticity of quartz (250-300 °C) recrystallized quartz display a basal $<a>$ fabric (Kirschner & Teyssier, 1991).

The examples selected above support the widely shared opinion that SGR and prism $<a>$ record temperatures significantly above the limit of crystal-plasticity of quartz (at around 250 °C: Stipp et al. 2002). This rises a major, provocative query as to whether the deformation temperatures inferred here for the Barrensee quartz vein mylonites are correct or not. Different observations converge on lower greenschist facies temperatures for the shear/fault zone deforming the quartz veins: (i) the strike-slip kinematics and the association with coeval pseudotachylytes typical of the Oligo-Miocene faults in the region (Ceccato & Pennacchioni, 2018; Mancktelow et al., 2001); (ii) the chlorite thermometry; (iii) the TitaniQ thermometry. All these constraints are individually disputable, but together represent a more robust indication towards low temperature conditions of deformation. This is a relevant question that should be addressed in future research. If the assumed temperature of deformation underestimates the actual one, this results in a critical assessment on the reliability and applicability of the TitaniQ as previously discussed by Asley et al. (2014) and Bestmann & Pennacchioni (2015). This would imply that the experimental calibration of the TitaniQ is not applicable to the natural mylonite, despite the sites of most complete strain-induced [Ti] resetting may be identified by a rigorous microstructural s.l. analysis. On converse, if the assumed temperature of deformation is correct, this implies a revision of the commonly assumed temperature range for dominant dislocation creep, SGR recrystallization and prism $<a>$ slip with the lower limit moved to lower temperatures than commonly expected.

6. Conclusions

The study of the Barrensee quartz veins (Prijakt Nappe, Austroalpine Unit, Schober Mountains, Eastern Alp) indicates that deformation-induced Ti-in-quartz resetting is possible in the regime of subgrain rotation (SGR) recrystallization. Field constrains and chlorite thermometry suggest that quartz vein deformation occurred at low temperatures ([?] 350 degC) in the ductile field at the base of the brittle crust. The microstructural complexity of the quartz mylonites requires a careful selection of the domains of most complete re-equilibration for applying TitaniQ. This is only possible through a detailed correlated analysis by optical and SEM (cathodoluminescence, CL; orientation contrast, OC; and EBSD) microscopy as necessary prerequisite to Ti measurement. The measured Ti concentration [Ti] in most complete re-equilibrated mylonitic domains (e.g. strain shadow or shear bands) yield consistent TitaniQ temperatures for the condition close to the brittle-ductile transition and rutile-buffered Ti activity. This is unusual for SGR and prism $<a>$ slip, considered to pertain to higher temperature ranges of quartz deformation. If the temperature estimate in our study is correct, our results undermine this commonly agreed belief and have profound implications in the interpretation of quartz microstructures. Future work should search for additional constrains of the temperature conditions of the quartz vein deformation.

Acknowledgements

This work was funded by the Deutsche Forschungsgemeinschaft DFG (BE 2413/3-1). GP acknowledge funding from the University of Padova (BIRD175145/17). Access to the SEM-EBSD facilities was provided by the Department of Werkstoffwissenschaften WW1, FAU Erlangen-Nurnberg, Germany. The Oxford Instruments CMOS-Symmetry EBSD detector was funded by the DFG (JA 2718/3-1). Jay Thomas is thanked for providing the synthetic Ti-doped quartz standard (QTiP-38, Ti 380 ppm), Djordje Grujic for the natural standard (TN-06, 0.3 ppm) and Steven Kidder for the Herkimer "Diamond" used as a Ti blank. Cees-Jan De Hoog is thanked for conducting SIMS measurements and processing at the School of Geosciences of the University of Edinburgh. We acknowledge Holger Stunitz for discussion and providing access to the SEM-CL spectra facilities at the Department of Geosciences at the Arctic University of Norway (Tromso), and Amicia Lee and Tom-Ivar Eilertsen for their assistance. Christoph E. Schrank and Nicholas W. Phillips are thanked for their contribution with respect to the synchrotron data set. Part of this research was undertaken on the XFM beamline at the Australian Synchrotron, part of ANSTO. Rene Romer is thanked for support during electron microprobe analysis (chlorite thermometry) and Friederike Urban and Raphael Njul for sample preparation. Alexis Plunder is thanked for the chlorite thermometry blind test.

Data Availability Statement

The EBSD, WDX, SIMS and Synchrotron X-ray Fluorescence data used in this study are publicly available at http://doi.org/10.5281/zenodo.4923150

Appendix A. Supplementary material

Supplementary material related to this article can be found online at ....

Author contributions

M.B., G.P. and B.G. conceived the idea, undertook fieldwork and contributed to equal parts to the discussion and interpretation of the data set. M.B. carried out sample preparation, microstructural analysis by light microscopy, scanning electron microscopy (SEM-CL, SEM-CL spectra, SEM-OC, EBSD) & processing, electron microprobe (EMP) and worked out the workflow for Ti-in-qtz analysis by Secondary Ion Mass Spectrometer (SIMS, in cooperation with Cees-Jan De Hoog). B.H. processed the EMP data and applied the chlorite (Chl) thermometer. B.H. and B.G. constrained the deformation condition based on Chl-thermometry data and the geological setting. M.B. applied the TitaniQ thermometer. M.W.M.J. and C.M.K collected and analysed the X-ray Fluorescence Microscopy data. M.B. wrote the ms with the contribution of B.G. and G.P. B.H. wrote the chlorite thermometry part and M.W.M.J. the synchrotron methodical part in the Supplementary Material.

Declaration of competing interest

The authors declare that they have no known competing financial interests or personal relationships that could have appeared to influence the work reported in this paper.

Figures

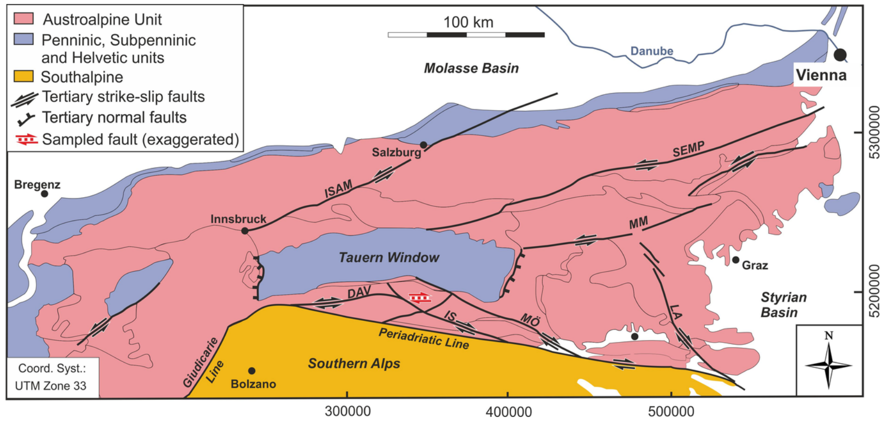

Figure 1 . Simplified geological map of part of the Eastern Alps (modified after Schuster et al., 2014). Important Tertiary fault systems are given. Note sampled fault (red stippled line) is a continuation in strike of the Defereggental-Anterselva-Valles fault (DAV). Innsbruck-Salzburg-Amstetten fault (ISAM); Salzach-Ennstal-Mariazell-Puchberger fault (SEMP); Mur-Mürztal fault (MM); Lavanttal fault (LA); Mölltal fault (MÖ); Iseltal fault (IS).

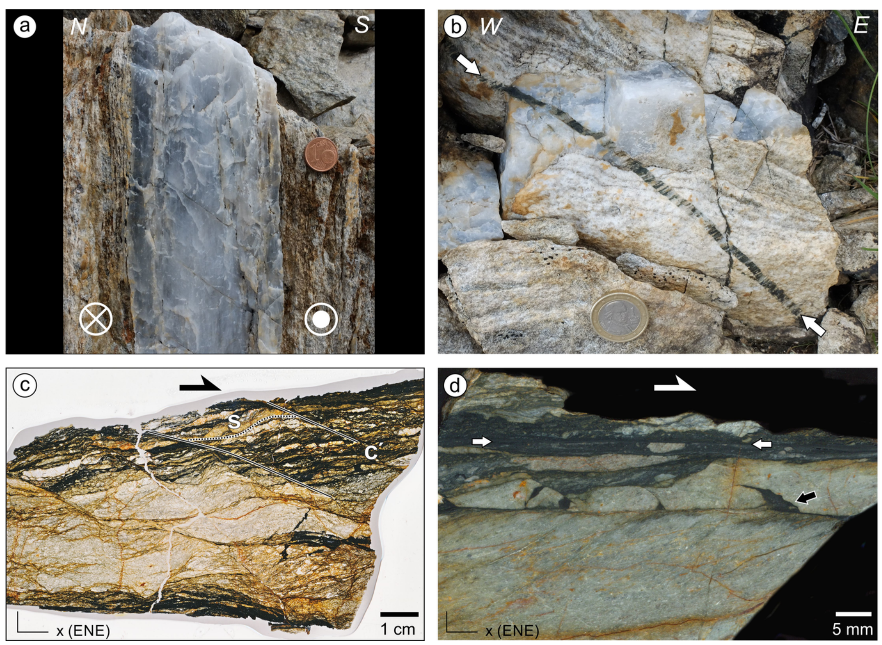

Figure 2. Field and sample pictures of the quartz mylonites and the brittle/ductile fault rocks. (a) Vertical, 7.5 cm-thick, mylonitic quartz vein within the foliated paragneisses (looking in the stretching lineation direction). Note the absence of cataclastic deformation. The white circle with the dot and with the cross indicate movement towards and from the observer, respectively, accommodated by the quartz mylonite (UTM33 326551.291 E / 5198985.993 N). (b) Fibrous quartz/chlorite vein (white arrows) cross-cutting the paragneiss and a mylonitized quartz vein oblique to the host rock foliation (UTM33 326540.807 E / 5198973.953 N) (see also Figure S6c). (c) Scan of a large thin section of foliated cataclasites and pseudotachylytes, ductilely overprinted by dextral SC' fabric (UTM33 326551.291 E / 5198985.993 N). (d) Polyphase ultracataclasites/pseudotachylytes partly overprinted by ductile deformation. Black arrow shows pseudotachylyte injection vein. Two small white arrows highlights a principal slip surface with a

truncated grain, separating different generations of ultracataclasites/pseudotachylytes (UTM33 326542.099 E / 5198981.700 N).

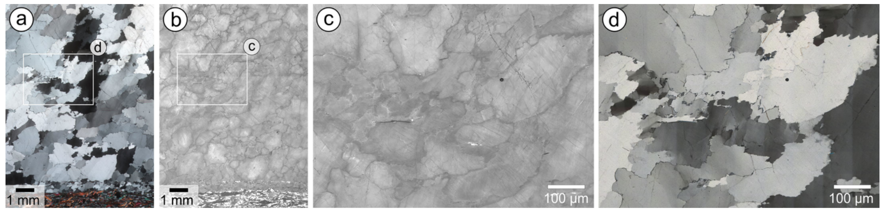

Figure 3. Weakly deformed quartz vein (sample HS-1B-2; UTM33 326621.460 E / 5199004.084 N) showing coarse grains with lobate grain boundaries typical of grain boundary migration recrystallization referable to the amphibolite facies formation conditions. (a, d) Optical microphotographs under crossed-polarized light (XPL). (b, c) SEM-CL images of same area as (a) and (d).

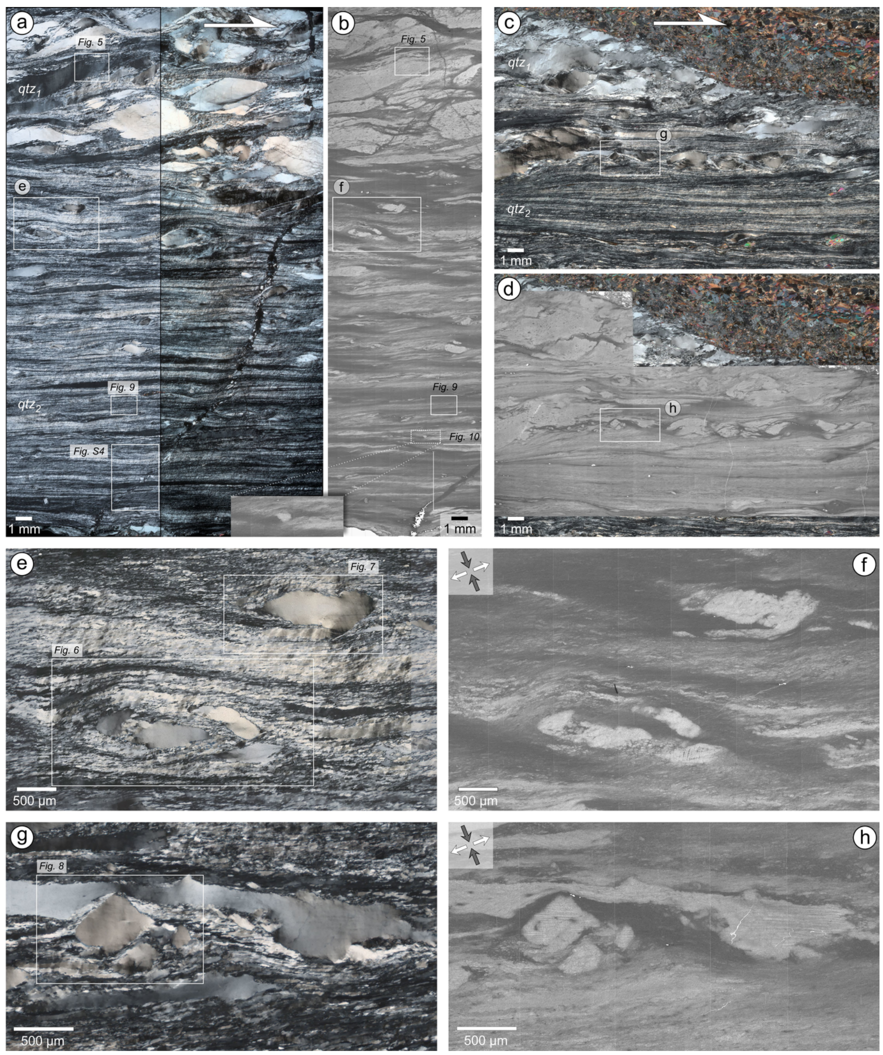

Figure 4. Microstructures (optical microphotograph, XPL, and corresponding CL images) of 2 deformed

quartz veins (a, b, e, f: sample MS-H2-2; c, d, g, h: sample MS-09a - UTM 33 326551.139 E / 5198985.997). Both samples show a strain gradient from a protomylonitic fabric (upper part) to mylonitic/ultramylonitic (lower part). The latter reveals a characteristic extinction banding in the optical images (a, c). MS-H2-2 shows a corresponding banding in the CL image (b). The (ultra)mylonitic part of MS-09a reveals similar CL intensity as the coarse qtz_1 clasts with only subtle variations (d). (e-h) Microstructures of quartz clasts in (ultra)mylonitic qtz_2 matrix. Note in (f), the CL intensity variation around the lower left clast-aggregate corresponding to stress-field – four-quadrant pattern. Similar 4-quadrand CL feature is highlighted in (b) – see insert. For both samples the schematic (not quantified) orientation of the instantaneous stretching axis is given in (f, h) – see insert. The sense of shear is dextral in all the figures.

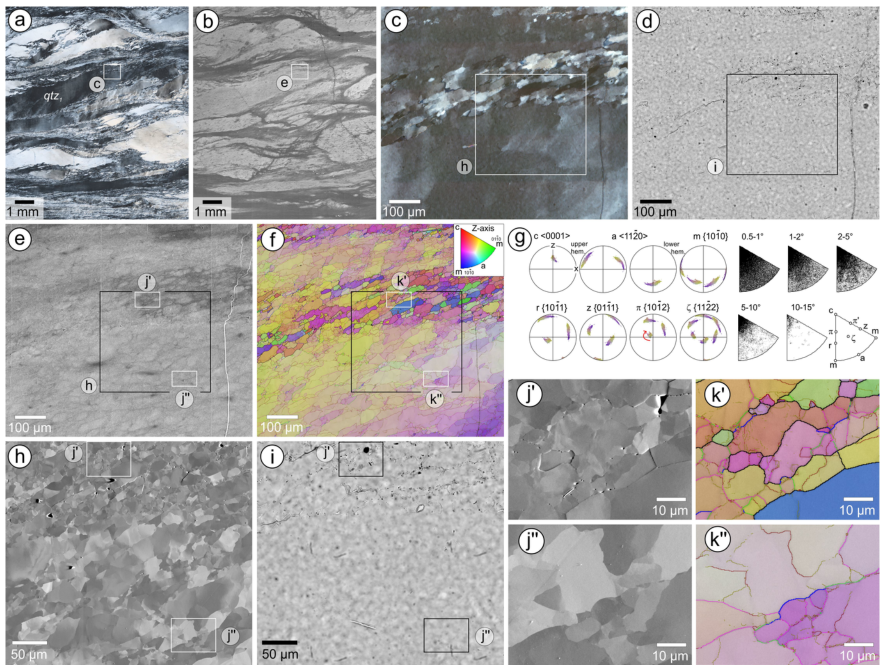

Figure 5. Internal deformation microstructure of elongated quartz grain (qtz_1). (a, b) Protomylonitic part of sample MS-H2-2 (XPL, SEM-CL). (c-f) Enlarged microstructure as marked in (a) and (b) – same location site (c: optical microphotograph, XPL; d: optical microphotograph under plane-polarized light, PPL; e: SEM-CL; f: EBSD orientation map (step size: 200 nm) colour coded with respect to Z-axis of the PF – see insert). For boundaries levels see key below. Note that high fluid inclusion (FI) spatial density in (d) matches with dark CL patterns in (e). In (e) fine dark-grey CL lines corresponds to low angle boundaries (LAB) in (f). (g) Pole figures (PF, equal area, lower hemisphere projection) and inverse PF with respect to crystal references system (equal area, upper hemisphere projection) of substructured host crystal (lower part). (h) Orientation (channelling) contrast (OC) image of area as marked in C, E, F. (I) Optical microphotograph (PPL) of same area in (h). (j, k) Detailed OC images and EBSD maps of areas as marked in e, f, h, i. Note in (j'), the porosity corresponds to FI in (I) and mainly follows high angle boundaries (HAB) of smaller grains in (k'). In contrast (j") and (k") does not show evidence of porosity/FI. EBSD boundary levels (misorientation angle interval): low angle boundaries: olive green 0.5-1°, maroon 1-2°, fuchsia 2-5°, green 5-10°; high angle boundaries: blues 10-15°, black >15°; Dauphine twin: red 60°±5° around $<c>$ axis.

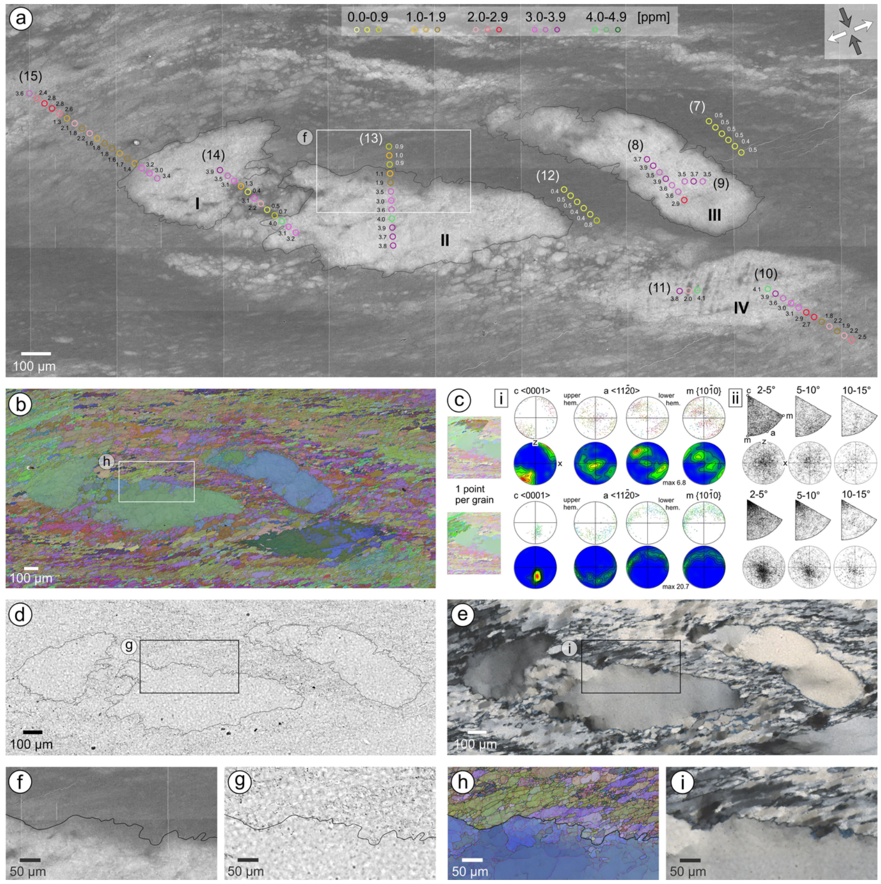

Figure 6. Cluster of *qtz₁* porphyroclasts (I-IV) within (ultra)mylonitic matrix as marked in Figure 4a, b, e, f. (a) SEM-CL image with Ti-in-qtz data. SIMS analysis spots (c. 15 µm) are colour-coded with respect to Ti concentration [Ti] – key is given. (b) EBSD map (step size: 500 nm) colour coded with respect to Euler angles. Internal substructure is highlighted by superposition of the partially transparent Euler map on the band contrast map. HAB are shown - for key see below. (c) Variation of the CPO of (ultra)mylonitic flow fabric around clast. Orientation data of 2 specific areas are plotted as (i) pole figures and (ii) misorientation axis plots of LAB (IPF, crystallographic reference system; PF, sample reference system). (d, e) Optical microphotographs (PL, XPL) of same areas as presented in (b). Note, spatial FI density correlates with CL variation in (a). (f-i) Porphyroclast II: magnification of the porphyroclast margin outlined in a-e. Black lines indicate grain boundary (GB) of quartz clast. In (f) decreasing CL intensity in clast towards GB corresponds to higher substructure density shown in (h), whereas the FI density is relatively low (g). (h) Clast in EBSD orientation map is colour coded with respect of texture component in blue, surrounding recrystallization matrix to Euler angles. Boundary level coding follows Figure 5. Density maxima of PF are given as multiple of random distribution (*mrd*).

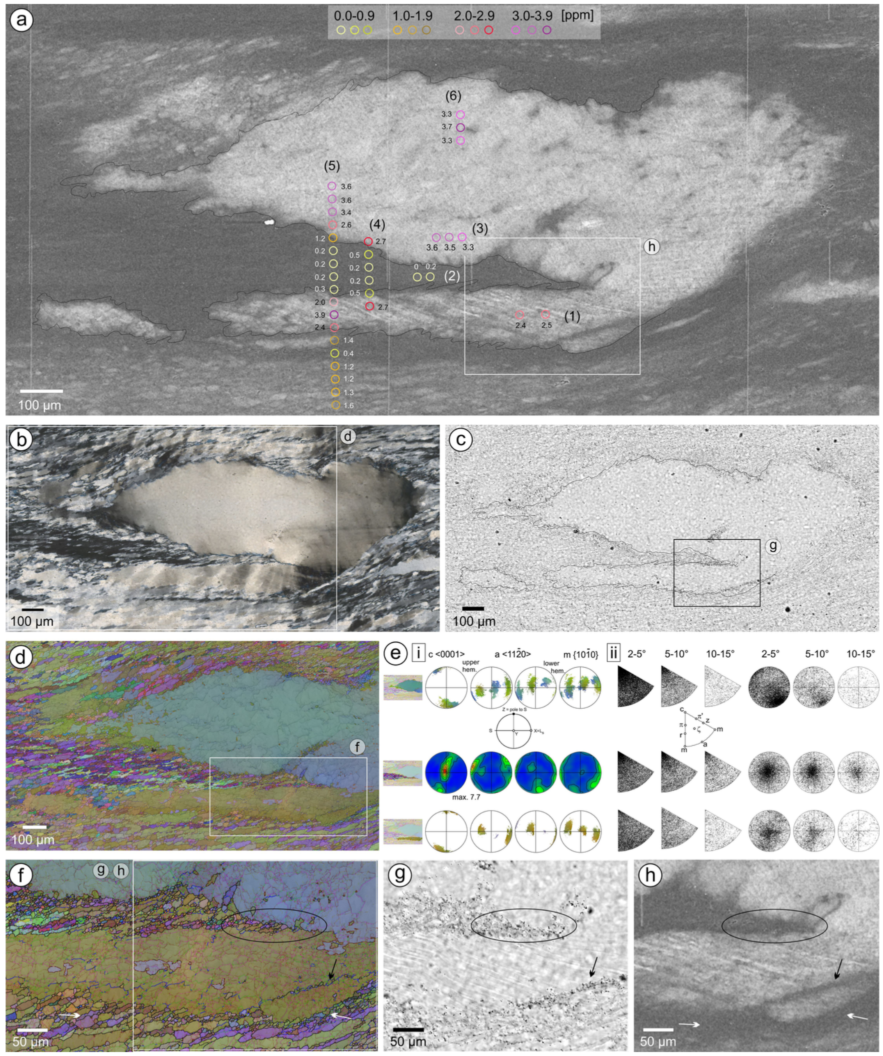

Figure 7. Quartz clast within (ultra)mylonitic matrix as marked in Figure 4a, b, e, f. (a) SEM-CL image with Ti-in-qtz data. SIMS analysis spots (c. 15 µm) are colour with respect to [Ti] – key is given. (b, c) Optical microphotographs (XPL, PL). Note, FI density in (c) corresponds with CL variation in (a). Black line in (a-c) indicates GB of quartz clast. (d) EBSD map (step size: 500 nm): transparent superposition of Euler and band contrast map; HAB are shown - see Figure 6. (e) Orientation data of clast domains are presented as (i) PF and (ii) misorientation axis plots of LAB (IPF and PF). (f) Enlarged EBSD area as marked in (d). LAB and HAB are given – for key see Figure 5. (g) Optical microphotograph (PPL) of area as marked in (f). (h) SEM-CL image of same area as presented in (g). CL variation corresponds to FI density shown in (g). In (f-h) black arrows mark intracrystalline deformation zone traced by HAB, white arrows recrystallization zone below the clast and ellipse the tip of recrystallized aggregates between upper and lower clast domain. Oblique features in (g, h) are deformation lamellae.

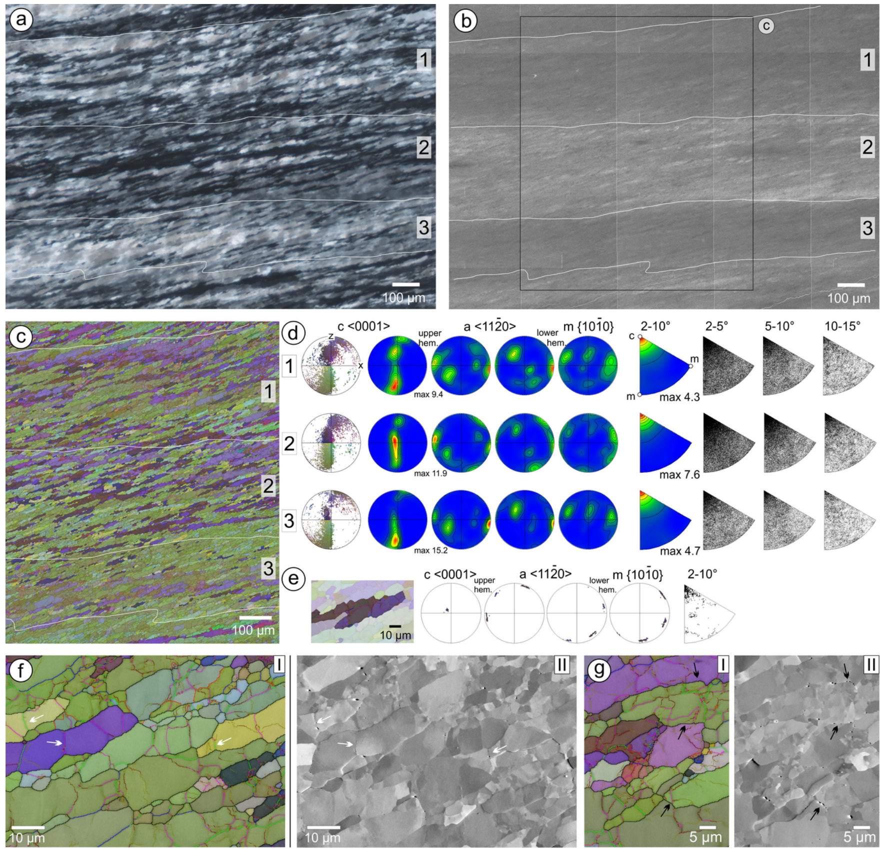

Figure 8. (Ultra)mylonite microstructure (sample HS-H2-2). (a) Optical microstructure (XPL). (b) SEM-CL image of same area as (a). (c) EBSD map (step size 200 nm) of area as marked in (b) colour-coded with respect to Euler angles. White lines in (a-c) marks CL banding. Note in (a, c), elongated grains (aspect ratio up 10:1) are highly substructured and show an oblique shape preferred orientation (SPO). (d) Orientation data of different CL-bands (1-3) are presented as PF (CPO) and misorientation axis of LAB (2-15°) as IPF. Note, the main cluster around $<c>$ indicating prism$<a>$ slip. Density maxima (mrd) are given. (e) Elongated substructured grain shows a dispersion path around $<c>$ and a clustering of LAB misorientation axis in IPF also around $<c>$. (f, g) Exemplary microstructure of elongated and highly substructured quartz grains. EBSD maps (I figures) and corresponding OC images (II figures). Subgrain size is in the same order as the new small grains, 1-10 µm. White arrows in (f) indicate LAB; black arrows indicate HAB in (g), decorated with porosity (fluid inclusions). Boundary levels in EBSD maps follows key of Figure 5.

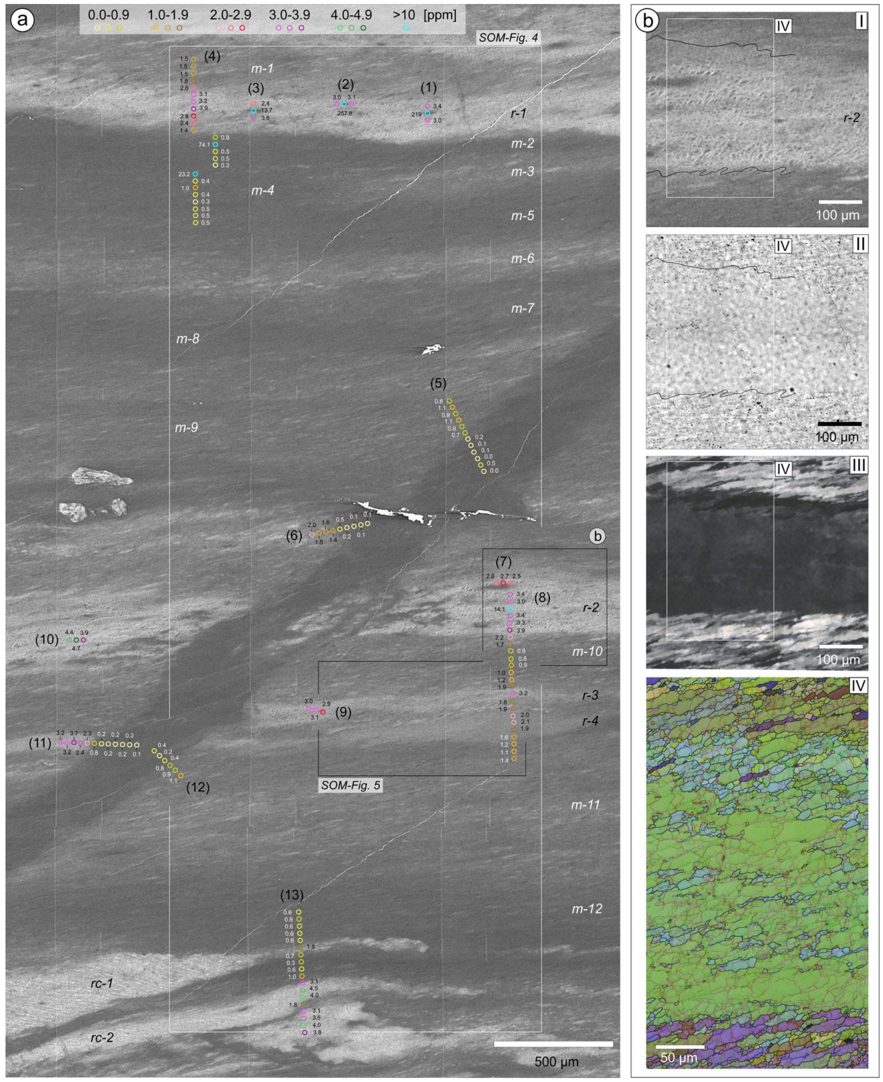

Figure 9. (a) SEM-CL image of (ultra)mylonite microstructure including (ultra)mylonitic layers (*m*), ribbon grains (*r*), ribbon-clasts (*rc*) and crosscutting late stage quartz vein. SIMS analysis spots are colour-coded with respect to [Ti] – key is given. Spots with [Ti] >10 ppm are related to micron-scale mica inclusions. (b) (I-III) Enlargement of an area of*ribbon-2* (r-2) as marked in (a). Black lines in (I, II) represent upper and lower grain boundaries of *ribbon-2* . (I) SEM-CL image. (II, III) Optical microphotograph (PPL, XPL). In (II) *ribbon-2*shows low spatial density of FI compared to high FI density in adjacent (ultra)mylonitic layers corresponding to CL intensity variation in (a). (IV) EBSD map (step size: 500 nm) of area as marked in (I-III) colour coded with respect to Euler angles. Boundary levels follow those of Figure 5. Note high spatial density of subgrain boundary in quartz ribbon.

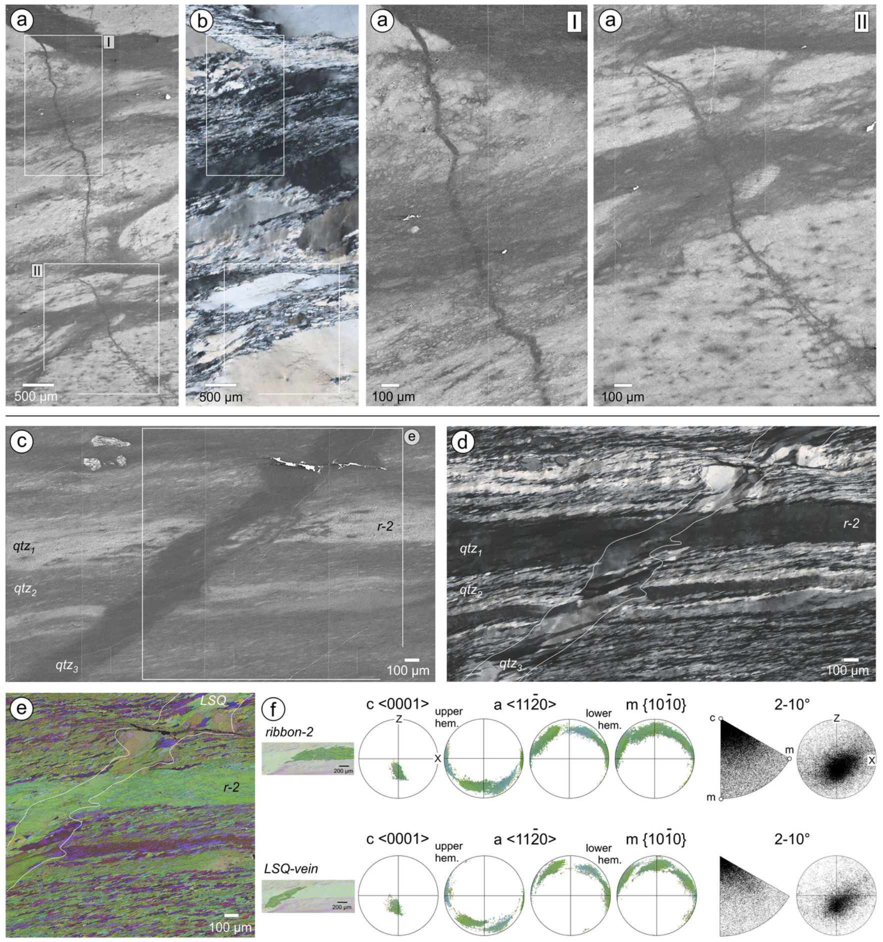

Figure 10. Late stage quartz (LSQ) vein (*qtz₃*) crosscutting the protomylonitic (a, b) and (ultra)mylonitic (c, d) microstructure. Optical microphotographs (XPL; b, d) and corresponding SEM-CL images (a, c). LSQ veins crosscutting the (ultra)mylonite is synkinematically deformed. (e) EBSD map (step size: 500 nm) of area as marked in (c). White line in (d) and (e) marks boundary of LSD-vein. (f) Orientation data of *ribbon-2* and LSQ vein are plotted as PF and misorientation axis of LAB as IPF and PF.

Table 1 . Results of chlorite thermometry showing the number of analyses, the calculated temperature range, average and standard deviation for each microstructural site of Figure S6.

Microstructural site	n	T min [°C]	T max [°C]	avg T [°C]	std T [°C]
A: Chl in strain shadow or sheard band	13	238	268	255	11
B: Chl in garnet cracks, retrogression product of garnet	31	272	352	315	24
C: Chl in LSQ-vein	38	265	333	300	19

References

Acosta, M. D., Watkins, J. M., Reed, M. H., Donovan, J. J., & De Palolo, D. J. (2020). Ti-in-quartz: Evaluating the role of kinetics in high temperature crystal growth experiments. *Geochimica et Cosmochimica Acta,*

281, 149-167. https://doi.org/10.1016/j.gca.2020.04.030.

Ashley, K. T., Carlson, W. D., Law, R. D., & Tracy, R. J. (2014). Ti resetting in quartz during dynamic recrystallization: mechanisms and significance. *American Mineralogist* , 99, 2025–2030. http://dx.doi.org/10.2138/am-2014-4943.

Ashley, K. T., Webb, L. E., Spear, F. S., & Thomas, J. B. (2013). P-T-D histories from quartz: A case study for the application of the TitaniQ thermobarometer to progressive fabric development in metapelites.*Geochemistry, Geophysics, Geosys* (G3) 14, 3821–3843. https://doi.org/10.1002/ggge.20237.

Behr, W. M., & Platt, J. P. (2011). A naturally constrained stress profile through the middle crust in an extensional terrane. *Earth and Planetary Science Letters,* 303, 181–192. http://dx.doi.org/10.1016/j.epsl.2010.11.044.

Bestmann, M., & Pennacchioni, G. (2015). Ti distribution in quartz across a heterogeneous shear zone within a granodiorite: the effect of deformation mechanism and strain on Ti resetting. *Lithos,* 227, 37–56. https://doi.org/10.1016/j.lithos.2015.03.009.

Bestmann, M., Piazolo, S., Spiers, C. J., & Prior, D.J. (2005). Microstructural evolution during initial stages of static recovery and recrystallization: new insights from in-situ heating experiments combined with electron backscatter diffraction analysis. *Journal of Structural Geology,* 27, 447–457. http://dx.doi.org/10.1016/j.jsg.2004.10.006.

Bourdelle, F. (2021). Low-Temperature Chlorite Geothermometry and Related Recent Analytical Advances: A Review. Minerals, 11(2), 130.

Bromiley, G. D., & Hiscock, M. (2016). Grain boundary diffusion of titanium in polycrystalline quartz and its implications for titanium in quartz (TitaniQ) geothermobarometry. *Geochimica et Cosmochimica Acta,*

178, 281–290. https://doi.org/10.1016/j.gca.2016.01.024.

Calzolari, G., Rossetti, F., Ault, A. K., Lucci, F., Olivetti, V., & Nozaem, R. (2018). Hematite (U-Th)/He thermochronometry constrains intraplate strike-slip faulting on the Kuh-e-Faghan Fault, central Iran. Tectonophysics, 728, 41-54.

Campbell, L. R., Menegon, L., Fagereng, A., & Pennacchioni, G. (2020). Earthquake nucleation in the lower crust by local stress amplification.*Nature Communication,* 11. https://doi.org/10.1038/s41467-020-15150-x.

Cantarero, I., Lanari, P., Vidal, O., Alías, G., Travé, A., & Baqués, V. (2014). Long-term fluid circulation in extensional faults in the central Catalan Coastal Ranges: P–T constraints from neoformed chlorite and K-white mica. Internation Journal of Earth Sciences (Geologische Rundschau), 103(1), 165-188.

Ceccato, A., Goncalves, P., & Pennacchioni, G. (2020). Temperature, fluid content and rheology of localized ductile shear zones in sub–solidus cooling plutons. *Journal of metamorphic Geology* , 38, 881-903. https://doi.org/10.1111/jmg.12553.

Ceccato, A., & Pennacchioni, G. (2018). Structural evolution of the Rieserferner pluton in the framework of the Oligo-Miocene tectonics of the eastern Alps. *Journal of Structural Geology* , 116, 64-80. https://doi.org/10.1016/j.jsg.2018.08.004.

Ceccato, A., Pennacchioni, G., Menegon, L., & Bestmann, M. (2017). Crystallographic control and texture inheritance during mylonitization of coarse grained quartz veins. *Lithos,* 290–291, 210–227. https://doi.org/10.1016/j.lithos.2017.08.005.

Chakraborty, S., 2008. Diffusion in solid silicates. *Annual Review of Earth and Planetary Sciences,* 36, 153-190.

Cherniak, D. J., Watson, E. B. & Wark, D. A. (2007). Ti diffusion in quartz. *Chemical Geology*

236(1–2), 65-74. https://doi.org/10.1016/j.chemgeo.2006.09.001.

Drury, M. R., Humphreys, F. J., & White, S. H. (1985). Large strain deformation studies using polycrystalline magnesium as a rock analogue. Part II: dynamic recrystallization mechanisms at high temperatures.*Physics of the Earth and Planetary Interiors,* 40, 208–222. https://doi.org/10.1016/0031-9201(85)90131-1.

Farver, J. R., & Yund, R.A. (1991). Oxygen diffusion in quartz: Dependence on temperature and water fugacity. *Chemical Geology* , 90 (1-2), 55–70.

Fitz Gerald, J. D., Mancktelow, N. S., Pennaccioni, G., & Kunze, K. (2006). Ultrafine-grained quartz mylonites from high-grade shear zones: Evidence for strong dry middle to lower crust. *Geology,* 34, 369-372.

Ganne, J., De Andrade, V., Weinberg, R. F., Vidal, O., Dubacq, B., Kagambega, N., & Allibon, J. (2012). Modern-style plate subduction preserved in the Palaeoproterozoic West African craton. Nature Geoscience, 5(1), 60-65.

Grujic, D., Stipp, M., & Wooden, J. (2011). Thermometry of quartz mylonites: importance of dynamic recrystallization on Ti-in-quartz re-equilibration. *Geochemistry, Geophysics, Geosystem,* 12, Q06012. http://dx.doi.org/10.1029/2010GC003368.

Haertel, M., Herwegh, M., & Pettke, T. (2013). Titanium-in-quartz thermometry on synkinematic quartz veins in a retrograde crustal-scale normal fault zone. *Tectonophysics,* 608, 468–481. http://dx.doi.org/10.1016/j.tecto.2013.08.042.

Hamers, M. F., Pennock, F. M., & Drury, M. R. (2017). Scanning electron microscope cathodoluminescence imaging of subgrain boundaries, twins and planar deformation features in quartz. *Physics and Chemistry of Minerals,* 44, 263-275.

Hawemann, F., Mancktelow, N. S., Pennacchioni, G., Wex, S., & Camacho, A. (2019). Weak and slow, strong and fast: How shear zones evolve in a dry continental crust (Musgrave Ranges, Central Australia).*Journal of Geophysical Research: Solid Earth* , 124, 1671-1687, https://doi.org/10.1029/2018JB016559.

Hauke, M., Froitzheim, N., Nagel, T.J., Miladinova, I., Fassmer, K., Fonseca, R. O. C., Sprung, P., & Münker, C. (2019). Two high-pressure metamorphic events, Variscan and Alpine, dated by Lu–Hf in an eclogite complex of the Austroalpine nappes (Schobergruppe, Austria).*International Journal of Earth Sciences (Geologische Rundschau),*108, 1317-1331. https://doi.org/10.1007/s00531-019-01708-8.

Hirth, G., & Beeler, N. M. (2015). The role of fluid pressure on frictional behavior at the base of the

seismogenic zone. *Geology,* 43, 223-226. doi:10.1130/G36361.1

Howard, D. L., de Jonge, M. D., Afshar, N., Ryan, C. G., Kirkham, R., Reinhardt, J., Kewish, C. M., McKinlay, J., Walsh, A., Divitcos, J., Basten, N., Adamson, L., Fiala, T., Sammut, L., & Paterson, D.J. (2020). The XFM beamline at the Australian Synchrotron. *Journal of Synchrotron Radiation,* 27, 1447-1458. https://doi.org/10.1107/S1600577520010152

Huang, R., & Audetat, A. (2012). The titanium-in-quartz (TitaniQ) thermobarometer: a critical examination and re-calibration.*Geochimica et Cosmochimica Acta,* 84, 75–89.

Kidder, S., Avouac, J.-P., & Chand, Y.-C. (2013). Application of titanium-in-quartz thermobarometry to greenschistfacies veins and recrystallized quartzites in the Hsuehshan range, Taiwan. *Journal of Geophysical Research: Solid Earth,* 4, 1–21.

Kidder, S., Toy, V., Prior, D., Little, T., & Macrae, C. (2018). Constraints on alpine fault (New Zealand) mylonitization temperatures and geothermal gradient from Ti-in-quartz thermobarometry. *Journal of Geophysical Research: Solid Earth,* 9, 1123-1139.

Kirschner, D., & Teyssier, C. (1991). Quartz c-axis fabric differences between porphyroclasts and recrystallized grains. *Journal of Structural Geology* , 13, 105-109. https://doi.org/10.1016/0191-8141(91)90106-S

Kohn, M. J., & Northrup, C. J. (2009). Taking mylonites' temperatures.*Geology,* 37, 47–50.

Korchinski, M., Little, T. A., Smith, E., & Millet, M.-A. (2012). Variation of Ti-in-quartz in gneiss domes exposing the world's youngest ultrahigh-pressure rocks, D'Entrecasteaux Islands, Papua New Guinea.*Geochemistry, Geophysics, Geosystem,* 13, Q0AL01. http://dx.doi.org/10.1029/2012GC004230.

Krenn, E., Schulz, B., & Finger, F. (2012). Three generations of monazite in Austroalpine basement rocks to the south of the Tauern Window: evidence for Variscan, Permian and Eo-Alpine metamorphic events.*Swiss Journal of Geoscience,* 105(3), 343-360.

Lacroix, B., Charpentier, D., Buatier, M., Vennemann, T., Labaume, P., Adatte, T., & Dubois, M. (2012). Formation of chlorite during thrust fault reactivation. Record of fluid origin and P–T conditions in the Monte Perdido thrust fault (southern Pyrenees). Contributions to Mineralogy and Petrology, 163(6), 1083-1102.

Legros, M., Dehm, G., Arzt, E., & Balk, T. J. (2008). Observation of giant diffusivity along dislocation cores. *Science,* 319, 1646–1649. http://dx.doi.org/10.1126/science.1151771.

Linner, M. (1999). Die P-T-t Entwicklung der Eklogite im Schoberkristallin als Beleg fur fruhalpidische kontinentale Subduktion im Ostalpinen Kristallin. *Thesis, University of Vienna* , 211 p.

Linner, M., Habler, G., & Grasemann, B. (2009). Switch of kinematics in the austroalpine basement between the defereggen-antholz-Vals (DAV) and the Pustertal-Gailtal fault. In: *9th Workshop on Alpine Geological Studies Cogne/Italy* , 16, pp. 18.

Mancktelow, N. S., Stockli, D. F., Grollimund, B., Muller, W., Fugenschuh, B., Viola, G., Seward, D., & Villa, I. M. (2001). The DAV and Periadriatic fault systems in the Eastern Alps south of the Tauern window. *Internation Journal of Earth Sciences (Geologische Rundschau),* 90 (3), 593-622.

Mizera, M., Little, T., Boulton, C., Prior, D., Watson, E., Biemiller, J., & Shigematsu, N. (2020). Slow-to-fast deformation in mafic fault rocks on an active low-angle normal fault, Woodlark Rift, SE Papua New Guinea. Geochemistry, Geophysics, Geosystem, 21(11), e2020GC009171.

Nachlas, W. O., & Hirth, G. (2015). Experimental constraints on the role of dynamic recrystallization on resetting the Ti-in-quartz thermobarometer. *Journal of Geophysical Research: Solid Earth,*120, 8120–8137. https://doi.org/10.1002/2015JB012274.

Nachlas, W. O., Whitney, D. L., Teyssier, C., Bagley, B., & Mulch, A. (2014). Titanium concentration in quartz as a record of multiple deformation mechanisms in an extensional shear zone. *Geochemistry, Geophysics, Geosystem,* 15, 1374–1397. http://dx.doi.org/10.1002/2013GC005200.

Nachlas, W. O., Thomas, J. B., & Hirth, G. (2018). TitaniQ deformed: Experimental deformation of out-of-equilibrium quartz porphyroclasts.*Journal of Structural Geology,* 116, 207-222.

Negrini, M., Stunitz, H., Berger, A., & Morales, L. F. G. (2014). The effect of deformation on the TitaniQ geothermobarometer: an experimental study. *Contributions to Mineralogy and Petrology,* 167, 982. http://dx.doi.org/10.1007/s00410-014-0982-x.

Neumann, B. (2000). Texture development of recrystallized quartz polycrystals unravelled by orientation and misorientation characteristics. *Journal of Structural Geology,* 22, 1695–1711.

Pennacchioni, G., & Mancktelow, N. S. (2018). Small-scale ductile shear zones: Neither extending, nor thickening, nor narrowing.*Earth-Science Reviews* , 184, 1-12. https://doi.org/10.1016/j.earscirev.2018.06.004.

Pennacchioni, G., Menegon, L., Leiss, B., Nestola, F., & Bromiley, G. (2010). Development of crystallographic preferred orientation and microstructure during plastic deformation of natural coarse-grained quartz veins. *Journal of Geophysical Research: Solid Earth,* 115, B12405. http://dx.doi.org/10.1029/2010JB007674.

Pennacchioni, G., & Zucchi, E. (2013). High-temperature fracturing and ductile deformation during cooling of a pluton: the Lake Edison granodiorite (Sierra Nevada batholith, California). *Journal of Structural Geology* , 50, 54-81. https://doi.org/10.1016/j.jsg.2012.06.001.

Piazolo, S., La Fontaine, A., Trimby, P., Harley, S., Yang, L., Armstrong, R. & Cairney J. M. (2016). Deformation-induced trace element redistribution in zircon revealed using atom probe tomography.

Nature Communication,

7, 10490. https://doi.org/10.1038/ncomms10490.

Plunder, A., Agard, P., Dubacq, B., Chopin, C., & Bellanger, M. (2012). How continuous and precise is the record of P–T paths? Insights from combined thermobarometry and thermodynamic modelling into subduction dynamics (Schistes Lustres, W. Alps). Journal of Metamorphic Geology, 30(3), 323-346.

Powell, R., & Holland, T. J. B. (2008). On thermobarometry. Journal of Metamorphic Geology, 26(2), 155-179.

Ratschbacher, L., Frisch, W., Neubauer, F., Schmid, S. M., & Neugebauer, J. (1989). Extension in compressional orogenic belts: the Eastern Alps. *Geology,* 17, 404–407. https://doi.org/10.1130/0091-7613(1989)017%3C0404:EICOBT%3E2.3.CO;2.

Rosenberg, C. L., Brun, J. P., Cagnard, F., & Gapais, D. (2007). Oblique indentation in the Eastern Alps: insights from laboratory experiments. *Tectonics* , 26(2). https://doi.org/10. 1029/2006TC001960.

Schulz, B. (1993). Mineral chemistry, geothermobarometry and pre-Alpine high-pressure metamorphism of eclogitic amphibolites and mica schists from the Schobergruppe, Austroalpine basement, Eastern Alps.*Mineralogical Magazine,* 57(387), 189-202.

Schuster, R., Daurer, A., Krenmayr, H.-G., Linner, M., Mandl, G. W., Pestal, G., & Reitner, J. M. (2014). Rocky Austria: The Geology of Austria - brief and colourful. *Vienna, Geological Survey Austria* , p. 1-80.

Spear, F. S., & Wark, D. (2009). Cathodoluminescence imaging and titanium thermometry in metamorphic quartz. *Journal of Metamorphic* Geology, 27, 187–205.

Stipp, M., Stunitz, H., Heilbronner, R., & Schmid, S. M. (2002). The Eastern Tonale fault zone: a "natural laboratory" for crystal plastic deformation of quartz over a temperature range from 250 to 700 degC.*Journal of Structural Geology,* 24, 1861–1884.

Thomas, J. B., & Watson, E. B. (2014). Diffusion and partitioning of magnesium in quartz grain boundaries. *Contributions to Mineralogy and Petrology,* 168, 1–12. https://doi.org/10.1007/s00410-014-1068-5.

Thomas, J. B., Watson, E. B., Spear, F. S., Shemella, P. T., Nayak, S. K., & Lanzirozzi, A. (2010). TitaniQ under pressure: the effect of pressure and temperature on the solubility of Ti in quartz.*Contributions to Mineralogy and Petrology,* 160, 743–759.

Thoni, M. (2006). Dating eclogite-facies metamorphism in the Eastern Alps – approaches, results, interpretations: a review. *Mineralogy and Petrology,* 88(1-2). https://doi.org/10.1007/s00710-00006-00153-00715.

Urai, J. L., Means, W. D., & Lister, G. S. (1986). In: Hobbs, B. E., Heard, H. C. (Eds.), Dynamic Recrystallization of Minerals. Mineral and Rock Deformation: the Paterson Volume. *American Geophysical Union* , Washington, D.C., pp. 1–49.

Vidal, O., Parra, T., & Vieillard, P. (2005). Thermodynamic properties of the Tschermak solid solution in Fe-chlorite: Application to natural examples and possible role of oxidation. American Mineralogist, 90(2-3), 347-358.

Vidal, O., de Andrade, V., Lewin, E., Munoz, M., Parra, T., & Pascarelli, S. (2006). P–T-deformation-Fe3+/Fe2+ mapping at the thin section scale and comparison with XANES mapping: application to a garnet-bearing metapelite from the Sambagawa metamorphic belt (Japan). Journal of Metamorphic Geology, 24(7), 669-683.

Wark, D. A., & Spear, F. S. (2005). Titanium in quartz: Cathodoluminescence and thermometry. *Geochimica et Cosmochimica Acta* , Suppl. 69, A592.

Wark, D. A., & Watson, E. B. (2006). TitaniQ: a titanium-in-quartz geothermometer. *Contributions to Mineralogy and Petrology,* 152, 743–754.

Yund, R. A., Smith, B. M., & Tullis, J. (1981). Dislocation-assisted diffusion of oxygen in albite. *Physics and Chemistry of Minerals,*7, 185–189.

Yund, R. A., & Tullis, J. (1991). Compositional changes of minerals associated with dynamic recrystallization. *Contributions to Mineralogy and Petrology,* 108, 346–355. https://doi.org/10.1007/BF00285942.

Zihlmann, B., Muller, S., Coggon, R. M., Koepke, J., Garbe-Schonberg, D., & Teagle, D. A. (2018). Hydrothermal fault zones in the lower oceanic crust: An example from Wadi Gideah, Samail ophiolite, Oman. Lithos, 323, 103-124.

Influence of deformation and fluids on the Ti exchange in quartz

Michel Bestmann[1], Giorgio Pennacchioni[2], Bernhard Grasemann[3], Benjamin Huet[4], Michael W. M. Jones [5], Cameron M. Kewish[6,7]

[1]GeoZentrum Nordbayern, Friedrich-Alexander Universität Erlangen-Nürnberg, 91054 Erlangen, Germany

[2]Department of Geosciences, University of Padova, 35131 Padova, Italy

[3]Department of Geology, University of Vienna, A-1090 Vienna, Austria

[4]Department of Hard Rock Geology, Geological Survey of Austria, A-1030 Vienna, Austria

[5]Central Analytical Research Facility, Queensland University of Technology, Brisbane, 4000, QLD, Australia

[6]Australian Synchrotron, ANSTO, Clayton, 3186, Vic, Australia

[7]Department of Chemistry and Physics, School of Molecular Sciences, La Trobe University, Melbourne, VIC 3086

Corresponding author: Michel Bestmann (`michel.bestmann@fau.de`)

Key Points

- Ti-in-quartz re-equilibration is possible in the regime of subgrain rotation recrystallization even at lower greenschist facies condition
- Ti resetting depends on the availability of fluid independently of strain and is mainly related to wetted interconnected grain boundaries
- Partial Ti resetting also take place along dry subgrain boundaries

Abstract

Coarse-grained quartz veins from the Prijakt Nappe (Austroalpine Unit, Schober Mountains, Eastern Alps), that formed under amphibolite facies conditions, were overprinted by lower greenschist facies deformation. During overprinting, subgrain rotation (SGR) recrystallization was the dominant mechanism assisting the evolution from protomylonite to (ultra)mylonite. The initial Ti-concentration [Ti] (3.0-4.7 ppm) and corresponding cathodoluminescence (CL) signature of the quartz vein crystals were reset to different degrees mainly depending on the availability of fluids and their partitioning across the microstructure. The amount of strain played a subordinate role in resetting. In recrystallized aggregates the most complete re-equilibration ([Ti] of 0.2-0.6 pm) occurred in strain shadows surrounding quartz porphyroclasts, acting as fluid sinks, and in localized shear bands that channelized fluid percolation. We applied a correlative multi-analytical workflow using optical and electron microscopy methods (e.g. electron backscatter diffraction and cathodoluminescence) in combination with secondary ion mass spectroscopy for [Ti] measurement. The most efficient

[Ti] resetting mainly occurs along wetted high angle boundaries (misorientation angle >10-15°), and to a minor extend (partial resetting) along dry low angle boundaries (<10-15°). This key-study prove for the first time that pure subgrain rotation recrystallization in combination with dissolution-precipitation under retrograde condition is able to provide microstructural sites to apply the TitaniQ geothermobarometer at deformation temperatures down to 300-350 °C provided that information on pressure and Ti-activity is available.

Plain Language Summary

Since around 10 years, the so-called TitaniQ geothermometer is used to constrain deformation temperatures in quartz-rich rocks. The calibration roots on the direct correlation of the titanium trace element concentration in quartz with respect to the ambient temperature. However, the processes and parameters, which lead to re-equilibration of the Ti-in-quartz system during deformation, are not fully understood yet. Here we analysed deformed quartz veins from the Eastern Alps applying a correlative data workflow. In contrast to recent studies, we were able to show that instead of strain the availability of fluids and it's partitioning, especially along grain boundaries plays an essential role. We also provide a robust interpretation tool for the interplay between grain-scale deformation, fluid-rock interaction and geochemical exchange during increasing strain in the quartz mylonites. Finally, we were able to identify specific microstructures representing most re-equilibrated sites in order to apply the TitaniQ geothermometer even at lower greenschist facies deformation conditions (independently constrained by chlorite thermometry) dominated by subgrain rotation recrystallization.

Keywords

Quartz

TitaniQ thermobarometry

Recrystallization processes

Correlative data workflow

Geochemical re-equilibration

Cathodoluminescence

1. **Introduction**

Under static condition, Ti incorporation in quartz lattice during crystal growth is a function of temperature, pressure and Ti activity. Ti concentrations (referred to as [Ti] hereafter) in quartz can, therefore, be used as a geothermometer (TitaniQ: Huang & Audétat, 2012; Thomas et al., 2010; Wark & Watson, 2006) to estimate ambient conditions of quartz formation. TitaniQ is well suited for quartz in magmatic and high-grade metamorphic rocks, and when quartz directly precipitated from a fluid.

[Ti] in quartz can be modified during crystal-plastic deformation. This gives TitaniQ the potential of estimating the ambient conditions of deformation. Since the original proposal by Kohn & Northrup (2009), several authors have attempted to apply TitaniQ to mylonites and to understand the behaviour of Ti in quartz during deformation in either nature (Behr & Platt, 2011; Bestmann & Pennacchioni, 2015; Grujic et al., 2011; Haertel et al., 2013; Kidder et al., 2013, 2018; Korchinski et al., 2012; Nachlas et al., 2014; Pennacchioni et al., 2010) or experiments (Nachlas & Hirth, 2015; Nachlas et al., 2018; Negrini et al., 2014). These studies have shown that strain-induced modification of [Ti] is a process influenced by several parameters, e.g.: the recrystallization processes (Haertel et al., 2013), the amount of finite strain (Bestmann & Pennacchioni, 2015), strain/stress partitioning, fluid percolation and redistribution (Bestmann & Pennacchioni, 2015; Nachlas et al., 2014), and the metamorphic path (e.g. prograde vs. retrograde: Negrini et al., 2014). In particular, to constrain the efficiency of [Ti] re-equilibration, during dislocation creep and subgrain rotation (SGR) recrystallization, is challenging (e.g. Haertel et al., 2013; Grujic et al., 2011). This is not trivial since dislocation creep is dominant in many quartzitic rocks at mid-crustal and, to some extent, lower crustal levels (Campbell et al., 2020; Hawemann et al., 2019). Considering the sluggish, intra-crystalline Ti diffusion in quartz over the temperature range where dislocation creep is predominant (Cherniak et al., 2007), strain-induced resetting of [Ti] is clearly enhanced by the grain size decrease (and increase of reactive grain boundary area per unit volume) during SGR recrystallization. In fact, this process results in reduction of diffusion lengths for re-equilibration and provides pathways for fluids to access the grain interior (Ashley et al., 2014). Enhanced diffusion along dislocation structures ("pipe diffusion") may also contribute to resetting (Nachlas et al., 2018).

Despite the evidence of strain-induced effects, the extent of re-equilibration of [Ti] during dislocation creep to the ambient conditions of deformation appears partial and highly heterogeneous across the strain gradients of quartz mylonites, as well-imaged by SEM-based cathodoluminescence (SEM-CL) maps (Bestmann & Pennacchioni, 2015). There is in fact a direct correlation between the [Ti] and the CL intensity in quartz (e.g. Spear & Wark, 2009; Wark & Spear, 2005). Heterogeneities in degree of re-equilibration of [Ti] occur between microstructural domains within zones of similar finite strain and remain heterogeneous in pervasively deformed and recrystallized quartz mylonites. This reflects the complexity of the microstructural evolution of coarse-grained quartz aggregates with diverse crystallographic orientations in different crustal rocks, e.g. in granitoids or pure quartz veins (Ceccato et al., 2017).

The use of TitaniQ, in quartz mylonites that underwent heterogeneous deformation in the dislocation creep regime, requires identification of the sites of most complete syn-kinematic [Ti] re-equilibration that do not necessarily correspond to the most strongly deformed domains. This identification is only possible through a rigorous protocol of integrated, high-resolution analysis by optical microscopy, SEM-CL, electron backscatter diffraction (EBSD) and direct measurement of [Ti] using secondary ion mass spectrometry (SIMS). SIMS measurements are necessary for quartz deformed under middle to upper or even high-pressure crustal conditions where equilibrium [Ti] are commonly below the ~7 ppm detection limit of electron probe microanalysis (Nachlas et al., 2018).

Matching the information from the different techniques is not only functional to TitaniQ thermobarometry, but also provides a robust interpretative tool for the interplay between grain-scale deformation, fluid-rock interaction, geochemical exchange and the evolution of the crystallographic preferred orientation (CPO) during increasing strain in a quartz mylonite. We present specific microstructures of deformed quartz veins from the Prijakt Nappe (Austroalpine Unit, Schober Mountains, Eastern Alps, Austria) as a key-study to unravel characteristic deformation processes responsible for partial to complete resetting of the Ti-in-quartz system under retrograde deformation condition in the SGR regime.

1. **Geological settings**

The studied samples of deformed quartz veins (2-10 cm thick) were collected near the Barrensee (Schober Mountains, Eastern Alps, Austria) within pre-Alpine paragneisses, orthogneisses and metabasites of the Prijakt Nappe (Austroalpine Unit; Figure 1) (Krenn et. al, 2012; Schulz, 1993). This nappe underwent Eo-Alpine (Cretaceous) subduction to eclogite-facies conditions at 650 °C and 1.9 GPa (Hauke et al., 2019). Quartz veins, that crosscut the eclogitic foliation, have been inferred to have developed at amphibolite-facies conditions (510-590 °C and 0.5-0.6 GPa) during rapid exhumation (Linner, 1999; Thöni, 2006).

In Oligocene-Miocene time, the tectonics of the Eastern Alps was dominated by the indentation of the Dolomites block (Southern Alps), delimited by the Giudicarie and the Periadriatic fault systems (Figure 1), against the Alpine stack. Indentation was accommodated within the Alpine stack by lateral escape, associated with the activity of a network of regional to smaller scale strike-slip faults (e.g., the Defereggental-Anterselva-Valles Line, DAV: Mancktelow et al., 2001) and uplift (Ratschbacher et al., 1989; Rosenberg et al., 2007). The Cenozoic deformation south of the Tauern window is dominated by strike slip faulting. Prior to intrusion of the main Periadriatic plutons at ~30 Ma the shear sense on W-E striking faults was sinistral. The transition from sinistral to dextral transpressive kinematics is related to the displacement along the Periadriatic fault, which continued at least until 13 Ma (Mancktelow et al., 2001).

East of the sample area, the Austroalpine Unit south of the DAV includes a series of ductile-to-brittle structures developed under low metamorphic conditions referable to the Oligo-Miocene faulting (Linner et al., 2009).

The studied Barrensee mylonitic quartz veins occur in association with a roughly W-E striking steeply-dipping strike slip fault with a strike-length of 300 m at an altitude of ~2850 m (UTM33 326383E/ 5199000 and 326674E/5199000N). The fault is localized in an up to 2 m broad zone with subvertical slickensides with subhorizontal slickenlines, cohesive cataclasites, black ultracataclasites and pseudotachylytes partly overprinted by a ductile SCC' fabric indicating dextral strike-slip kinematics (Figure 2c, d). The fault generally crosscuts the Eo-alpine metamorphic fabric in the host rocks, which is characterized by a complex pattern of refold structures. The investigated samples are from the eastern parts of the fault zone, where the metamorphic layering is subvertical and parallel to the fault, where the shear displacement is strictly localized in dm-thick foliation-parallel quartz vein forming the precursor structure (Pennacchioni & Mancktelow, 2018) of grey to blueish quartz-mylonites with a subhorizontal stretching lineation (Figure 2a). Up-to mm-size mica fish indicate dextral strike slip kinematics. Interestingly, in the vicinity of the mylonitized veins, no indication of cataclastic deformation, black ultra-cataclasites, pseudotachylites or SCC' fabrics have been observed. Mylonitization of the quartz veins only occurs within the narrow fault zone and ca. up to 4-5 m outside of the central part of the fault zone. Quartz veins further away do not show evidence of mylonitisation.

1. **Materials and methods**

The analyses were conducted on thin sections of sheared quartz veins orthogonal to the vein boundary (X-Y plane in the kinematic reference frame) and parallel to the stretching lineation (X-axis). The centre of the pole figures (PF), used for representing the CPO, corresponds to the shear zone kinematic vorticity axis (Y-axis).

We use optical microscopy, SEM-CL and EBSD to characterize the microstructures and CPO of quartz veins across strain gradients from weakly to strongly deformed domains parallel to the vein boundary. Based on CL images, where the CL signal is proportional to [Ti] (e.g. Bestmann & Pennacchioni, 2015; Wark & Spear, 2005), microstructurally-controlled measurements of [Ti] in quartz were carried out by SIMS. The correlation between [Ti] and intensity of the CL signal is corroborated by the SIMS measurements. Wavelength spectral analysis demonstrate that the CL signal depends only on the single emission peak at 400-420 nm (Figure S1). Despite very low [Ti] (0.1-4.7 ppm), CL was perfectly capable of imaging even sub-ppm Ti-variations. Because the highest CL intensities of weakly deformed quartz veins is also reflected in stretched protolithic vein crystals and porphyroclasts in mylonites, we limited our SIMS measurements to these last domains where the whole range of CL/[Ti] are present in association with a diversity of microstructures. Synchrotron-based X-ray fluorescence microscopy (XFM) was undertaken on the XFM beamline at the Australian Synchrotron (Howard, 2020) to identify µm-sized Ti-bearing phase within the vein that buffered the Ti activity.

Optical images in transmitted plane-polarized light and high-resolution SEM orientation contrast (OC) images were used to record the spatial density of small-scale pores (fluid inclusions, FI). This information, in combination with EBSD maps, was aimed at correlating variations in CL intensity (and corresponding variations in [Ti]) across the microstructure with the occurrence of fluids.

The composition of syn- and late-kinematic chlorite (with respect to the mylonitic deformation) was determined by microprobe analysis to apply chlorite thermometry (Vidal et al., 2005; 2006). This provides an independent, complementary estimate of temperature to TitaniQ.

A detailed description of the different analytical apparatus and procedures used in the study is reported in the Data Repository.

1. **Results**

Most veins are heterogeneously deformed with strain increasing towards the vein core or show a strain gradient from one vein margin (protomylonite) to the other (ultramylonite). Weakly deformed domains consist of mm-sized vein crystals (qtz_1) (Figure 3). With increasing strain, qtz_1 grains progressively stretched, their long axis rotated into parallelism with the shear plane (vein boundary) and dynamically recrystallized to different degrees depending on their crystallographic orientation (Figure 4). Relict qtz_1 grains persist as porphyroclasts in extensively recrystallized, strongly deformed domains (Figures 5-7). Initially, qtz_1 recrystallized into elongated (aspect ratio up to 10:1, hundred microns long) new grains (qtz_{2A}) (Figure 8). Then, highly sub-structured qtz_{2A} grains underwent mantle recrystallization to smaller (1-10 µm in diameter), equant new grains (qtz_{2B}). At high strains, the microstructure is still heterogeneous: the main foliation, parallel to the vein boundary, is defined by an alternation of dominant, recrystallized layers showing a distinct internal extinction banding (100-500 µm in thickness) and monocrystalline (commonly highly sub-structured) ribbon grains. The recrystallized layers show a CPO characterized by a single *c*-axis girdle with variable sub-maxima as reflected in the optical extinction banding (Figure 8). The foliation of deformed quartz veins is crosscut at a high angle by late-stage quartz, (qtz_3 ±chlorite) veins, which were only slightly involved in ductile deformation (Figures. 2b, 9, 10 and Figure S3c). The microstructural and CPO evolution, and the variations in [Ti] across the differently strained domains (imaged by CL and measured by SIMS) are described in detail below.

4.1. Weakly to moderately deformed quartz vein domains

The most preserved domains (Figure 3) contain mm-sized, weakly deformed quartz vein crystals (qtz_1). These "crystals" contain deformation bands, elongated subgrains and deformation lamellae, and show serrate grain boundaries (GB). The qtz_1 CL shade varies from medium to light grey with darker tones at GB (over a thickness of 20-40 µm). XFM element maps reveal dispersed inclusions of rutile grains (3-7 µm grain size) as inclusions in qtz_1 and along pristine microshear zones (Figure S2).

With increasing bulk strain qtz_I grains become (i) stretched to different degrees, depending on their crystallographic orientation relative to the kinematic reference frame, and (ii) separated by shear bands of recrystallized grains (qtz_2). Qtz_I grains show a high spatial density of low angle boundaries (LAB: misorientations < 10-15°). In qtz_I grains with *c*-axis oriented between the Y and Z-axis, the LAB misorientation axis plot shows clustering around <*c*> with a spread to the rhomb planes and to the {10-12} direction. *Qtz_I* grains with a peripheral *c*-axis orientation in the PF have more random LAB misorientation axes and higher degree of recrystallization. The selected, elongated *qtz_I* grain (aspect ratio of 10:1) of Figure 5, with *c*-axis inclined 37° to the Y-axis in the Y-Z plane, is highly substructured; the LAB misorientation axes cluster around <*c*> (Figure 5g) and the PF show a continuous dispersion around the {10-12} pole close to the Y-axis (Figure 5g). This *qtz_I* grain shows a similar CL-shade as the incipiently deformed quartz vein crystals (Figure 5b, e). In contrast, the recrystallized portions are darker in CL shade (Figure 5e), and associated with high angle boundaries (HAB: misorientation >10-15°) (Figure 5f, k') and pores (Figure 5i, j'). The interior of *qtz_I* grain shows a network of thin dark-grey CL lines (Figure 5e) that matches the LAB network (misorientation 0.5°-15°) of EBSD maps (Figure 5f). There are no visible pores associated with LAB (Figure 5k' ') in either the optical (Figure 5i) or OC images (Figure 5h, j' ').

4.2. Strongly deformed domains

Strongly deformed vein portions show a mylonitic foliation subparallel to the vein boundary defined by the alternation of layers of (i) dominant, recrystallized aggregates of *$qtz_{2A,B}$* with slightly different CPO reflected in the extinction banding, and (ii) monocrystalline, ribbon grains. This layering is partially reflected in a CL-shade layering (Figure 9a). The foliation wraps around local, mm-sized *qtz_1* porphyroclasts (Figure 4). In the following we highlight the correlations between the CL-patterns and [Ti] with the CPO, (sub)grain size and porosity distribution.

4.2.1. *Qtz_I* porphyroclasts

Most of the *qtz_1* porphyroclasts have a nearly peripheral *c*-axis orientation in PF, slightly rotated to the Z-axis against the sense of shear (Figure S3). Two different microstructural sites (*Site 1, 2*) have been selected for detailed study. *Site 1* (Figure 6) shows a cluster of *qtz_1* porphyroclasts (I-IV) mostly retaining the medium-light CL-shade of *qtz_1* of weakly deformed vein portions, corresponding to 3.6-4.1 ppm [Ti] (*SIMS-profiles 8-11, 13, 14*). Pores are rare or absent within the clast. As a whole the cluster defines a composite low-strain domain with the wrapping recrystallized *qtz_2* matrix showing CL variation between the contractional and extensional domains, developed at opposite quadrants around the porphyroclast cluster and induced by distortion in the non-coaxial (dextral) flow. The contractional domains show medium-dark CL shade and 1.3-2.7 ppm [Ti] (*SIMS-profiles 10, 15*). The extensional quadrants, including the recrystallized domain between I and III, show darker CL shade and 0.4-0.5 ppm [Ti] (*SIMS-profiles 7, 12*). These CL/[Ti] patterns well correlate with the density of HAB pores, higher in the Ti-poorer extensional domains (Figure 6a, d). The separation zone between porphyroclasts I and II (Figure S3) shows heterogeneous CL patterns with (i) larger irregular portions, partially retaining the typical CL-shade of *qtz_1*, and (ii) CL-darker domains. The formers are highly sub-structured, contain scarce pores and show a trend of decreasing [Ti] (1.3-2.2 ppm) from the values of the porphyroclast cores. The CL-darker domains include new *qtz_2* grains, have higher pore spatial density (Figure S3) and show lower [Ti] (0.4-0.7 ppm). Porphyroclast II locally shows decreasing CL intensity towards the rim (up to 50 µm in width; Figure 6f), in association with highly sub-structured domains (Figure 6h) almost free of pores (Figure 6g), corresponding to a progressive decrease of [Ti] from 3.0-4.0 ppm (clast interior) to 1.1 ppm (clast margin) (Figure 6a, *SIMS-profile 13*). [Ti] decrease to 0.9 ppm in the adjacent recrystallized pore-rich *qtz_2* aggregate.

Site-2 shows a *qtz_1* porphyroclast partially separated in two parts by a wedge-shaped domain of recrystallized *qtz_2* (Figure 7). The upper part has moderate-light CL shade and 3.3-3.7 ppm [Ti] (*SIMS-profiles 3, 5, 6*). The presence of localized pore clusters associates with darker CL shade (Figure 7c). The lower porphyroclast part shows a more heterogeneous CL pattern corresponding to a larger variation in [Ti] (2.0-3.9 ppm; *SIMS-profiles 1, 4, 5*). The set of thin CL-brighter lines corresponds to deformation lamellae (Figure 7g, h). The dividing recrystallization *qtz_2* aggregate shows homogenous dark CL shade, 0.2-0.5 ppm [Ti] (*SIMS-profiles 2, 4, 5*) and abundant HAB pores (Figure 7c, g, h). The CPO of the recrystallized aggregate consists of an oblique, single girdle with *c*-axis Y-maximum and peripheral sub-maxima (nearly overlapping with the host grain CPO) linked to low-strain tip of the recrystallized aggregate (Figure 7f). There is no noticeable change in CL signal within the porphyroclast associated with the strain gradient towards the tip of the recrystallized aggregate (Figure 7f-h, ellipse). A dark CL shade is also observed for very thin (single-grain-thick) micro-shear zones of recrystallized *qtz_{2B}* showing HAB porosity (Figure 7f-h, black arrow). There is also no noticeable change in CL between recrystallized aggregates of *qtz_{2A}* and *qtz_{2B}*.

4.2.2. Monocrystalline lenticular quartz

Qtz_1 grains are progressively stretched into lenticular, high aspect-ratio, monocrystalline grains bending into the mylonitic foliation subparallel to the vein boundary. *Qtz_1* grains less favourably oriented for prism$<a>$ slip (*c*-axis angle to Y: >54°) tend to recrystallize as soon as the clasts bend into the shear foliation (*ribbon-clast-1, 2* in Figure 9a and Figure S4). This goes along with the overall change to darker CL-shades associated with the appearance of a high spatial density of HAB pores. The recrystallized grains commonly contain brighter CL remnant cores. Extensive recrystallization is especially observed for ribbon-clasts with *c*-axis at the PF periphery (*ribbon-clast-1*). Instead of a main clustering of LAB misorientation axis parallel to $<c>$ a tendency around $\{m\}$ is evident suggestive of basal$<a>$ and/or $<c+a>$ slip (Neumann, 2000) (Figure S4c-I). Deformation zones, showing different degree of recrystallization, are commonly localized between the ribbon-clasts. However, independently of the accommodated amount of strain, the localized zones reveal a resetting towards low CL intensities and low [Ti] (0.3-1.0 / 1.8 ppm; *SIMS-profile 13*, Figure 9a).

4.2.3. Ribbon grains

In general, ribbons preserve a light CL-shade similar to, or slightly darker than, that of qtz_I grains (Figure 9a). The corresponding [Ti] vary between 3.0-4.7 ppm (lighter ribbons: *ribbon-1, 2*) and 1.6-3.2 ppm (darker ribbons: *ribbon-3, 4*). All ribbons contain a high spatial density of LABs (Figure 9b-IV, Figure S5d) with a main cluster of misorientation axis around <*c*> and additional clusters are towards $\{r\}/\{z\}$ and { }, even for misorientation angles >10-15° (Figure S4c-I *ribbon-4*). The internal HAB are mostly not interconnected. The cellular-structure with a high CL shade present within some ribbons (e.g. *ribbon-2*, Figure 9, Figure S4) corresponds to LABs not associated with detectable [Ti] variations; this structure likely corresponds to intrinsic lattice defects of SGB (Hamers et al., 2017). Ribbons with the *c*-axis next to the Y-axis (*c*-axis angle to Y   25°; *ribbon-2*) are the most elongated ones (up to 1 cm long and 250 µm thick) (Figure S4a, c-I). The LAB misorientation axis are subparallel to <*c*> and correspond to prism<*a*> slip (Neumann, 2000). Ribbons with *c*-axis orientation between Y and Z (angle 40-44°) show a main clustering of LAB misorientation axes (sub)parallel to <*c*> but also towards $\{r\}$ and $\{z\}$; this is suggestive of both prism<*a*> and rhomb<*a*> slip (Neumann, 2000). These grains show a higher degree of recrystallization at their ends where the CL signal gets weaker. In general, ribbons are nearly free of porosity (Figure 9b-II), except for some specific clusters and in zones of incipient recrystallization.

4.2.4. Strongly deformed, pervasively recrystallized aggregates

Pervasively recrystallized aggregates are characterized by extinction banding and corresponding CL variations (layer thickness 100-500 µm) (Figure 4a, b and Figure 9). The CPO of the different layers indicate a variation in the distribution of the *c*-axis submaxima within the *c*-axis girdle, mainly located between the Y and Z direction of the PF (Figure S4c-II). The distribution of LAB misorientation axes mainly cluster around <*c*>. We used the density of the clustering (multiple of random distribution, *mrd*, for misorientation angle interval 2-10°) to quantify the activity of slip system, especially prism<*a*>. The *mrd* values varies for different CPOs (position of the *c*-axis sub-maxima). In general, the closer the *c*-axis sub-maxima is to the Y-axis the higher is the *mrd*. For some (ultra)mylonitic areas there is a tendency that layers with dark CL show higher *mrd* values, corresponding to *c*-axis clustering towards Y-axis (e.g. *mylonite-5* - dark CL, *mrd* 4.2; Figure S4c-II). Adjacent layers with a brighter CL signal are characterized by lower *mrd* values and more peripheral *c*-axis sub-maxima in PF (*mylonite-3* and *6* – brighter CL, *mrd* 2.9 and 2.8). The darker CL layers commonly display a higher degree of smaller (sub)grain size and accompanied higher pore spatial density than CL-brighter layers. However, this is not always true and no strict correlation between CL, CPO, misorientation axis distribution, (sub)grain size and FI density can be demonstrated. For example, *area-A* is completely recrystallized where a layer with brighter CL signature (thickness 300 µm) is surrounded by either sides by layers with darker CL signature (Figure 8). However, the brighter CL *layer-2* shows a cluster of *c*-axis in the centre of the PF (Y-axis), whereas the *c*-axis sub-maxima of the adjacent *layers-1* and *3* (dark CL) tend to localize further away from Y and/or a located near the PF periphery. This is also reflected by the *mrd* values of the LAB (clustering around $<c>$) showing higher values for *layer-2* (mrd 7.45) compared to lower values for the adjacent *layers-1* (*mrd* 4.58) and *layer-3* (*mrd* 5.29). Further, all three layers show the same (sub)grains size distribution and there is no obvious variation of the FI density. FI occur mainly along HAB but are also present along LAB (Figure 8f, g).

In sample (*MS-09a*) strongly deformed vein portions show a characteristic extinction banding but a relatively minor corresponding CL variation (Figure 4c, d). With respect to qtz_1 of weakly deformed parts the mylonitic aggregate have a slightly to moderately decreased CL-shade (Figure 4d). A strong reduction in the CL signal is only observed in strain shadows between coarse quartz clasts (Figure 4g, h). It is important to note, that only the microstructures with a dark CL signal contain a high spatial density of pores. In contrast, the (ultra)mylonitic matrix with its relatively homogeneous moderate CL signal is characterized by a very low FI density, where only sporadically FI are evident along HAB.

The SIMS data reveals very homogenous low [Ti] (0.3 – 0.6 ppm) for the dark CL layers (Figure 9a). The brighter (ultra)mylonitic CL layers are more heterogeneous in the [Ti] (0.8-2.2 ppm) which is also reflected by the heterogeneous CL microstructure. Many of the elongated recrystallized grains show brighter CL cores and darker structures along the HAB especially where FI are evident. In general, CL intensity can vary within and between these layers.

4.3. Late-stage quartz (LSQ, qtz_3) veins

Late-stage quartz (LSQ) veins (locally accompanied by chlorite) crosscut the main foliation of the deformed quartz veins. These veins are easily identified in CL images by their dark, homogeneous shade crosscutting the CL banding of the deformed vein (Figure 10a, e). Thin LSQ veins can be easily overlooked under the optical microscope due to the epitaxial growth of the quartz infilling on the host-vein quartz. These veins are slightly involved in ductile deformation and show the same type of deformation features as the hosting quartz and therefore are called syn-kinematic late stage quartz veins. In Figure 10f the host ribbon grain (qtz_1) and the filling of the crosscutting vein (qtz_3) show (i) the same dispersion patterns of the CPO in PFs, and (ii) similar clustering around $<c>$ and around the Y-axis in the misorientation axis plots in crystal and sample coordinates, respectively. Only minor dynamic recrystallization is recorded in the LSQ veins as result of the small accumulated strain. The homogeneous, dark CL shade corresponds to [Ti] in the range of 0.1-0.5 ppm (mainly 0.1-0.3 ppm) (*SIMS-profile 5, 6, 11* and *12* in Figure 10a).

4.4. Chlorite thermometry

We applied chlorite thermometry (Bourdelle, 2021) in order to have an independent information on the deformation temperature to complement the Ti-in-quartz estimates. This method has been shown to be particularly efficient for determining deformation temperature in the greenschist facies (Calzolari et al., 2018; Cantarero et al., 2014; Lacroix et al., 2012; Mizera et al., 2020; Zihlmann et al., 2018). We used the calibration of Vidal et al. (2005; 2006), which is based on two independent internal equilibria amongst the end members of the chlorite solid solution in presence of quartz and H_2O (see Ganne et al., 2012 for calculation details).

Chlorite from the investigated samples were classified from microstructural observation as pre-, syn- and late-kinematic with respect to the mylonitic deformation event of the quartz veins. Syn- and late-kinematic chlorites from three different microstructural sites in three sample (Figure S6) were analyzed with an electron probe microanalyzer (see Data Repository for method). An equilibrium temperature was calculated for each analysis, assuming a pressure of 0.3 GPa (see *section 5.3.2.2.* for explanation, Table 1). Syn-kinematic chlorite from shear bands and strain shadows (Figure S6a) yielded values between 238 and 268 °C. Chlorite growing in garnet cracks as retrogression product is interpreted as syn- to late-kinematic (Figure S6b) and yielded temperatures in the range 272-352 °C. The unoriented chlorite from a late-stage syn-deformational quartz veins crosscutting the mylonitic foliation (Figure S6c, see *section 4.3*) yielded temperatures between 265 and 333 °C.

A minimum error of 30 °C (Plunder et al., 2012) to 50 °C (Powell & Holland, 2008) should be applied to results of thermometry. Increasing the input pressure to 0.5 GPa induces an increase of the sample average temperature lower than 10 °C and changing the range of accepted ferric iron indicates that the impact of this parameter remains within 50 °C. With an uncertainty of 50 °C, the average temperatures in the three microstructural sites overlap within error, implying that syn- and late-kinematic chlorite grew at similar conditions. Only one sample yielded temperature consistently below 300 °C (Table 1). Owing to the irregular surface of chlorite in shear bands and strain shadows in this sample (Figure S6aIII) and the small number of analyses, less weight should be put on this sample. We therefore conclude that chlorite thermometry provides a reasonable estimate of 300±50 °C for the deformation temperature, most likely in the upper part of this range.

5. Discussion

5.1. Conditions of quartz vein formation and deformation

The development of the Barrensee quartz veins has been referred to amphibolite-facies conditions, constrained at 510-590 °C and 0.5-0.6 GPa (Linner, 1999). The quartz veins were later exploited as ductile shear zones along a sub-vertical ca. W-E-striking pseudotachylyte-bearing fault/shear zones, with dextral strike-slip kinematics, cutting discordantly the main foliation of the host rocks. A strike-slip kinematics, and the association with pseudotachylytes, is typical of the Oligocene-Miocene faulting in the Austroalpine and Penninic units of the Eastern Alps (Ceccato & Pennacchioni, 2018; Mancktelow et al., 2001). These strike-slip faults, including major faults like the DAV fault (Mancktelow et al., 2001), accommodated shortening and the lateral escape of the Alpine stack at the front of the Dolomites block (Southern Alps) indenter (Ratschbacher et al., 1989). Since only dextral shear sense is recorded in the mylonites and the brittle fault rocks, the shear zone most likely belongs to the dextral Periadriatic fault system active after 30 Ma (Mancktelow et al., 2001). This postdates the Cretaceous/Paleocene exhumation constrained by biotite Rb/Sr ages (Linner, 1999) and indicates that deformation took place at the basal part of the upper crust, consistent with (i) the temperatures estimated from the chlorite thermometry, and (ii) the occurrence of ultra-cataclasites and pseudotachylytes coeval with ductile shearing in the quartz veins. Alternatively, the mylonitization of the quartz veins could have happened earlier during the Cretaceous/Paleocene exhumation and the investigated fault exploited the mylonitic foliation as a preexisting anisotropy in a favourable orientation for brittle-ductile strike-slip in the Oligocene/Miocene. However, the mylonitic quartz veins have only been observed in the investigated fault and the mylonitic quartz veins do not record any evidence of cataclastic reworking and therefore we favour the interpretation that mylonitization of the quartz veins was coeval with brittle-ductile strike-slip faulting at low-greenschist facies conditions.

5.2. Resetting of [Ti] during deformation

Resetting of [Ti] from initial 3-4 ppm of coarse-grained qtz_1 grains down to 0.3-0.5 ppm of recrystallized qtz_2 grains in strongly deformed domains is heterogeneous. Two main factors apparently caused resetting: (i) the amount of fluid in combination with dynamic recrystallization, responsible for the strongest resetting, and (ii) the development of SGB. The SIMS analysis have established the univocal correlation between the CL signal and [Ti]. In the following we use the term resetting to indicate the decrease of the [Ti] with respect to that of pristine vein quartz crystals, corresponding to change to darker CL grey shades. We discuss the influence of different parameters (fluids, recrystallization, CPO, clast orientation, strain, and available) on the [Ti]/CL resetting.

5.2.1. Effect of fluids

Synkinematic infiltration and/or re-distribution of free aqueous fluids (e.g. released from FI of the protolithic quartz vein grains during deformation) played a major role on [Ti] resetting. The main mechanism producing grain-scale fluid pathways is SGR recrystallization resulting in a pervasive network of fluid-permeable grain boundaries (GB). As a result, there is a general switch to dark CL-shades and low [Ti] from qtz_1 grains to qtz_2 recrystallized aggregates. GB permeability is witnessed by widespread occurrence of pores along HAB, as reported in other quartz mylonites (Fitz Gerald et al., 2006). In contrast, LAB are either free of porosity or show only a minor porosity. The syn-kinematic timing of fluid infiltration is well documented in Figure 6a, where there is a distinct degree of [Ti] resetting, in the recrystallized quartz matrix surrounding the composite quartz porphyroclast, between the low pressure domains (preferential sink of fluids and with stronger resetting) and the high pressure domains (weaker resetting) (see schematic stress field, marked in Figure 6a). The contrast in CL shade between extensional and contractional sites is not associated with a change of CPO of the qtz_2 aggregate or of the active slip systems (Figure 6a-c). [Ti] resetting along GB commonly affects a thickness of as much as several tens of micron of the grains (Figure 6a, Figure S3). This may result from a component of dissolution-precipitation in the recrystallized aggregate accompanying the predominant SGR recrystallization. An enhanced resetting may result from a combination of diffusion creep (pressure solution) and the movement of HAB through the strained aggregate in the dislocation creep regime accompanied by SGR recrystallization (Yund & Tullis, 1991). Complete resetting is also evident even when the degree of recrystallization and the strain are low (Figure 7f-h, ellipse) or is strictly localized along interconnected HAB (black arrow). On the other hand, in high strain zones at the compressional quadrants around clasts the GB fluid was drained and moved to extensional and dilatant zones under microscale pressure gradients (Figure 6a). Therefore, in compressional quadrants resetting took place to a minor extent despite the persavive dynamic recrystallization (see also *section 5.2.1.3*). In contrast, within strongly localized and recrystallized microstructures, e.g. shear bands in the protomylonites (Figure 4a-d; Figure 5a, b) or in clast-related microstructures in the (ultra)mylonites (Figure 4d, h), available fluids were channelized and promoted a strong resetting.

Along GB, but locally also along SGB, a CL gradient towards the grain interior is observed. Cherniak et al. (2007) showed that diffusion distances are limited at low temperatures. Ti volume diffusion over a distance of 1 µm should take more than 1 Ma at ~300 °C (the inferred deformation temperature of the Barrensee quartz veins). This diffusion rate is too sluggish to explain the observed 3-10 µm-thick [Ti] zonation. However, dislocations can act as fast diffusion pathways – a process known as pipe diffusion (Legros et al., 2008). Most diffusion experiments have been carried out under static condition and therefore probably underestimate diffusion rates of deformation microstructures (Chakraborty, 2008, and references within). In deformation experiments, Yund et al. (1981) concluded, based on dislocation density gradients, that pipe diffusion enhanced diffusion coefficient for oxygen and therefore promoted faster chemical exchange in albite. Piazolo et al. (2016) showed direct evidence by atom probe tomography that trace elements within deformed zircons are concentrated along dislocations piled up at SGB. For the Barrensee quartz veins the [Ti] are too low to carry out atom probe analysis. However, since CL gradients mainly occur where GB and SGB are correlated with a high FI density we presume that diffusion is promoted by the presence of fluids in any case.

5.2.1.2. Effect of subgrain boundaries

Resetting related to SGB ranges from (i) a strongly localized effect along individual SGB to (ii) a nearly homogeneous effect in strongly substructured (high spatial density of SGB) domains. In both cases, an associated porosity is basically absent, and the degree of resetting is minor compared to wetted GB and SGB.

1. *Local [Ti] resetting along SGB*

In Figure 5e the network of thin dark-grey CL lines within the qtz_1 grain correspond with the LAB network. Dislocations along SGB can cause non-bridging oxygen hole centre defects under electron irradiation and act as intrinsic defects producing a 650 nm emission peak in the red wavelength range in quartz (Hamers et al., 2017 and references within). However, the above described CL network is not visible using a red filter (600-700 nm) therefore excluding that intrinsic defects are responsible for the observed feature. We refer the dark-grey CL network to [Ti] variations associated to diffusion along SGB. Note the strongly localized reduced CL signal along SGB is too small for SIMS analysis (beam spot size ca 10x15 µm, see methodical section in Data Repository). Nachlas et al. (2018) observed that Ti-undersaturated coarse-grained quartz clasts, experimentally deformed in a fine-grained Ti-saturated quartz matrix, show slightly higher CL intensities along SGB and to some extent also a broader diffusion pattern from the SGB into the host grains.

1. *Homogeneous [Ti] resetting in areas with high SGB density*

The observed partial resetting along stretched qtz_1 margins (up to 50 µm, Figure 6a, f) cannot result from the sluggish volume diffusion of Ti within intact quartz at greenschist facies conditions (see above and *section 5.2.1.*). Rather synkinematic rearrangement of SGB and migration within the relatively highly strained grain margins can explain the process of resetting. SGB migration was observed in metals, analogue materials (Drury et al., 1985; Urai et al., 1986) and in rock-salt (Bestmann et al., 2005). Because SGB do not show any associated porosity, this type of resetting seems not to imply a role of fluids, at least at the submicron level. Nachlas et al. (2018) argued that SGB migration is also able to reset the deformed parts of the grain, where SGR recrystallization is evident, to uniform higher [Ti] with respect to the host with original lower [Ti].

5.2.1.3. Effect of clast orientation, strain, recrystallization and available fluid in strongly deformed vein portions

Highly strained quartz-ribbons with high SGB spatial density and misorientation axis around <*c*> preserve the pristine CL/Ti signal (e.g. *ribbon-2,* Figure 9a). This was also observed in the experiments of Nachlas et al. (2018). Therefore, continuous SGB rearrangement by mainly prism<*a*> slip, not leading to dynamic recrystallization, allows homogeneous crystal deformation without resetting. Only marginal resetting takes place with the nearly FI-free quartz ribbons acting as barriers for fluids. However, at incipiently recrystallized ribbon-tips, a higher FI density is evident and is associated to a stronger resetting.

In the ultramylonite with the characteristic extinction banding there is no strict correlation between [Ti]/CL and the CPO (LAB misorientation axis and related slip systems), the FI density and the (sub)grain size (Figure 9, Figure S4). However, the original orientation of the vein crystals apparently plays a major role for the microstructural evolution during increasing deformation (Ceccato et al., 2017). The degree of the [Ti] resetting depends strongly on the amount of the available fluids, and only to a minor degree on the "cycles" of dynamic recrystallization (Figure 4d). A strong resetting occurs where fluids were channelized (shear bands) or concentrated in dilatant sites (Figure 4d) in combination with recrystallization and dissolution-precipitation (Bestmann & Pennacchioni, 2015). At comparable strain/recrystallization microstructures with lower fluid/rock volume ratio show minor [Ti] resetting than the ones with a high fluid/rock volume ratio (Bestmann & Pennacchioni, 2015). Thus, the moderate and incomplete resetting took place under relative dry conditions due to continuous rearrangement and movement of SGB and GB during ongoing cycles of SGR recrystallization. Ashley et al. (2014) and Bestmann & Pennacchioni (2015) already suggested the importance of an inter-crystalline fluid to promote Ti-removal from quartz during deformation by SGR recrystallization.

In summary, under conditions where SGR recrystallization and prism $<a>$ intracrystalline slip are predominant, deformation-induced resetting of Ti in the deformed quartz veins remains heterogeneous up to high strain and pervasive recrystallization. The different crystallographic orientation of the vein crystals determines whether quartz persists as relatively low-strain porphyroclasts or stretches into mono-crystalline ribbons or recrystallizes to mylonitic aggregates. Dynamic recrystallization by SGR represents an efficient process to dramatically increase the GB surface area per unit volume and, especially, results in an invasive permeability network, allowing fluids to reach grain interior, and decreasing the diffusion length for compositional exchange. In fact, HAB commonly host GB fluids and, therefore, recrystallization enhances permeability and fluid-assisted Ti re-equilibration. Microscale strain heterogeneities also result in pressure gradients that guide fluid redistribution and differential Ti re-equilibration between fluid-rich and fluid-poor domains even in fully recrystallized aggregates. In fact, fluids appear the main agent of Ti re-equilibration. In contrast to HAB, LAB are in most cases impermeable to fluids and induce only subordinate Ti re-setting. In mylonites, containing recrystallized highly elongated grains qtz_{2a} surrounded by small qtz_{2b} grains, commonly show a CPO banding, reflecting the derivation from original crystals with different crystallographic orientation that control the selective activation of the main intracrystalline slip systems. This CPO banding is in part reflected in the Ti re-setting indicating that the CPO affects the strength and fluid redistribution in dependence of the original orientation of the vein crystals and the amount of strain within each band, and finally the amount of fluid.

5.2.2. Influence of late-stage syn-deformational quartz veins

The fluid infiltration associated with the formation of the late-stage quartz (qtz_3) veins does not have any significant effect on the [Ti]/CL signature of the crosscut mylonitic fabric. The crosscutting new qtz_3 veins show a homogenous dark CL shade sharply in contact with the CL banding of the host quarzt vein (qtz_1, qtz_2) except for a very limited, micron-scale halo in contact to the ultramylonite (Figure 10c). This indicates that fluid percolation across the quartz veins was actually only effective during synchronous mylonitization by crystal-plastic deformation. The evolving grain-scale microstructure during flow (especially associated with new GB formation by SGB recrystallization) provided transient and mobile porosity allowing fluid transport. This is consistent with the observed partitioning of fluids along pressure gradients induced by flow perturbation around porphyroclasts.

5.3. Application of TitaniQ

5.3.1. TitaniQ of quartz vein formation

TitaniQ calibrations (Huang & Audétat, 2012 – HA12; Thomas et al., 2010 – TH10;) are based on synthetic quartz grown from silica-saturated aqueous fluid in presence of rutile. Synchrotron analysis of the Barrensee veins reveals the occurrence of rutile inclusions in coarse quartz vein crystals and within recrystallized shear bands. This constrains TiO_2 activity (a_{TiO2}) to unity (e.g. Thomas et al., 2010). Assuming the pressure estimates of Linner (1999), the TH10 of pristine [Ti] (3.0-4.7 ppm) preserved in deformed quartz clasts yields 388-410 °C (0.5 GPa) and 405-427 °C (0.6 GPa). HA12 results in approximately 100 °C higher temperatures, 492-519 °C and 507-534 °C. The TH10 calculations are far below the vein crystallization temperatures (510-590 °C) inferred by Linner (1999).

5.3.2. TitaniQ of quartz vein deformation

5.3.2.1. Influence of deformation processes and related microstructures for Ti-in-qtz re-equilibration

Several studies have shown that SGR recrystallization is inefficient to cause [Ti] re-equilibration (e.g. Ashley et al., 2013; Grujic et al., 2011). Grujic et al. (2011) concluded that only grain boundary migration (GBM) above ~540 °C causes a complete [Ti] resetting. Nachlas et al. (2018) showed experimentally that SGB migration is able to promote [Ti] resetting. Haertel et al. (2013) inferred that, during retrograde deformation, SGR together with fluid-mediated bulging recrystallization were capable of re-equilibrating [Ti] at 350-400 °C, but concluded that the sole SGR recrystallization did not. All these studies inferred that SGR recrystallization represents a structural rearrangement of the lattice coupled with grain size reduction, but does not involve SiO_2 transport and, therefore, is not efficient for [Ti] re-equilibration. Further, the duration (cycles) of dynamic recrystallization and the amount of strain were inferred to play an important role in [Ti] resetting (Ashley et al., 2014; Bestmann & Pennacchioni, 2015; Kidder et al., 2013; Nachlas et al., 2015). In this view, ultramylonites (i.e. portion of nearly complete dynamic recrystallization) should represent the best candidates for applying TitaniQ. Here we show that the amount of free fluids percolating through the specific microstructure (especially along GB) is critical in controlling [Ti] resetting. Not a precise strain threshold is essential, instead an almost complete resetting occurs along wetted HAB and/or where dilatation sites provided sinks for fluids and synkinematic quartz precipitation (Bestmann & Pennacchioni, 2015; Haertel et al., 2013). In those microstructures the [Ti] (0.2-0.3 ppm) is in the same range as in (ultra)mylonitic layers (showing high FI density) characterized by homogeneous low dark CL and corresponding homogeneous low [Ti] (0.3-0.6 ppm).

5.3.2.2. Application of TitaniQ to (ultra)mylonites

As discussed above (*section 5.1*), it can be reasonably assumed that the Barrensee veins were deformed at the base of the brittle-ductile transition of the crust, ~300-350 °C that roughly occurs at 10-12 km depth (e.g. Hirth & Beeler, 2015), corresponding to ~0.3 GPa. Acosta et al. (2020) pointed out that HA12 was experimentally calibrated at lower pressure (0.1-1.0 GPa) than TH10 (0.5-2.0 GPa), and should ideally be more suitable for the Barrensee quartz veins. At 0.3 GPa, the temperatures calculated with the 2 calibrations differs of ca. 70-100 °C for a [Ti] range of 0.2-0.6 ppm and for an a_{TiO2} range of 0.1 and 1 HA12 yields systematically higher temperatures. Provided the assumed ambient conditions of ~300-350 °C are correct, temperature values in this range are obtained with HA12 with $a_{TiO2} = 1$ (320-369 °C) or with TH10 with $a_{TiO2} = 0.2$ (305-355 °C). If our multi-methodological microstructural analysis allows identification of proper sites of compositional re-equilibration for TitaniQ, the use of the HA12 and TH10 calibrations need to have a rigorous constrain on the Ti activity for the application of the thermometer (and the choice of the appropriate calibration). Small rutile inclusions are present within the coarse quartz vein crystals as well as along the crosscutting MSZ showing the same dark CL-shades as the ultramylonitic samples analysed by SIMS (Figure S2g, h). Further, during dynamic recrystallization rutile inclusions within qtz_I grains are exposed into the qtz_2 matrix and get in contact with the GB fluid. Therefore, we infer that mylonitic deformation occurred under Ti-saturated conditions due to water-assisted rapid diffusion along the interconnected GB network (Bromiley & Hiscock, 2016; Farver & Yund, 1991; Nachlas et al., 2018; Thomas & Watson, 2014). In summary, the calculated temperature of 320-369 °C using HA12 (as the low-pressure TitaniQ calibration) and $a_{TiO2} = 1$ apparently represents the most reliable estimate for the mylonitization of the Barrensee quartz veins.

5.4. Temperature estimates vs. quartz microstructure in the Barrensee quartz veins: a paradox?

In the deformed Barrensee quartz veins, subgrain rotation (SGR) and accordingly SGR recrystallization was the dominant deformation process and prism<*a*> the easiest intracrystalline slip system (Figure 8d and Figure S4cI+II) (Neumann, 1999). Despite a recrystallization process and a CPO cannot be taken as univocal representative of a specific temperature range, SGR recrystallization and prism<*a*> slip have been commonly described for quartz at upper greenschist to amphibolite facies deformation conditions (Behr & Platt, 2011; Ceccato et al., 2020; Stipp et al., 2002). Ceccato et al. (2020) constrained in the range 420-460 °C, by petrologic pseudosections, the deformation of quartz (by dominant SGR and prism <*a*> slip) within different granitoid plutons (Adamello, southern Alps: Pennacchioni et al., 2010; Sierra Nevada, California: Pennacchioni & Zucchi, 2013; Rieserferner, Eastern

Alps: Ceccato et al., 2020). In study cases where deformation occurred over a temperature range (e.g. 250–700 °C in the Tonale shear zone: Stipp et al., 2002; 300–550 °C in the Whipple Mountains core complex: Behr & Platt, 2011) the intracrystalline slip system is observed to evolve from prism $<a>$ at high temperature/low stress to a mixture of basal $<a>$, prism $<a>$, and rhomb $<a>$ at intermediate temperatures and stresses to basal $<a>$ at low temperatures/high stresses. At low temperatures for crystal-plasticity of quartz (250-300 °C) recrystallized quartz display a basal $<a>$ fabric (Kirschner & Teyssier, 1991).

The examples selected above support the widely shared opinion that SGR and prism $<a>$ record temperatures significantly above the limit of crystal-plasticity of quartz (at around 250 °C: Stipp et al. 2002). This rises a major, provocative query as to whether the deformation temperatures inferred here for the Barrensee quartz vein mylonites are correct or not. Different observations converge on lower greenschist facies temperatures for the shear/fault zone deforming the quartz veins: (i) the strike-slip kinematics and the association with coeval pseudotachylytes typical of the Oligo-Miocene faults in the region (Ceccato & Pennacchioni, 2018; Mancktelow et al., 2001); (ii) the chlorite thermometry; (iii) the TitaniQ thermometry. All these constraints are individually disputable, but together represent a more robust indication towards low temperature conditions of deformation. This is a relevant question that should be addressed in future research. If the assumed temperature of deformation underestimates the actual one, this results in a critical assessment on the reliability and applicability of the TitaniQ as previously discussed by Asley et al. (2014) and Bestmann & Pennacchioni (2015). This would imply that the experimental calibration of the TitaniQ is not applicable to the natural mylonite, despite the sites of most complete strain-induced [Ti] resetting may be identified by a rigorous microstructural s.l. analysis. On converse, if the assumed temperature of deformation is correct, this implies a revision of the commonly assumed temperature range for dominant dislocation creep, SGR recrystallization and prism $<a>$ slip with the lower limit moved to lower temperatures than commonly expected.

6. Conclusions

The study of the Barrensee quartz veins (Prijakt Nappe, Austroalpine Unit, Schober Mountains, Eastern Alp) indicates that deformation-induced Ti-in-quartz resetting is possible in the regime of subgrain rotation (SGR) recrystallization. Field constrains and chlorite thermometry suggest that quartz vein deformation occurred at low temperatures (350 °C) in the ductile field at the base of the brittle crust. The microstructural complexity of the quartz mylonites requires a careful selection of the domains of most complete re-equilibration for applying TitaniQ. This is only possible through a detailed correlated analysis by optical and SEM (cathodoluminescence, CL; orientation contrast, OC; and EBSD) microscopy as necessary pre-requisite to Ti measurement. The measured Ti concentration [Ti] in most complete re-equilibrated mylonitic domains (e.g. strain shadow or shear bands) yield consistent TitaniQ temperatures for the condition close to the brittle-ductile transition and rutile-buffered Ti activity. This is unusual for SGR and prism <a> slip, considered to pertain to higher temperature ranges of quartz deformation. If the temperature estimate in our study is correct, our results undermine this commonly agreed belief and have profound implications in the interpretation of quartz microstructures. Future work should search for additional constrains of the temperature conditions of the quartz vein deformation.

Acknowledgements

This work was funded by the Deutsche Forschungsgemeinschaft DFG (BE 2413/3-1). GP acknowledge funding from the University of Padova (BIRD175145/17). Access to the SEM-EBSD facilities was provided by the Department of Werkstoffwissenschaften WW1, FAU Erlangen-Nürnberg, Germany. The Oxford Instruments CMOS-Symmetry EBSD detector was funded by the DFG (JA 2718/3-1). Jay Thomas is thanked for providing the synthetic Ti-doped quartz standard (QTiP-38, Ti 380 ppm), Djordje Grujic for the natural standard (TN-06, 0.3 ppm) and Steven Kidder for the Herkimer "Diamond" used as a Ti blank. Cees-Jan De Hoog is thanked for conducting SIMS measurements and processing at the School of Geosciences of the University of Edinburgh. We acknowledge Holger Stünitz for discussion and providing access to the SEM-CL spectra facilities at the Department of Geosciences at the Arctic University of Norway (Tromsö), and Amicia Lee and Tom-Ivar Eilertsen for their assistance. Christoph E. Schrank and Nicholas W. Phillips are thanked for their contribution with respect to the synchrotron data set. Part of this research was undertaken on the XFM beamline at the Australian Synchrotron, part of ANSTO. Rene Romer is thanked for support during electron microprobe analysis (chlorite thermometry) and Friederike Urban and Raphael Njul for sample preparation. Alexis Plunder is thanked for the chlorite thermometry blind test.

Data Availability Statement

The EBSD, WDX, SIMS and Synchrotron X-ray Fluorescence data used in this study are publicly available at http://doi.org/10.5281/zenodo.4923150

Appendix A. Supplementary material

Supplementary material related to this article can be found online at ....

Author contributions

M.B., G.P. and B.G. conceived the idea, undertook fieldwork and contributed to equal parts to the discussion and interpretation of the data set. M.B. carried out sample preparation, microstructural analysis by light microscopy, scanning electron microscopy (SEM-CL, SEM-CL spectra, SEM-OC, EBSD) & processing, electron microprobe (EMP) and worked out the workflow for Ti-in-qtz analysis by Secondary Ion Mass Spectrometer (SIMS, in cooperation with Cees-Jan De Hoog). B.H. processed the EMP data and applied the chlorite (Chl) thermometer. B.H. and B.G. constrained the deformation condition based on

Chl-thermometry data and the geological setting. M.B. applied the TitaniQ thermometer. M.W.M.J. and C.M.K collected and analysed the X-ray Fluorescence Microscopy data. M.B. wrote the ms with the contribution of B.G. and G.P. B.H. wrote the chlorite thermometry part and M.W.M.J. the synchrotron methodical part in the Supplementary Material.

Declaration of competing interest

The authors declare that they have no known competing financial interests or personal relationships that could have appeared to influence the work reported in this paper.

Figures

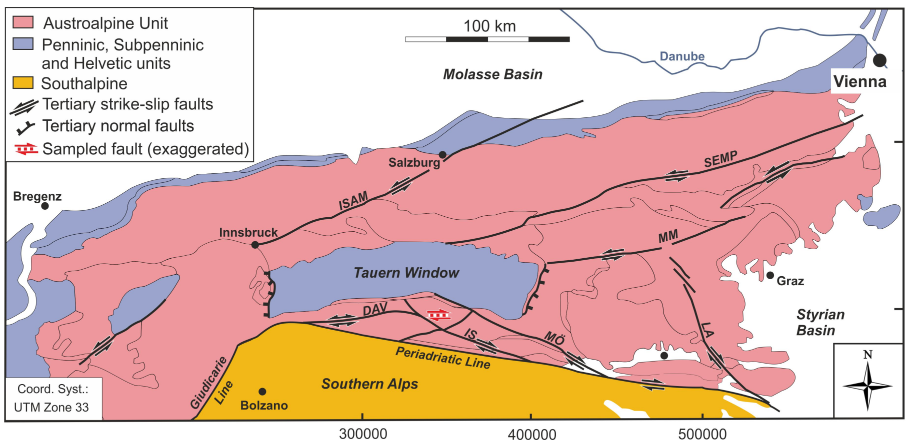

Figure 1. Simplified geological map of part of the Eastern Alps (modified after Schuster et al., 2014). Important Tertiary fault systems are given. Note sampled fault (red stippled line) is a continuation in strike of the Defereggental-Anterselva-Valles fault (DAV). Innsbruck-Salzburg-Amstetten fault (ISAM); Salzach-Ennstal-Mariazell-Puchberger fault (SEMP); Mur-Mürztal fault (MM); Lavanttal fault (LA); Mölltal fault (MÖ); Iseltal fault (IS).

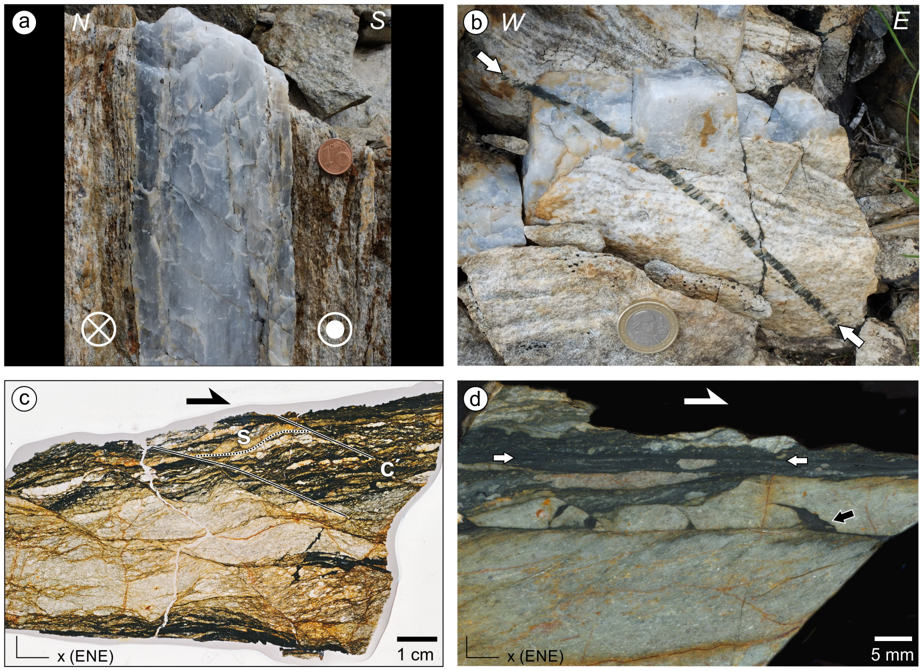

Figure 2. Field and sample pictures of the quartz mylonites and the brittle/ductile fault rocks. (a) Vertical, 7.5 cm-thick, mylonitic quartz vein within the foliated paragneisses (looking in the stretching lineation direction). Note the absence of cataclastic deformation. The white circle with the dot and with the cross indicate movement towards and from the observer, respectively, accommodated by the quartz mylonite (UTM33 326551.291 E / 5198985.993 N). (b) Fibrous quartz/chlorite vein (white arrows) cross-cutting the paragneiss and a mylonitized quartz vein oblique to the host rock foliation (UTM33 326540.807 E / 5198973.953 N) (see also Figure S6c). (c) Scan of a large thin section of foliated cataclasites and pseudotachylytes, ductilely overprinted by dextral SC' fabric (UTM33 326551.291 E / 5198985.993 N). (d) Polyphase ultracataclasites/pseudotachylytes partly overprinted by ductile deformation. Black arrow shows pseudotachylyte injection vein. Two small white arrows highlights a principal slip surface with a truncated grain, separating different generations of ultracataclasites/pseudotachylytes (UTM33 326542.099 E / 5198981.700 N).

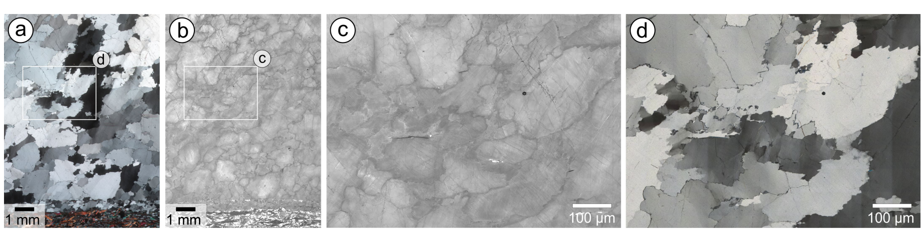

Figure 3. Weakly deformed quartz vein (sample HS-1B-2; UTM33 326621.460

E / 5199004.084 N) showing coarse grains with lobate grain boundaries typical of grain boundary migration recrystallization referable to the amphibolite facies formation conditions. (a, d) Optical microphotographs under crossed-polarized light (XPL). (b, c) SEM-CL images of same area as (a) and (d).

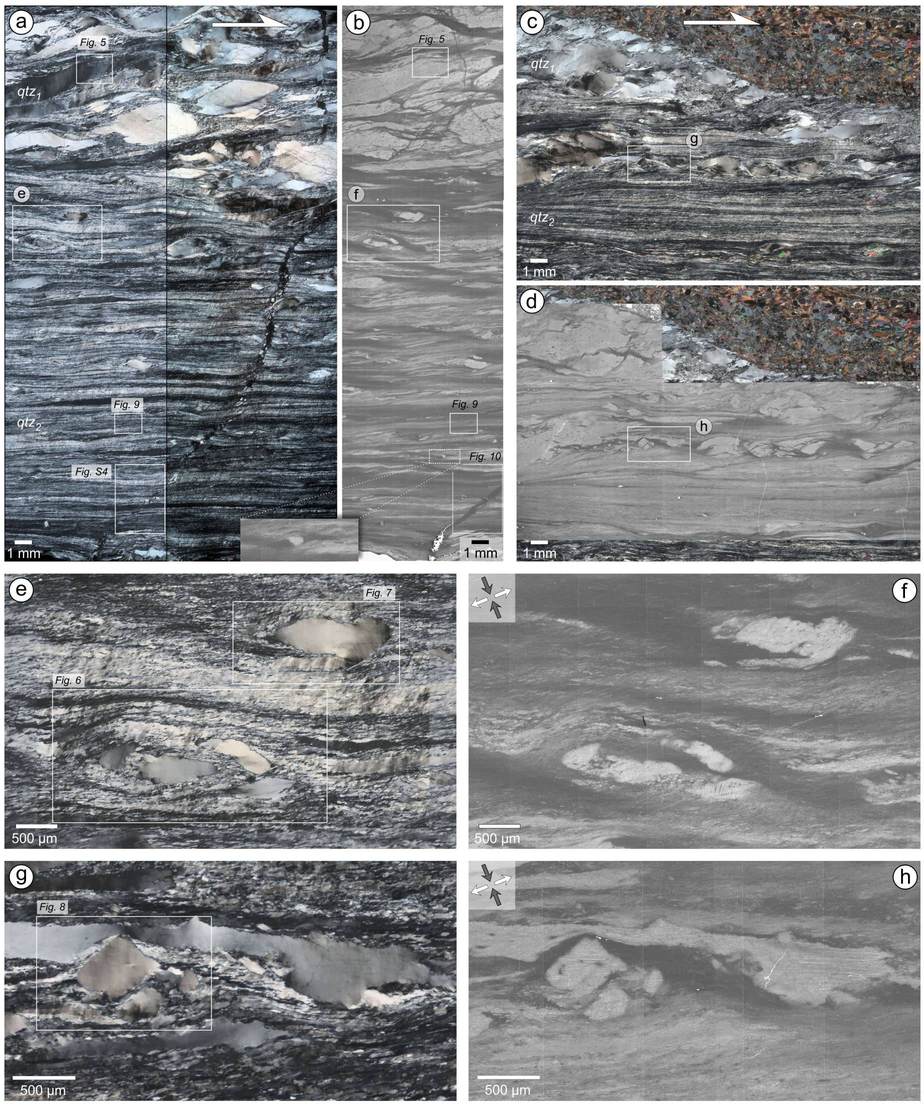

Figure 4. Microstructures (optical microphotograph, XPL, and corresponding CL images) of 2 deformed quartz veins (a, b, e, f: sample MS-H2-2; c, d, g, h: sample MS-09a - UTM 33 326551.139 E / 5198985.997). Both samples show a strain gradient from a protomylonitic fabric (upper part) to mylonitic/ultramylonitic (lower part). The latter reveals a characteristic extinction banding in the optical images (a, c). MS-H2-2 shows a corresponding banding

in the CL image (b). The (ultra)mylonitic part of MS-09a reveals similar CL intensity as the coarse qtz_1 clasts with only subtle variations (d). (e-h) Microstructures of quartz clasts in (ultra)mylonitic qtz_2 matrix. Note in (f), the CL intensity variation around the lower left clast-aggregate corresponding to stress-field – four-quadrant pattern. Similar 4-quadrand CL feature is highlighted in (b) – see insert. For both samples the schematic (not quantified) orientation of the instantaneous stretching axis is given in (f, h) – see insert. The sense of shear is dextral in all the figures.

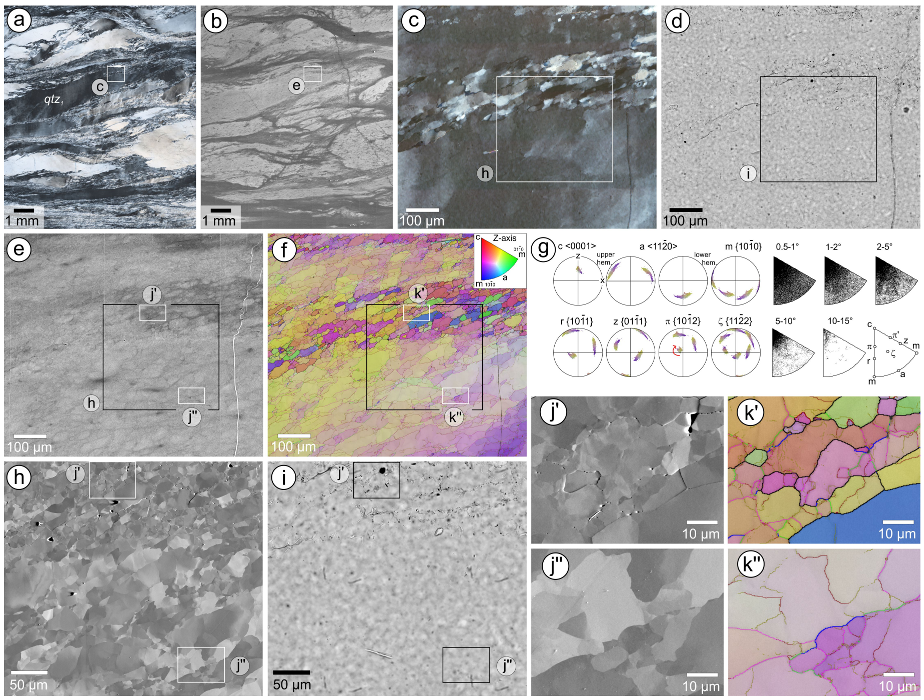

Figure 5. Internal deformation microstructure of elongated quartz grain (qtz_1). (a, b) Protomylonitic part of sample MS-H2-2 (XPL, SEM-CL). (c-f) Enlarged microstructure as marked in (a) and (b) – same location site (c: optical microphotograph, XPL; d: optical microphotograph under plane-polarized light, PPL; e: SEM-CL; f: EBSD orientation map (step size: 200 nm) colour coded with respect to Z-axis of the PF – see insert). For boundaries levels see key below. Note that high fluid inclusion (FI) spatial density in (d) matches with dark CL patterns in (e). In (e) fine dark-grey CL lines corresponds to low angle boundaries (LAB) in (f). (g) Pole figures (PF, equal area, lower hemisphere projection) and inverse PF with respect to crystal references system (equal area, upper hemisphere projection) of substructured host crystal (lower part). (h) Orientation (channelling) contrast (OC) image of area as marked in C, E, F. (I) Optical microphotograph (PPL) of same area in (h). (j, k) Detailed OC images and EBSD maps of areas as marked in e, f, h, i. Note in (j'), the porosity corresponds to FI in (I) and mainly follows high angle boundaries (HAB) of smaller

grains in (k'). In contrast (j' ') and (k' ') does not show evidence of porosity/FI. EBSD boundary levels (misorientation angle interval): low angle boundaries: olive green 0.5-1°, maroon 1-2°, fuchsia 2-5°, green 5-10°; high angle boundaries: blues 10-15°, black >15°; Dauphine twin: red 60°±5° around <*c*> axis.

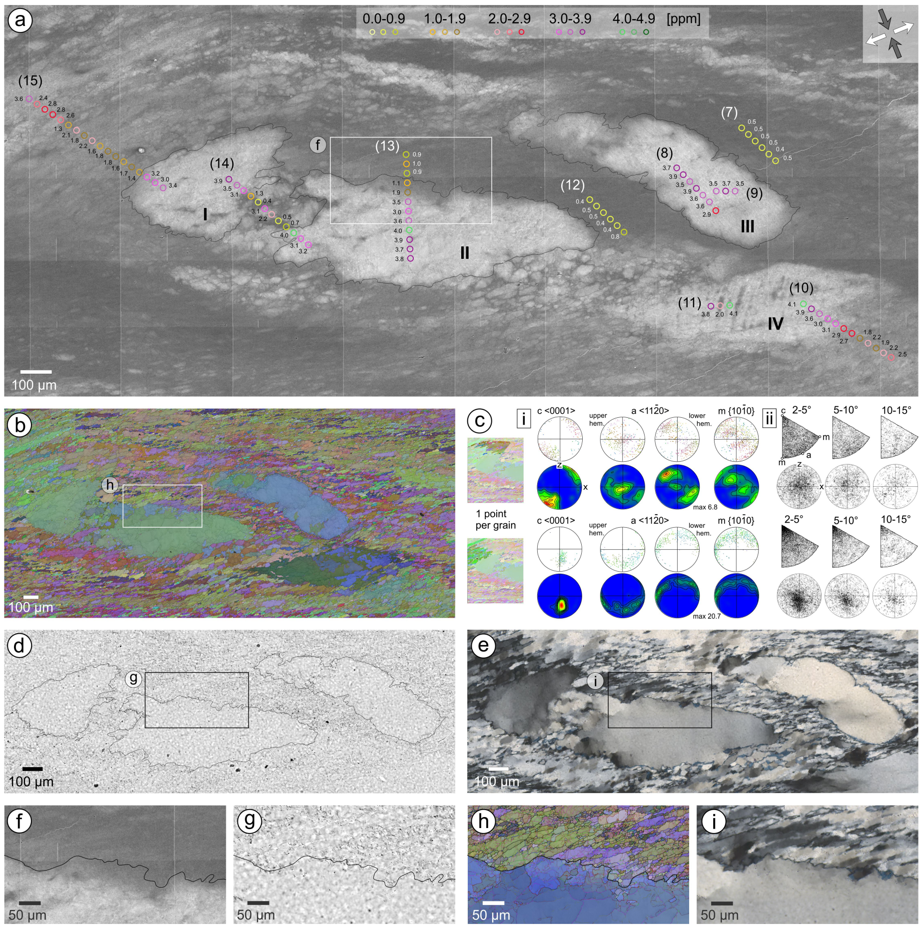

Figure 6. Cluster of *qtz₁* porphyroclasts (I-IV) within (ultra)mylonitic matrix as marked in Figure 4a, b, e, f. (a) SEM-CL image with Ti-in-qtz data. SIMS analysis spots (c. 15 µm) are colour-coded with respect to Ti concentration [Ti] – key is given. (b) EBSD map (step size: 500 nm) colour coded with respect to Euler angles. Internal substructure is highlighted by superposition of the partially transparent Euler map on the band contrast map. HAB are shown - for key see below. (c) Variation of the CPO of (ultra)mylonitic flow fabric around clast. Orientation data of 2 specific areas are plotted as (i) pole figures and (ii) misorientation axis plots of LAB (IPF, crystallographic reference system; PF, sample reference system). (d, e) Optical microphotographs (PL, XPL) of same areas as presented in (b). Note, spatial FI density correlates with CL variation

in (a). (f-i) Porphyroclast II: magnification of the porphyroclast margin outlined in a-e. Black lines indicate grain boundary (GB) of quartz clast. In (f) decreasing CL intensity in clast towards GB corresponds to higher substructure density shown in (h), whereas the FI density is relatively low (g). (h) Clast in EBSD orientation map is colour coded with respect of texture component in blue, surrounding recrystallization matrix to Euler angles. Boundary level coding follows Figure 5. Density maxima of PF are given as multiple of random distribution (*mrd*).

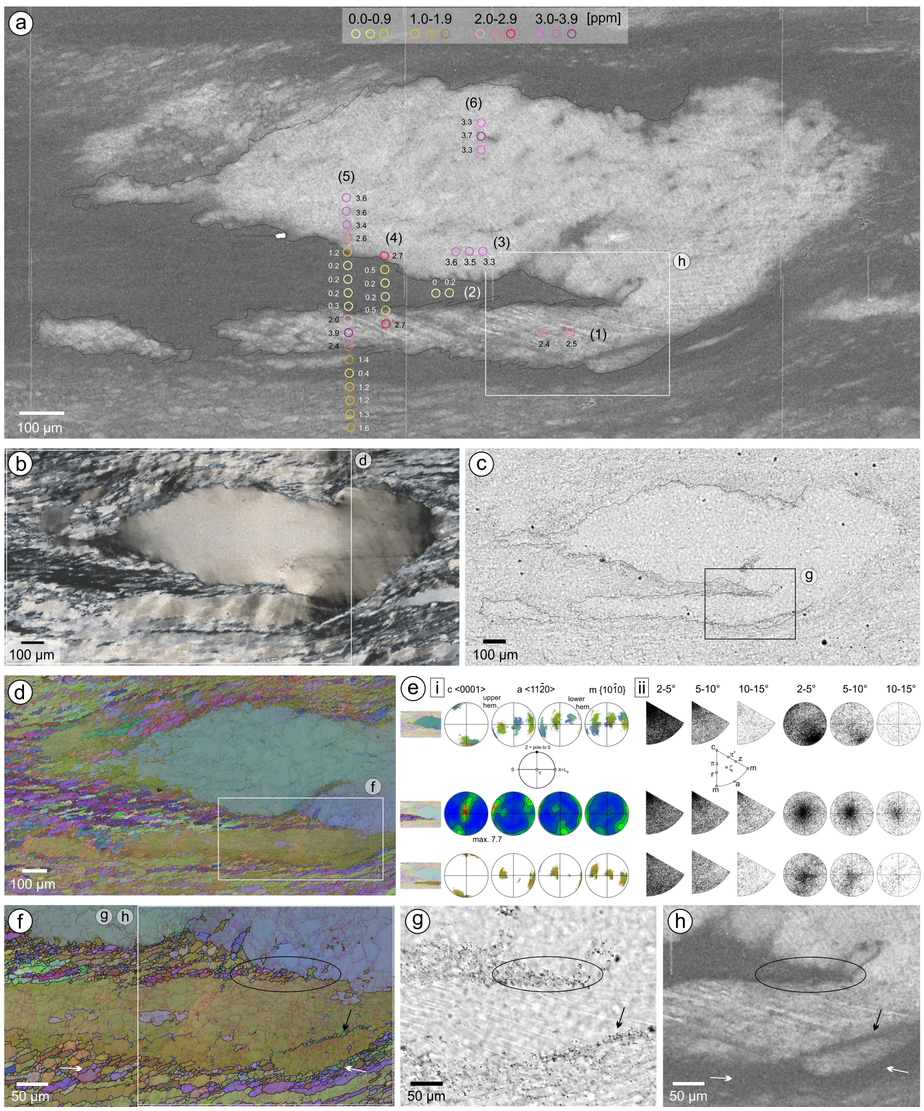

Figure 7. Quartz clast within (ultra)mylonitic matrix as marked in Figure 4a, b, e, f. (a) SEM-CL image with Ti-in-qtz data. SIMS analysis spots (c. 15 µm)

are colour with respect to [Ti] – key is given. (b, c) Optical microphotographs (XPL, PL). Note, FI density in (c) corresponds with CL variation in (a). Black line in (a-c) indicates GB of quartz clast. (d) EBSD map (step size: 500 nm): transparent superposition of Euler and band contrast map; HAB are shown - see Figure 6. (e) Orientation data of clast domains are presented as (i) PF and (ii) misorientation axis plots of LAB (IPF and PF). (f) Enlarged EBSD area as marked in (d). LAB and HAB are given – for key see Figure 5. (g) Optical microphotograph (PPL) of area as marked in (f). (h) SEM-CL image of same area as presented in (g). CL variation corresponds to FI density shown in (g). In (f-h) black arrows mark intracrystalline deformation zone traced by HAB, white arrows recrystallization zone below the clast and ellipse the tip of recrystallized aggregates between upper and lower clast domain. Oblique features in (g, h) are deformation lamellae.

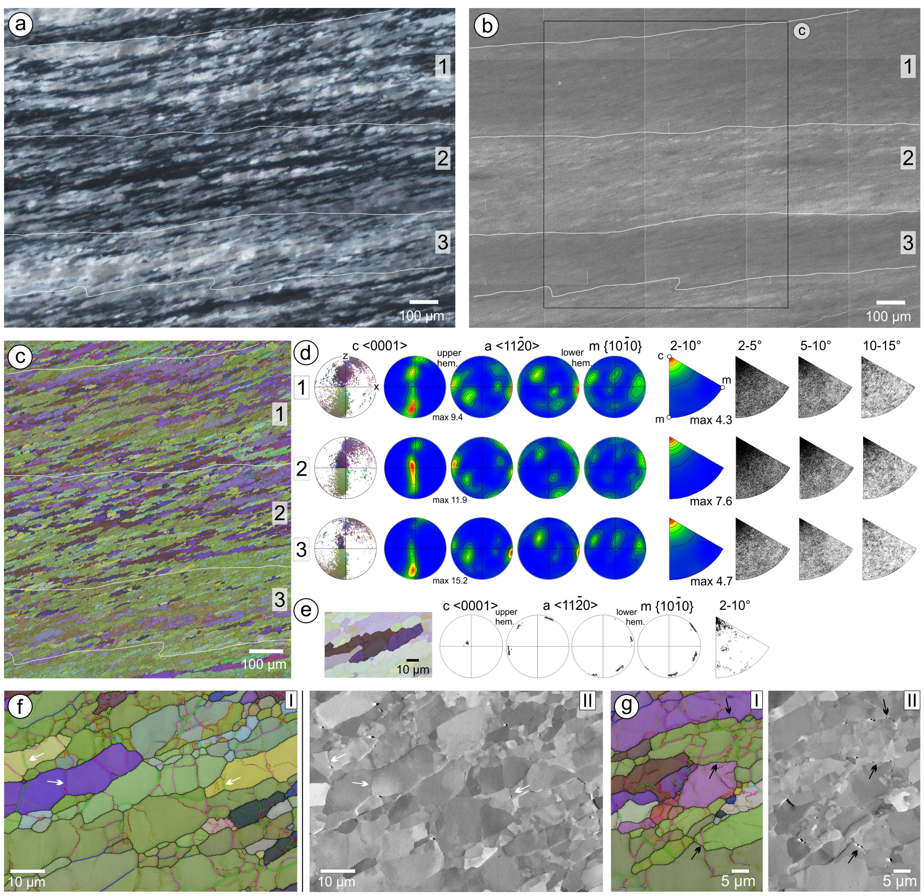

Figure 8. (Ultra)mylonite microstructure (sample HS-H2-2). (a) Optical microstructure (XPL). (b) SEM-CL image of same area as (a). (c) EBSD map (step size 200 nm) of area as marked in (b) colour-coded with respect to Euler angles. White lines in (a-c) marks CL banding. Note in (a, c), elongated grains

(aspect ratio up 10:1) are highly substructured and show an oblique shape preferred orientation (SPO). (d) Orientation data of different CL-bands (1-3) are presented as PF (CPO) and misorientation axis of LAB (2-15°) as IPF. Note, the main cluster around $<c>$ indicating prism$<a>$ slip. Density maxima (*mrd*) are given. (e) Elongated substructured grain shows a dispersion path around $<c>$ and a clustering of LAB misorientation axis in IPF also around $<c>$. (f, g) Exemplary microstructure of elongated and highly substructured quartz grains. EBSD maps (I figures) and corresponding OC images (II figures). Subgrain size is in the same order as the new small grains, 1-10 µm. White arrows in (f) indicate LAB; black arrows indicate HAB in (g), decorated with porosity (fluid inclusions). Boundary levels in EBSD maps follows key of Figure 5.

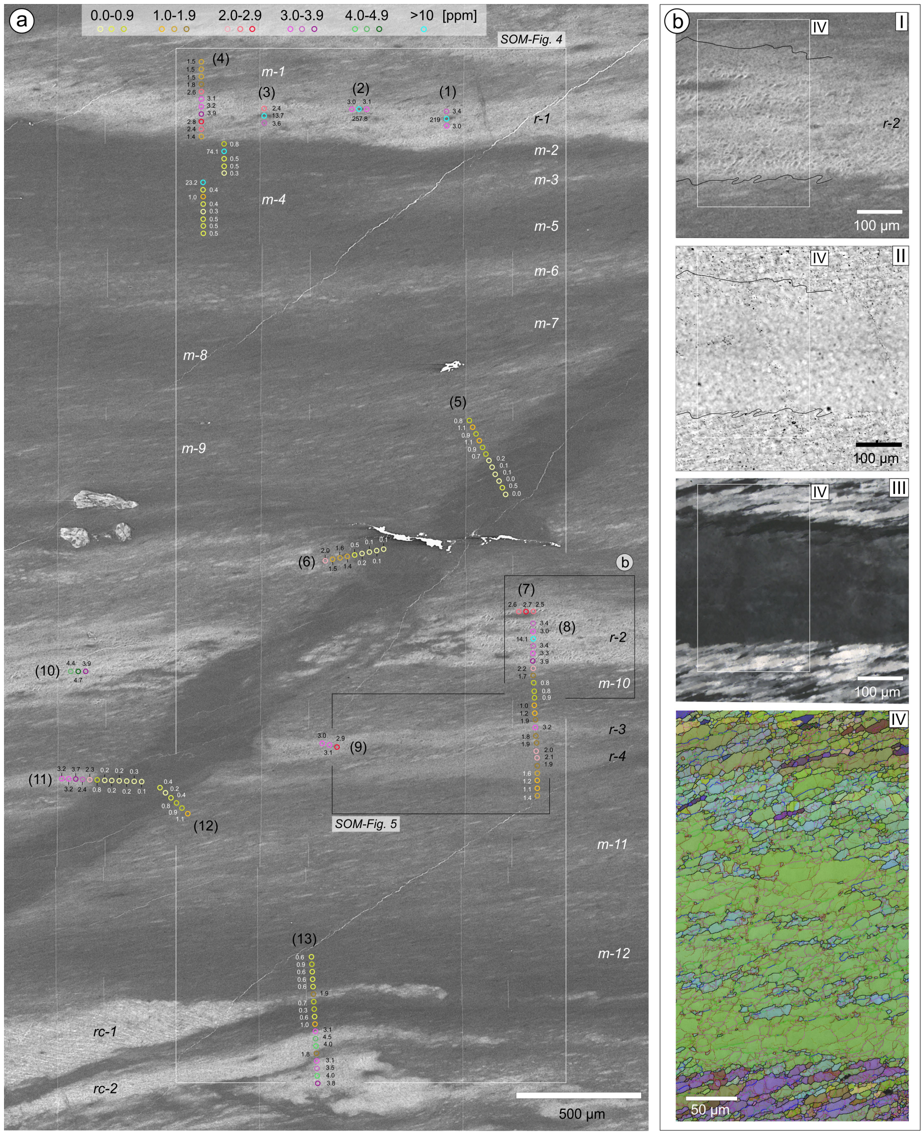

Figure 9. (a) SEM-CL image of (ultra)mylonite microstructure including (ultra)mylonitic layers (*m*), ribbon grains (*r*), ribbon-clasts (*rc*) and crosscutting late stage quartz vein. SIMS analysis spots are colour-coded with respect to [Ti] – key is given. Spots with [Ti] >10 ppm are related to micron-scale mica inclusions. (b) (I-III) Enlargement of an area of *ribbon-2* (r-2) as marked in (a). Black lines in (I, II) represent upper and lower grain boundaries of *ribbon-2*. (I) SEM-CL image. (II, III) Optical microphotograph (PPL, XPL). In (II) *ribbon-2* shows low spatial density of FI compared to high FI density in adjacent (ultra)mylonitic layers corresponding to CL intensity variation in (a). (IV)

EBSD map (step size: 500 nm) of area as marked in (I-III) colour coded with respect to Euler angles. Boundary levels follow those of Figure 5. Note high spatial density of subgrain boundary in quartz ribbon.

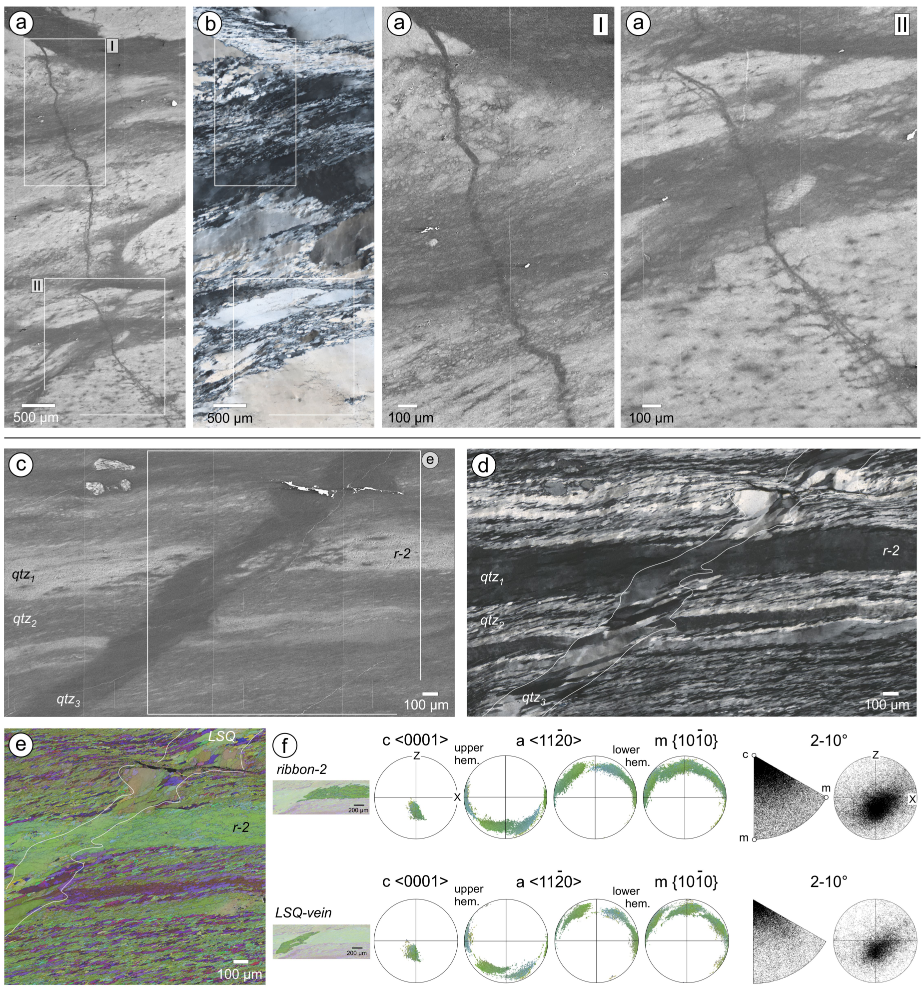

Figure 10. Late stage quartz (LSQ) vein (qtz_3) crosscutting the protomylonitic (a, b) and (ultra)mylonitic (c, d) microstructure. Optical microphotographs (XPL; b, d) and corresponding SEM-CL images (a, c). LSQ veins crosscutting the (ultra)mylonite is synkinematically deformed. (e) EBSD map (step size: 500 nm) of area as marked in (c). White line in (d) and (e) marks boundary of LSD-vein. (f) Orientation data of *ribbon-2* and LSQ vein are plotted as PF and misorientation axis of LAB as IPF and PF.

Table 1. Results of chlorite thermometry showing the number of analyses, the calculated temperature range, average and standard deviation for each microstructural site of Figure S6.

Microstructural site	n	T min [°C]	T max [°C]	avg T [°C]	std T [°C]
A: Chl in strain shadow or sheard band	13	238	268	255	11
B: Chl in garnet cracks, retrogression product of garnet	31	272	352	315	24
C: Chl in LSQ-vein	38	265	333	300	19

References

Acosta, M. D., Watkins, J. M., Reed, M. H., Donovan, J. J., & De Palolo, D. J. (2020). Ti-in-quartz: Evaluating the role of kinetics in high temperature crystal growth experiments. *Geochimica et Cosmochimica Acta,*

281, 149-167. https://doi.org/10.1016/j.gca.2020.04.030.

Ashley, K. T., Carlson, W. D., Law, R. D., & Tracy, R. J. (2014). Ti resetting in quartz during dynamic recrystallization: mechanisms and significance. *American Mineralogist* , 99, 2025–2030. http://dx.doi.org/10.2138/am-2014-4943.

Ashley, K. T., Webb, L. E., Spear, F. S., & Thomas, J. B. (2013). P-T-D histories from quartz: A case study for the application of the TitaniQ thermobarometer to progressive fabric development in metapelites. *Geochemistry, Geophysics, Geosys* (G3) 14, 3821–3843. https://doi.org/10.1002/ggge.20237.

Behr, W. M., & Platt, J. P. (2011). A naturally constrained stress profile through the middle crust in an extensional terrane. *Earth and Planetary Science Letters,* 303, 181–192. http://dx.doi.org/10.1016/j.epsl.2010.11.044.

Bestmann, M., & Pennacchioni, G. (2015). Ti distribution in quartz across a heterogeneous shear zone within a granodiorite: the effect of deformation mechanism and strain on Ti resetting. *Lithos,* 227, 37–56. https://doi.org/10.1016/j.lithos.2015.03.009.

Bestmann, M., Piazolo, S., Spiers, C. J., & Prior, D.J. (2005). Microstructural evolution during initial stages of static recovery and recrystallization: new insights from in-situ heating experiments combined with electron backscatter diffraction analysis. *Journal of Structural Geology,* 27, 447–457. http://dx.doi.org/10.1016/j.jsg.2004.10.006.

Bourdelle, F. (2021). Low-Temperature Chlorite Geothermometry and Related Recent Analytical Advances: A Review. Minerals, 11(2), 130.

Bromiley, G. D., & Hiscock, M. (2016). Grain boundary diffusion of titanium in polycrystalline quartz and its implications for titanium in quartz (TitaniQ) geothermobarometry. *Geochimica et Cosmochimica Acta,*

178, 281–290. https://doi.org/10.1016/j.gca.2016.01.024.

Calzolari, G., Rossetti, F., Ault, A. K., Lucci, F., Olivetti, V., & Nozaem, R. (2018). Hematite (U-Th)/He thermochronometry constrains intraplate strike-slip faulting on the Kuh-e-Faghan Fault, central Iran. Tectonophysics, 728, 41-54.

Campbell, L. R., Menegon, L., Fagereng, A., & Pennacchioni, G. (2020). Earthquake nucleation in the lower crust by local stress amplification. *Nature Communication,* 11. https://doi.org/10.1038/s41467-020-15150-x.

Cantarero, I., Lanari, P., Vidal, O., Alías, G., Travé, A., & Baqués, V. (2014). Long-term fluid circulation in extensional faults in the central Catalan Coastal Ranges: P–T constraints from neoformed chlorite and K-white mica. Internation Journal of Earth Sciences (Geologische Rundschau), 103(1), 165-188.

Ceccato, A., Goncalves, P., & Pennacchioni, G. (2020). Temperature, fluid content and rheology of localized ductile shear zones in sub–solidus cooling plutons. *Journal of metamorphic Geology*, 38, 881-903. https://doi.org/10.1111/jmg.12553.

Ceccato, A., & Pennacchioni, G. (2018). Structural evolution of the Rieserferner pluton in the framework of the Oligo-Miocene tectonics of the eastern Alps. *Journal of Structural Geology*, 116, 64-80. https://doi.org/10.1016/j.jsg.2018.08.004.

Ceccato, A., Pennacchioni, G., Menegon, L., & Bestmann, M. (2017). Crystallographic control and texture inheritance during mylonitization of coarse grained quartz veins. *Lithos,* 290–291, 210–227. https://doi.org/10.1016/j.lithos.2017.08.005.

Chakraborty, S., 2008. Diffusion in solid silicates. *Annual Review of Earth and Planetary Sciences,* 36, 153-190.

Cherniak, D. J., Watson, E. B. & Wark, D. A. (2007). Ti diffusion in quartz. *Chemical Geology*

236(1–2), 65-74. https://doi.org/10.1016/j.chemgeo.2006.09.001.

Drury, M. R., Humphreys, F. J., & White, S. H. (1985). Large strain deformation studies using polycrystalline magnesium as a rock analogue. Part II: dynamic recrystallization mechanisms at high temperatures. *Physics of the Earth and Planetary Interiors,* 40, 208–222. https://doi.org/10.1016/0031-9201(85)90131-1.

Farver, J. R., & Yund, R.A. (1991). Oxygen diffusion in quartz: Dependence on temperature and water fugacity. *Chemical Geology*, 90 (1-2), 55–70.

Fitz Gerald, J. D., Mancktelow, N. S., Pennaccioni, G., & Kunze, K. (2006). Ultrafine-grained quartz mylonites from high-grade shear zones: Evidence for strong dry middle to lower crust. *Geology,* 34, 369-372.

Ganne, J., De Andrade, V., Weinberg, R. F., Vidal, O., Dubacq, B., Kagambega, N., & Allibon, J. (2012). Modern-style plate subduction preserved in the Palaeoproterozoic West African craton. Nature Geoscience, 5(1), 60-65.

Grujic, D., Stipp, M., & Wooden, J. (2011). Thermometry of quartz mylonites: importance of dynamic recrystallization on Ti-in-quartz re-equilibration. *Geochemistry, Geophysics, Geosystem,* 12, Q06012. http://dx.doi.org/10.1029/2010GC003368.

Haertel, M., Herwegh, M., & Pettke, T. (2013). Titanium-in-quartz thermometry on synkinematic quartz veins in a retrograde crustal-scale normal fault zone. *Tectonophysics,* 608, 468–481. http://dx.doi.org/10.1016/j.tecto.2013.08.042.

Hamers, M. F., Pennock, F. M., & Drury, M. R. (2017). Scanning electron microscope cathodoluminescence imaging of subgrain boundaries, twins and planar deformation features in quartz. *Physics and Chemistry of Minerals,* 44, 263-275.

Hawemann, F., Mancktelow, N. S., Pennacchioni, G., Wex, S., & Camacho, A. (2019). Weak and slow, strong and fast: How shear zones evolve in a dry continental crust (Musgrave Ranges, Central Australia). *Journal of Geophysical Research: Solid Earth*, 124, 1671-1687, https://doi.org/10.1029/2018JB016559.

Hauke, M., Froitzheim, N., Nagel, T.J., Miladinova, I., Fassmer, K., Fonseca, R. O. C., Sprung, P., & Münker, C. (2019). Two high-pressure metamorphic events, Variscan and Alpine, dated by Lu–Hf in an eclogite complex of the Austroalpine nappes (Schobergruppe, Austria). *International Journal of Earth Sciences (Geologische Rundschau),* 108, 1317-1331. https://doi.org/10.1007/s00531-019-01708-8.

Hirth, G., & Beeler, N. M. (2015). The role of fluid pressure on frictional behavior at the base of the

seismogenic zone. *Geology,* 43, 223-226. doi:10.1130/G36361.1

Howard, D. L., de Jonge, M. D., Afshar, N., Ryan, C. G., Kirkham, R., Reinhardt, J., Kewish, C. M., McKinlay, J., Walsh, A., Divitcos, J., Basten, N., Adamson, L., Fiala, T., Sammut, L., & Paterson, D.J. (2020). The XFM beamline at the Australian Synchrotron. *Journal of Synchrotron Radiation,* 27, 1447-1458. https://doi.org/10.1107/S1600577520010152

Huang, R., & Audétat, A. (2012). The titanium-in-quartz (TitaniQ) thermobarometer: a critical examination and re-calibration. *Geochimica et Cosmochimica Acta,* 84, 75–89.

Kidder, S., Avouac, J.-P., & Chand, Y.-C. (2013). Application of titanium-in-quartz thermobarometry to greenschistfacies veins and recrystallized quartzites in the Hsüehshan range, Taiwan. *Journal of Geophysical Research: Solid Earth,* 4, 1–21.

Kidder, S., Toy, V., Prior, D., Little, T., & Macrae, C. (2018). Constraints on alpine fault (New Zealand) mylonitization temperatures and geothermal gradient from Ti-in-quartz thermobarometry. *Journal of Geophysical Research: Solid Earth,* 9, 1123-1139.

Kirschner, D., & Teyssier, C. (1991). Quartz c-axis fabric differences between porphyroclasts and recrystallized grains. *Journal of Structural Geology*, 13, 105-109. https://doi.org/10.1016/0191-8141(91)90106-S

Kohn, M. J., & Northrup, C. J. (2009). Taking mylonites' temperatures. *Geology,* 37, 47–50.

Korchinski, M., Little, T. A., Smith, E., & Millet, M.-A. (2012). Variation of Ti-in-quartz in gneiss domes exposing the world's youngest ultrahigh-pressure rocks, D'Entrecasteaux Islands, Papua New Guinea. *Geochemistry, Geophysics, Geosystem,* 13, Q0AL01. http://dx.doi.org/10.1029/2012GC004230.

Krenn, E., Schulz, B., & Finger, F. (2012). Three generations of monazite in Austroalpine basement rocks to the south of the Tauern Window: evidence for Variscan, Permian and Eo-Alpine metamorphic events. *Swiss Journal of Geoscience,* 105(3), 343-360.

Lacroix, B., Charpentier, D., Buatier, M., Vennemann, T., Labaume, P., Adatte, T., & Dubois, M. (2012). Formation of chlorite during thrust fault reactivation. Record of fluid origin and P–T conditions in the Monte Perdido thrust fault (southern Pyrenees). Contributions to Mineralogy and Petrology, 163(6), 1083-1102.

Legros, M., Dehm, G., Arzt, E., & Balk, T. J. (2008). Observation of giant diffusivity along dislocation cores. *Science,* 319, 1646–1649. http://dx.doi.org /10.1126/science.1151771.

Linner, M. (1999). Die P-T-t Entwicklung der Eklogite im Schoberkristallin als Beleg für frühalpidische kontinentale Subduktion im Ostalpinen Kristallin. *Thesis, University of Vienna*, 211 p.

Linner, M., Habler, G., & Grasemann, B. (2009). Switch of kinematics in the austroalpine basement between the defereggen-antholz-Vals (DAV) and the Pustertal-Gailtal fault. In: *9th Workshop on Alpine Geological Studies Cogne/Italy*, 16, pp. 18.

Mancktelow, N. S., Stöckli, D. F., Grollimund, B., Müller, W., Fügenschuh, B., Viola, G., Seward, D., & Villa, I. M. (2001). The DAV and Periadriatic fault systems in the Eastern Alps south of the Tauern window. *International Journal of Earth Sciences (Geologische Rundschau),* 90 (3), 593-622.

Mizera, M., Little, T., Boulton, C., Prior, D., Watson, E., Biemiller, J., & Shigematsu, N. (2020). Slow-to-fast deformation in mafic fault rocks on an active low-angle normal fault, Woodlark Rift, SE Papua New Guinea. Geochemistry, Geophysics, Geosystem, 21(11), e2020GC009171.

Nachlas, W. O., & Hirth, G. (2015). Experimental constraints on the role of dynamic recrystallization on resetting the Ti-in-quartz thermobarometer. *Journal of Geophysical Research: Solid Earth,* 120, 8120–8137. https://doi.org/10.1002/2015JB012274.

Nachlas, W. O., Whitney, D. L., Teyssier, C., Bagley, B., & Mulch, A. (2014). Titanium concentration in quartz as a record of multiple deformation mechanisms in an extensional shear zone. *Geochemistry, Geophysics, Geosystem,* 15, 1374–1397. http://dx.doi.org/10.1002/2013GC005200.

Nachlas, W. O., Thomas, J. B., & Hirth, G. (2018). TitaniQ deformed: Experimental deformation of out-of-equilibrium quartz porphyroclasts. *Journal of*

Structural Geology, 116, 207-222.

Negrini, M., Stünitz, H., Berger, A., & Morales, L. F. G. (2014). The effect of deformation on the TitaniQ geothermobarometer: an experimental study. *Contributions to Mineralogy and Petrology,* 167, 982. http://dx.doi.org/10.1007/s00410-014-0982-x.

Neumann, B. (2000). Texture development of recrystallized quartz polycrystals unravelled by orientation and misorientation characteristics. *Journal of Structural Geology,* 22, 1695–1711.

Pennacchioni, G., & Mancktelow, N. S. (2018). Small-scale ductile shear zones: Neither extending, nor thickening, nor narrowing. *Earth-Science Reviews*, 184, 1-12. https://doi.org/10.1016/j.earscirev.2018.06.004.

Pennacchioni, G., Menegon, L., Leiss, B., Nestola, F., & Bromiley, G. (2010). Development of crystallographic preferred orientation and microstructure during plastic deformation of natural coarse-grained quartz veins. *Journal of Geophysical Research: Solid Earth,* 115, B12405. http://dx.doi.org/10.1029/2010JB007674.

Pennacchioni, G., & Zucchi, E. (2013). High-temperature fracturing and ductile deformation during cooling of a pluton: the Lake Edison granodiorite (Sierra Nevada batholith, California). *Journal of Structural Geology*, 50, 54-81. https://doi.org/10.1016/j.jsg.2012.06.001.

Piazolo, S., La Fontaine, A., Trimby, P., Harley, S., Yang, L., Armstrong, R. & Cairney J. M. (2016). Deformation-induced trace element redistribution in zircon revealed using atom probe tomography. *Nature Communication,*

7, 10490. https://doi.org/10.1038/ncomms10490.

Plunder, A., Agard, P., Dubacq, B., Chopin, C., & Bellanger, M. (2012). How continuous and precise is the record of P–T paths? Insights from combined thermobarometry and thermodynamic modelling into subduction dynamics (Schistes Lustrés, W. Alps). Journal of Metamorphic Geology, 30(3), 323-346.

Powell, R., & Holland, T. J. B. (2008). On thermobarometry. Journal of Metamorphic Geology, 26(2), 155-179.

Ratschbacher, L., Frisch, W., Neubauer, F., Schmid, S. M., & Neugebauer, J. (1989). Extension in compressional orogenic belts: the Eastern Alps. *Geology,* 17, 404–407. https://doi.org/10.1130/0091-7613(1989)017%3C0404:EICOBT%3E2.3.CO;2.

Rosenberg, C. L., Brun, J. P., Cagnard, F., & Gapais, D. (2007). Oblique indentation in the Eastern Alps: insights from laboratory experiments. *Tectonics*, 26(2). https://doi.org/10. 1029/2006TC001960.

Schulz, B. (1993). Mineral chemistry, geothermobarometry and pre-Alpine high-pressure metamorphism of eclogitic amphibolites and mica schists from the

Schobergruppe, Austroalpine basement, Eastern Alps. *Mineralogical Magazine,* 57(387), 189-202.

Schuster, R., Daurer, A., Krenmayr, H.-G., Linner, M., Mandl, G. W., Pestal, G., & Reitner, J. M. (2014). Rocky Austria: The Geology of Austria - brief and colourful. *Vienna, Geological Survey Austria*, p. 1-80.

Spear, F. S., & Wark, D. (2009). Cathodoluminescence imaging and titanium thermometry in metamorphic quartz. *Journal of Metamorphic* Geology, 27, 187–205.

Stipp, M., Stünitz, H., Heilbronner, R., & Schmid, S. M. (2002). The Eastern Tonale fault zone: a "natural laboratory" for crystal plastic deformation of quartz over a temperature range from 250 to 700 °C. *Journal of Structural Geology,* 24, 1861–1884.

Thomas, J. B., & Watson, E. B. (2014). Diffusion and partitioning of magnesium in quartz grain boundaries. *Contributions to Mineralogy and Petrology,* 168, 1–12. https://doi.org/10.1007/s00410-014-1068-5.

Thomas, J. B., Watson, E. B., Spear, F. S., Shemella, P. T., Nayak, S. K., & Lanzirozzi, A. (2010). TitaniQ under pressure: the effect of pressure and temperature on the solubility of Ti in quartz. *Contributions to Mineralogy and Petrology,* 160, 743–759.

Thöni, M. (2006). Dating eclogite-facies metamorphism in the Eastern Alps – approaches, results, interpretations: a review. *Mineralogy and Petrology,* 88(1-2). https://doi.org/10.1007/s00710-00006-00153-00715.

Urai, J. L., Means, W. D., & Lister, G. S. (1986). In: Hobbs, B. E., Heard, H. C. (Eds.), Dynamic Recrystallization of Minerals. Mineral and Rock Deformation: the Paterson Volume. *American Geophysical Union*, Washington, D.C., pp. 1–49.

Vidal, O., Parra, T., & Vieillard, P. (2005). Thermodynamic properties of the Tschermak solid solution in Fe-chlorite: Application to natural examples and possible role of oxidation. American Mineralogist, 90(2-3), 347-358.

Vidal, O., de Andrade, V., Lewin, E., Munoz, M., Parra, T., & Pascarelli, S. (2006). P–T-deformation-Fe^{3+}/Fe^{2+} mapping at the thin section scale and comparison with XANES mapping: application to a garnet-bearing metapelite from the Sambagawa metamorphic belt (Japan). Journal of Metamorphic Geology, 24(7), 669-683.

Wark, D. A., & Spear, F. S. (2005). Titanium in quartz: Cathodoluminescence and thermometry. *Geochimica et Cosmochimica Acta*, Suppl. 69, A592.

Wark, D. A., & Watson, E. B. (2006). TitaniQ: a titanium-in-quartz geothermometer. *Contributions to Mineralogy and Petrology,* 152, 743–754.

Yund, R. A., Smith, B. M., & Tullis, J. (1981). Dislocation-assisted diffusion of oxygen in albite. *Physics and Chemistry of Minerals,* 7, 185–189.

Yund, R. A., & Tullis, J. (1991). Compositional changes of minerals associated with dynamic recrystallization. *Contributions to Mineralogy and Petrology,* 108, 346–355. https://doi.org/10.1007/BF00285942.

Zihlmann, B., Müller, S., Coggon, R. M., Koepke, J., Garbe-Schönberg, D., & Teagle, D. A. (2018). Hydrothermal fault zones in the lower oceanic crust: An example from Wadi Gideah, Samail ophiolite, Oman. Lithos, 323, 103-124.